UNIVERSITY OF OKLAHOMA
GRADUATE COLLEGE

GENERATION OF SYNTHETIC ANTENNA APERTURES IN SWARM UNMANNED AERIAL SYSTEMS USING TIGHT-COUPLING

A THESIS
SUBMITTED TO THE GRADUATE FACULTY
in partial fulfillment of the requirements for the
Degree of
MASTER OF SCIENCE

By

BENJAMIN KORTY
Norman, Oklahoma
2022

GENERATION OF SYNTHETIC ANTENNA APERTURES IN SWARM UNMANNED AERIAL SYSTEMS USING TIGHT-COUPLING

A THESIS APPROVED FOR THE
SCHOOL OF ELECTRICAL AND COMPUTER ENGINEERING

BY THE COMMITTEE CONSISTING OF

Dr. Jessica Ruyle, Chair

Dr. Caleb Fulton

Dr. Nathan Goodman

Table of Contents

List of Tables

List of Figures

Abstract

Relative to their various land and air-based counterparts, swarm unmanned aerial system (SUAS) platforms, being comprised of many separate airborne bodies, or elements, possess a number of unique and advantageous characteristics, whether in the context of radar, or communications. These advantages include reduced element complexity, minimal size, weight, and power (SWaP) requirements, and a high degree of redundancy, among others. Because individual bodies in an SUAS are generally smaller than single UAS systems, however, it is generally imperative that the overall electromagnetic performance of the entire swarm match or even exceed that of its single-bodied counterpart, compensating for any reduction in the capabilities of individual radiators within the SUAS. Consequently, even with reduced complexity in the individual elements, the design and control of such large arrays of radiating bodies often presents a very significant challenge. Previous work has demonstrated the efficacy of design techniques involving widely-spaced, sparse arrays, and deliberate use of aperiodicity in order to maximize array radiation performance, while minimizing any deleterious effects. Such design techniques, however, are quite limited in their use, often requiring very large numbers of electromagnetically large elements, whilst only achieving fairly narrowband solutions. Consequently, attempts to make use of these techniques require both a high degree of control complexity, and vast amounts of space, being unable to bring elements close together, lest detrimental phenomena like mutual impedance arise. To enable the design of more tightly-spaced SUAS with fewer, and potentially smaller,

elements, a fairly new antenna array design technique will be utilized, being now applied to the more challenging domain of SUAS for the first time. In particular, the following will be the application of tight-coupling, which exploits rather than mitigates the presence of mutual impedance, to closely-spaced antenna arrays. Thus, the ability of tight-coupling techniques, when applied to SUAS, to generate useful antenna array apertures will subsequently investigated. This exploration will pay particular attention to arrays comprised of elements with poor individual radiative capabilities. The performance of these SUAS arrays will be assessed primarily in terms of spectral impedance, efficiency, and realized gain behavior.

Chapter 1

Motivation of SUAS

1.1 The Utility of Airborne Radar Systems

Radar systems, categorically speaking, have been one of the most useful innovations of the past hundred years, being ubiquitous throughout science and technology, as well as everyday life. Myriad examples of this exist whether taken from geological exploration, meteorology, astronomy, or even from more commonplace cases such as air traffic control, law enforcement, or various military applications. Of the plethora of distinct incarnations of radar that have come into existence, however, airborne radar systems have, with respect to their ground and sea-based counterparts, gained particular prominence. This fact is likely due to the variety of advantages possessed by such airborne systems.

Principal among these advantages is an airborne radar system's range. Whether used for target identification, environmental mapping, or any application in between, a radar system's range is of primary concern. As noted in [1] for example, for a moving target identification (MTI) system, the difference in detection range between a 100-ft antenna mast, and that flying at 25,000-ft can be as great as 183 nautical miles (nmi). Simply put, this figure means that, even when barring physical obstructions and issues with refraction for the ground-based radar, the airborne system will outperform its

counterpart by more than 1500%, as the latter is limited to about 12 nmi [1]. The reason for this is of course clear, as the increased elevation of the airborne system drastically increases the number of potential targets within the system's line of sight, among other reasons.

Additional advantages of airborne radars include reduced ground clutter and of course the mobility of the platform itself, being able to not only cover greater ranges than stationary systems, but also change locations much more rapidly. Land-based radars, by contrast, beyond being unable to relocate rapidly, must also generally avoid low beam angles with respect to the ground, as pointed out in [1], in order to avoid significant ground clutter in the back-scattered signal. This is especially true in heavily populated environments, whether in the form of urban areas with densely crowded buildings, heavily wooded regions with dense foliage, etc. Airborne platforms, by virtue of elevation, obviate this challenge.

Finally, a number of further, radar-based applications such as synthetic aperture radar (SAR) [2]-[3], foliage penetrating radars [4], and "the characterization of precipitation micro-physics and other meteorological phenomena" [5] exist exclusively because of, or have been revolutionized by, the advent of airborne radar systems.

1.2 Swarm-based Unmanned Aerial Systems (SUAS)

Now, while airborne radar systems do possess numerous performance advantages on a systems level as was stated above, such systems at the same time do present a significant challenge in terms of design, especially with respect to a given radar's antenna. As is discussed in [6], the electromagnetic environment in which an airborne antenna is placed is often far more complex than that of its ground-based counterpart, let alone the standard, open, free-space environment upon which much of antenna theory is based;

this is due in large part to the conflicting structural and electromagnetic needs of typical aircraft, wherein some optimization is required. For example, for externally located antennas, it is often a requisite that the antenna's profile be minimized in order to limit unwanted drag on the body of the aircraft; this requirement however, often comes at the expense of electromagnetic performance, particularly in the form of poor antenna efficiency, gain, or bandwidth. Furthermore, because unmanned aerial systems are often required to be self-sufficient for the duration of their operation, limitations involving size, weight, and power (SWaP), as discussed in [7]–[11], are often of critical importance during design. In particular, as the size of an airborne radar platform scales linearly, its weight and power requirements, as well as the complexity of its power control systems, will much more climb rapidly [7].

One increasingly common way to circumvent these and other concerns regarding solitary airborne platforms is the move towards swarm unmanned aerial systems (SUAS). SUAS possess considerable advantages over the single UAS, the first of these being the aforementioned SWaP constraints. Because each individual UAV body in an SUAS is scaled to much smaller dimensions than the typical single-body UAS, the design complexity of each unit is enormously reduced, which in turn is multiply beneficial, as both the cost and requisite power needs of each unit drop significantly. In fact, the cost of an entire swarm is, in many cases, a fraction of that of its singular counterpart, as was the case with the US Navy's LOCUST program [12]. With respect to performance, while each individual element in a SUAS will of course not be able to match the capabilities of the larger UAS, a number of techniques exist to ensure that the performance of the overall SUAS matches or even exceeds that of the large UAS, as will be discussed in the next chapter.

Secondly, for a variety of both military and non-military applications, the presence of a substantial number of small UAV bodies is greatly advantageous over a single,

larger body. In the event of military engagement or even volatile weather, the greater number of aircraft in the SUAS provides a degree of redundancy that allows continued operation of the swarm even if a few aircraft are rendered non-operational. Additionally, being smaller in size, SUAS bodies provide both a smaller physical target and a smaller radar cross-section (RCS) [12], granting them a greater likelihood of survival. Clearly, the larger UAS lacks these advantages. Additionally, for reasons that will be discussed throughout this thesis, the SUAS provides a much greater degree of mechanical, and therefore operational, reconfigurability, when compared to, for example, a large phased array mounted on a single, large UAS.

1.3 Thesis Outline

In the following chapters, this thesis explores methods by which the apertures generated by SUAS may be analyzed, and subsequently, evaluates the performance of such apertures. In chapter 2, various design techniques by which antenna arrays may be constructed are introduced and briefly evaluated, and in particular, the concept of tight-coupling is investigated. This chapter continues with a brief sketch of the anticipated mutual coupling expected to exist between elements of an SUAS when these elements are assumed to be large-radius, radiating cylinders. In fact, this assumption that the SUAS's array characteristics may be well approximated by replacing the elements with fuselage-representing cylinders will be maintained throughout the duration of this thesis. Consequently, this thesis focuses specifically on the results that may be achieved under these assumptions.

The physical theory of radiating cylinders is then discussed at length in chapter 3, particular attention being given to the derivation of integro-differential equations useful in the analysis of dipole antennas. Chapter 4 then gives a survey of the method

of moments, a series technique by which the complex derivations of chapter 3 may be readily evaluated. In chapter 5, the behavioral trends of individual radiating cylinders is then evaluated, multiple baselines for later comparison being devised. The approximate, simulated mutual impedance between two cylinders is then analyzed in chapter 6, wherein the efficacy of SUAS inter-element coupling used in this thesis is explored. Subsequently, chapter 7 and 8 discuss the generation of antenna apertures in parasitic and driven cylinder arrays, respectively. Finally, chapter 9 serves as the conclusion to this thesis, summarizing the previous and future work involved in this project.

Chapter 2

Introduction to Tightly-Coupled Arrays in SUAS

2.1 Introduction

As discussed in the previous chapter, SUAS-based radars hold several advantages over their single-bodied counterparts. One of the principal advantages is the ability of SUAS to mechanically reconfigure and thus provide a greater number of operational capabilities due to the vast number of arrangements into which the SUAS may configure itself. Nonetheless, as is commonplace with antenna arrays, a wide variety of array ordering techniques exist [13], and understanding the relative advantages of each is of course critical. In the case of SUAS, the most common approach is the aperiodic sparse array.

Before discussing sparse arrays, however, it's important to note that traditionally popular phased, and more generally periodic, arrays tend to be undesirable for SUAS applications, due to their extreme sensitivity to element positioning in terms of sidelobe levels (SLL) and antenna gain [14]. Specifically, because positional and orientational errors tend to be high in an SUAS due to weather and control complexity, the sensitivity of such arrays are almost always incompatible with SUAS applications, especially for arrays operating at higher frequencies.

In addition to sparse arrays, this thesis will present tightly-coupled arrays, a relatively newer method of organizing antenna arrays that has not previously been applied

to airborne swarms, yet presents many advantages therein.

2.2 On Frequency Selection in Radar

Before discussing specific array types however, it will be beneficial to clarify the relevance of frequency and electrical size in SUAS design. Specifically, in order to meet the performance specifications of any application, identification of the optimal frequency band in which to operate, as well as the ideal electrical size of the respective SUAS elements, will be absolutely paramount. In many cases in fact, the operational frequency of an SUAS will be at least partially determined by its intended application. For example, as [15] mentions, radar imaging systems, whether used for surveillance or geographic mapping, often benefit from higher signal frequencies, as such will increase the resolution of the constructed image depending on the waveform used. Additionally, in the case of more complex beam-forming techniques, higher frequencies are useful in producing smaller beam angles for an array with a given element size [16]-[17]. In other words, given that the range of manufacturable antenna sizes is limited, higher frequencies will always permit the narrowest beams by noting that

$$\theta_{3dB}\phi_{3dB} \propto \frac{1}{Af^2} \quad , \tag{2.1}$$

where Θ_{3dB} and ϕ_{3dB} are the azimuthal and elevation beam-widths (assuming a generalized elliptical beam), and A is the antenna's aperture. This in turn improves resolution, as previously mentioned in [15], as

$$\Delta V = \frac{\pi}{4} R^2 \theta_{3dB}\phi_{3dB}\Delta R \quad . \tag{2.2}$$

Here, ΔV is the radar's unit cell volume, and R is the radar range. ΔR is then related to the radar pulse envelope in that

$$\Delta R = \frac{c\tau}{2} \quad , \tag{2.3}$$

where c is the speed of light, and τ is the pulse duration. Additionally, as noted in [18], for applications such as communications where high data rates are crucial, the choice of higher frequencies leads to greater data rates as

$$R_b = R_s log_2 M \quad . \tag{2.4}$$

Here, R_b is the bit rate of the communication channel, M is related to the modulation scheme, and R_s is the symbol rate which is directly proportional to the channel's carrier frequency.

Conversely, lower frequencies have their own unique set of benefits; one of these is attenuation. Because a transmitted signal's maximal range drops off rapidly with increasing frequency according to the radar range equation, which states that

$$R_{max} = \sqrt[4]{\frac{P_t G^2 c^2 \sigma}{(4\pi)^3 P_{min} f^2}} \quad , \tag{2.5}$$

lower operational frequencies allow an SUAS to both operate farther from its target and have greater inter-element spacing. This of course, may be useful depending on the type of antenna array being employed. Here, P_t and P_{min} are related to signal power, G is the antenna's gain, and σ is the target's RCS. The radar range equation also demonstrates how SUAS operating at longer wavelengths are often be able to reduce power requirements, as transmitted signals attenuate significantly more slowly. Additionally, depending on the application, various lower frequency bands such as HF and

VHF may present advantages in terms of lower absorption, as higher frequencies tend to be much more readily absorbed, whether by dense foliage, atmospheric water, or materials found in urban environments such as concrete [19]. This, in turn, presents bands like HF and VHF with certain superior capabilities including greater foliage penetration in geographic mapping and imaging, and enhanced atmospheric penetration in high-altitude applications.

However, one important disadvantage of lower frequencies, especially for HF and below, is antenna efficiency. Because most UAV bodies are size-limited, meaning building electrically large aircraft for long wavelengths is almost always prohibitively expense, when at all possible, one common yet severe disadvantage of SUAS operating in bands around HF is small electrical size, which always means reduced antenna efficiency and thus wasted power, usually in the form of thermal noise or impedance mismatch. Tightly-coupled arrays however, the technique applied to SUAS in this thesis, often partially circumvent this issue by synthesizing larger antenna apertures from smaller elements, thus reducing the detrimental effects of being electrically small.

2.3 Aperiodic Sparse Arrays

Unlike phased arrays, aperiodic sparse arrays do not in general suffer heavily from noise related to element positioning errors; in fact, being derived from random arrays, aperiodic arrays are usually designed specifically to avoid these issues. Where as phased arrays are cleverly designed to selectively cancel out the detrimental effects of mutual impedance normally present in antenna arrangements with close inter-element spacing, aperiodic sparse arrays, by virtue of being sparse, do the opposite. These arrays generally circumvent the issue of mutual impedance by increasing this inter-element spacing until mutual impedance is effectively mitigated, or at least until the designer feels safe

in ignoring such effects. This is shown in greater detail in [20], where floquet theory is applied to 2D planar arrays to demonstrate significantly decreased sensitivity in the field response under increased positional errors.

From here, a variety of techniques can be used to properly arrange the array such that the field patterns of each element can be summed into a single resultant field matching the desired array performance. [21], for example, investigates the performance of an array in an urban environment using four pre-determined array configurations, determining in this case, linear arrays to be beneficial for multiple input, multiple output (MIMO) applications. In [14] and [22], the effect of positional noise on array performance is characterized, and methods by which to mitigate these effects are developed. Specifically, for some N-element array, the array factor, AF, with current magnitude and phase terms I_n and β_n, is defined such that

$$AF(\theta, \phi) = \frac{1}{N} \sum_{n=1}^{N} I_n e^{j[k\hat{n}\cdot(r_n+\tilde{r}_n)+\beta_n]} \quad , \tag{2.6}$$

where k is the wave number, and r_n and $\tilde{r}_n$ are the nominal position and positional noise of the nth element. Here, setting β_n equal to the nominal phase term plus an additive correctional term by stating that

$$\beta_n = \beta_{in} + \beta_{cn} \quad , \tag{2.7}$$

serves as one method of error minimization via phase modulation. By adding this correctional phase term, the effects of positional noise in the nth term may clearly be minimized whenever

$$\beta_{cn} \approx k\hat{n} \cdot \tilde{r}_n \quad , \tag{2.8}$$

which, if the noise is assumed Gaussian, leads to a maximum system variance, σ^2_{system},

where

$$\sigma^2_{system} \leq \frac{2k^2\sigma^2(1-\cos\psi)}{N} \quad . \tag{2.9}$$

Under these assumptions, σ^2 is the variance of a single element in the array, assumed to be equal in the far field for every element, while ψ is the angle from the array's bore-sight direction to the observation direction. The above expression for the system noise variance, equation (2.9), immediately illustrates several important aspects of this strategy of error correction. Firstly, it's easily observed that the upper limit on an array's noise variance drops quickly as the size of the array scales. Larger arrays may be justified in this way, being significantly more tolerant to positional errors. Secondly, this upper limit increases quadratically with wave number, demonstrating how the aforementioned strategy functions more reliably in lower frequency bands, but weakens as frequency is scaled upwards. Finally, as is visible in the $1-\cos\psi$ term in equation (2.9), large observation angles, relative to the direction of bore-sight, can lead to significant variance in the system's array factor.

[14] also discusses how, by means of genetic algorithms, array element arrangements may be found such that the system's side-lobe level (SLL) is minimized as shown in fig. 2.1 and fig. 2.2.

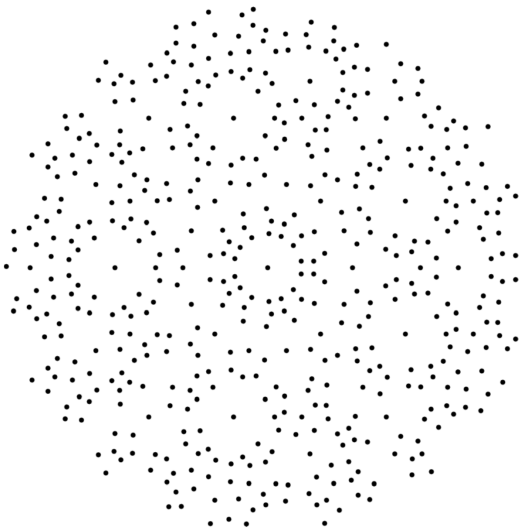

Figure 2.1: Optimized 505-element array configuration designed by genetic algorithm in [14].

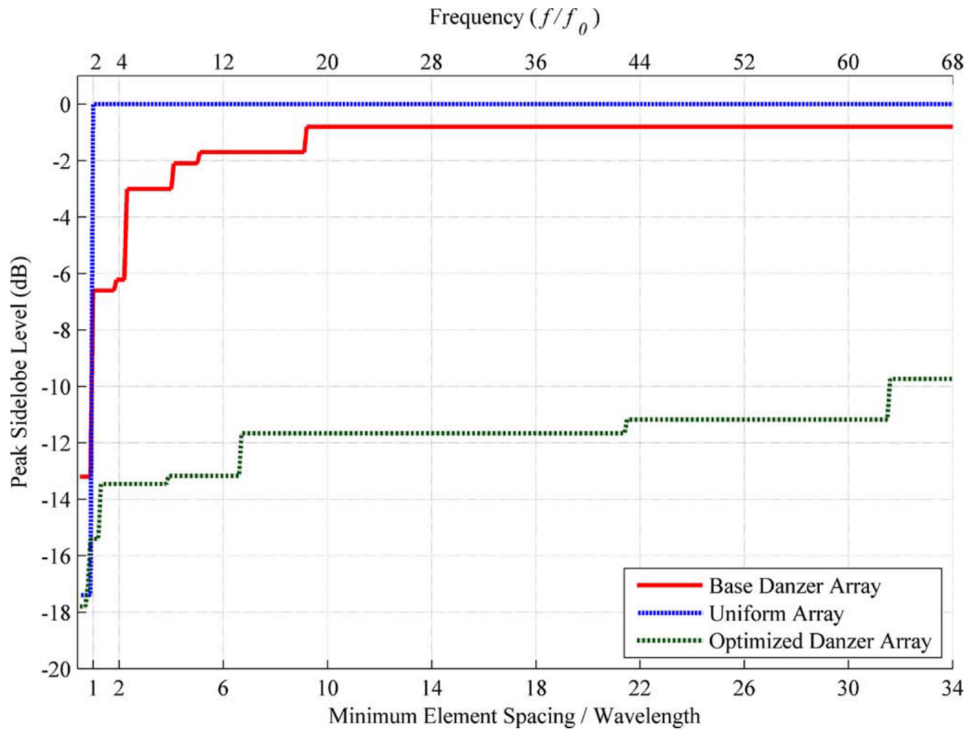

Figure 2.2: Optimized 505-element array SLL designed by genetic algorithm in [14].

It's worth noting that in order to produce usefully low SLL for arrays designed in this way, a very large number of radiating elements are needed, as is visible in fig. 2.1, where 505 elements were optimized. Additionally, by virtue of using genetic algorithms involving a very large number of variables, the operational reconfigurability of such an array is reduced. This is due, specifically, to the long solve-time requirement typically associated with such search methods. A similar field-optimization approach is described in [23] using many fewer elements, albeit with substantially higher SLL, as shown in fig. 2.3.

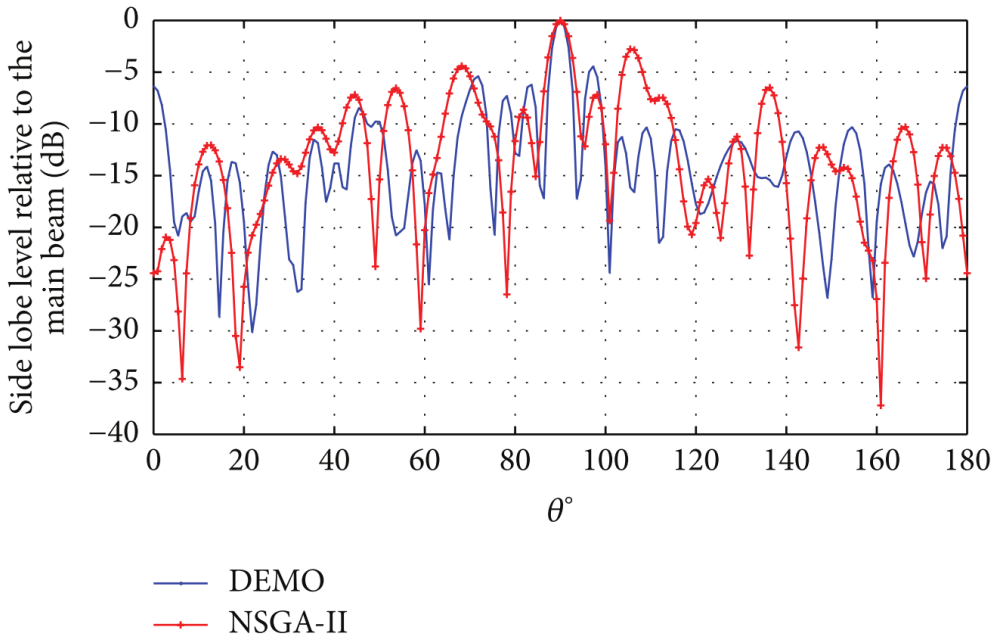

Figure 2.3: Optimized 8-element array. DEMO is the optimal search method proposed in [23].

Following [14], [24] and [25] extend the idea of aperiodic arrays to include random array swarms, which are of course necessarily aperiodic; in doing so, the previous characterization of positional error is transformed into one involving time-varying, indeterminate positioning. In particular, [24] describes how the use of amplitude tapering

and phase modulation may be used to achieve desirable SLL values as show in fig. 2.4. Note once again that the method presented functions most reliably when unconstrained by array size and spread limitations. From here, in the next section, focus will be placed on elements of tight-coupling techniques, in particular those contrasting the characteristics of aperiodic arrays just mentioned.

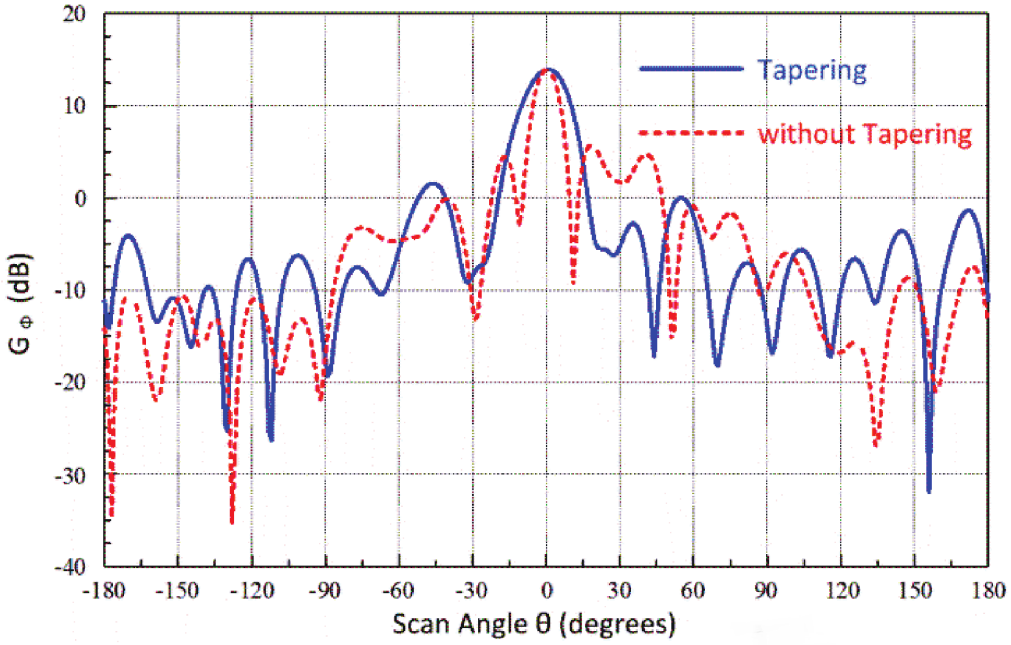

Figure 2.4: Effect on SLL of Amplitude Tapering method proposed in [24].

2.4 Theory of Tightly-Coupled Arrays

2.4.1 Mutual Impedance and Network Theory

In order to properly understand the way in which tight-coupling functions, it's worthwhile to first review some aspects of mutual coupling in general array theory and its relationship to input impedance. Specifically, beginning with two-port network theory, it has long been established, as is shown in [26], that for a two-port network like that

shown in fig. 2.5, the relevant circuit properties are well-defined.

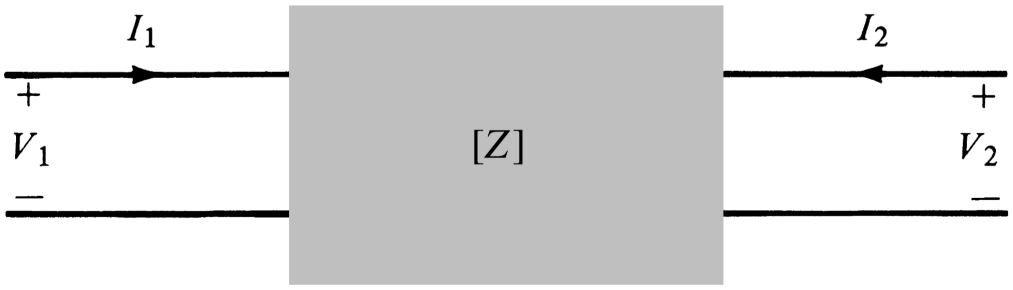

Figure 2.5: Two-Port Network circuit model taken from [24], pg. 468.

The voltage current relations for such a network may be stated as

$$\begin{aligned} V_1 &= Z_{11}I_1 + Z_{12}I_2 \quad \text{and} \\ V_2 &= Z_{21}I_1 + Z_{22}I_2 \quad , \end{aligned} \tag{2.10}$$

where the various Z_{ij} are often referred to as impedance parameters or Z-parameters. These equations can clearly be extended to the more general N-port case by now defining the i^{th} port voltage such that

$$V_i = \sum_{j=1}^{N} Z_{ij}I_j \quad . \tag{2.11}$$

Using circuit model approximations, it is often possible to derive values for these parameters by rearranging the above relations to state that

$$Z_{ij} = \left.\frac{V_i}{I_j}\right|_{I_n = 0 \,\forall\, n \neq j} \quad . \tag{2.12}$$

Here, a zero-valued port current corresponds to that same port being held open to prevent current flow, or in other words, an open-circuit. In the case of antennas, particularly in the context of arrays, these parameters are often referred to as self- and mutual

impedances; an impedance Z_{ii}, for example, is then defined as the i^{th} element's self-impedance in said space, independent of any mutual coupling effects. Therefore, Z_{ij} with $i \neq j$, is by contrast the mutual impedance of the i^{th} element due to the j^{th}, or rephrased, the variation in the i^{th} port voltage due to the j^{th} port current. An N-element antenna array can then be said to have an N-by-N impedance matrix, Z_{mn}, defined such that

$$Z_{mn} \equiv \begin{bmatrix} Z_{11} & Z_{12} & \dots & Z_{1N} \\ \vdots & \ddots & \ddots & \vdots \\ Z_{N1} & \dots & \dots & Z_{NN} \end{bmatrix} \quad . \tag{2.13}$$

Finally, the driving-point impedance of an antenna element, $Z_{d,i}$, is typically then defined such that

$$Z_{d,i} \equiv \frac{V_i}{I_i} = Z_{ii} + \sum_{j \neq i} Z_{ij} \frac{I_j}{I_i} \quad , \tag{2.14}$$

an equality clearly found by dividing the i^{th} voltage in equation (2.11) by the i^{th} current. Qualitatively speaking, the driving-point impedance, also referred to as the input impedance, is that to which any connecting transmission line will need to be matched, being a numeric representation of both the individual element's structure, as well as that of the element's radiative environment.

For moderately complex arrays, whether in size or element topology, circuit approximations are often insufficiently precise to determine an array's impedance matrix; in such cases, other strategies, such as the Method of Moments discussed in Chapter 4, will be necessary.

2.4.2 On Tight-Coupling in Standard Arrays

The designs of traditional phased arrays and aperiodic sparse arrays, unlike tightly-coupled arrays, seek to minimize the role of mutual impedance, in line with the general observation that the effects of such are predominantly detrimental to array performance. This design process typically begins by selecting and optimizing a single representative antenna element, before introducing it into an array setting. Array techniques such as periodicity, sparsity, and phase control are then implemented to limit the de-tuning of the $already$ tuned element, now within an impedance environment very different from free space. Tight-coupling, by contrast, seeks the opposite. In particular, the main principle of tight-coupling is in the utilization of the impedance environment created by an array to not only impedance-tune the array elements, but often extend the array's bandwidth well beyond that of the individual element. This technique, unlike the others mentioned thus far, typically employs un-optimized elements, relying on the introduction of the element into the array's coupling environment to improve element performance and bandwidth.

One of the early studies on the application of tight-coupling to full-scale arrays was conducted by [27] where a unique type of Foursquare antenna, shown in fig. 2.6, is characterized and implemented into a tightly-coupled array.

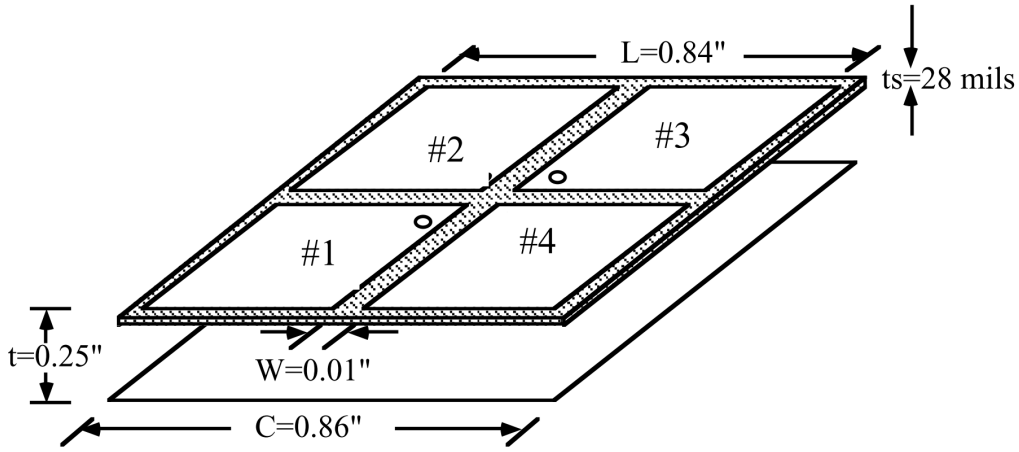

Figure 2.6: Model of planar "Foursquare" antenna used to build array in [27], pg. 48.

By controlling the geometric properties of a 3x3 array of Foursquare antennas, Buxton in [27] is able to affect the magnitude of mutual impedance present in the array, and by extension, both the impedance bandwidth and center frequency of the array. This strategy was then re-attempted using an approximate, FDTD-based approach in [27], with some of the results displayed in fig. 2.7-2.9.

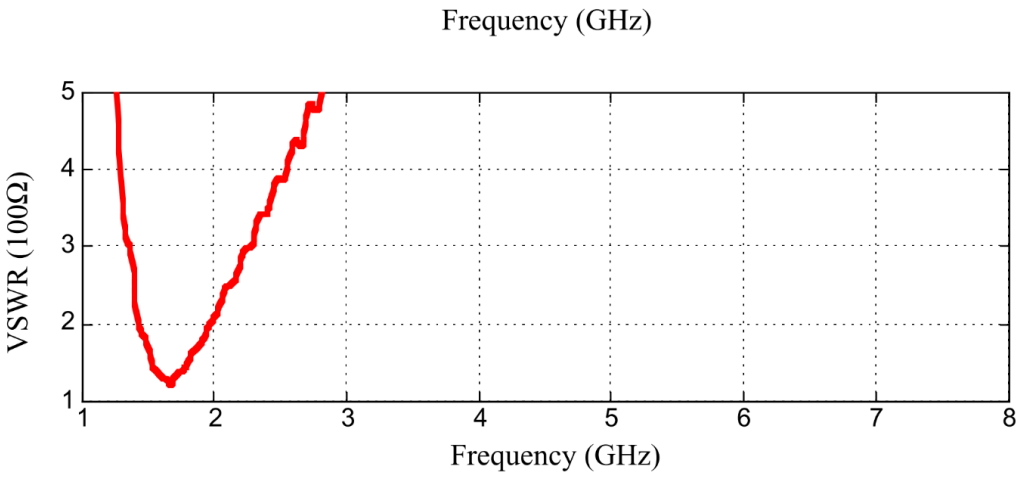

Figure 2.7: Geometry Configuration II - 35% Bandwidth for 100Ω VSWR in [27], pg. 115.

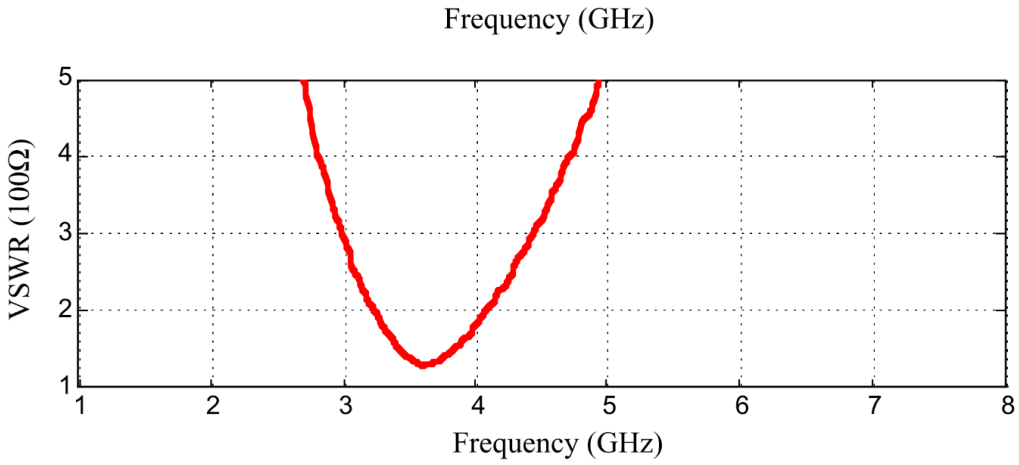

Figure 2.8: Geometry Configuration III - 25% Bandwidth for 100Ω VSWR in [27], pg. 116.

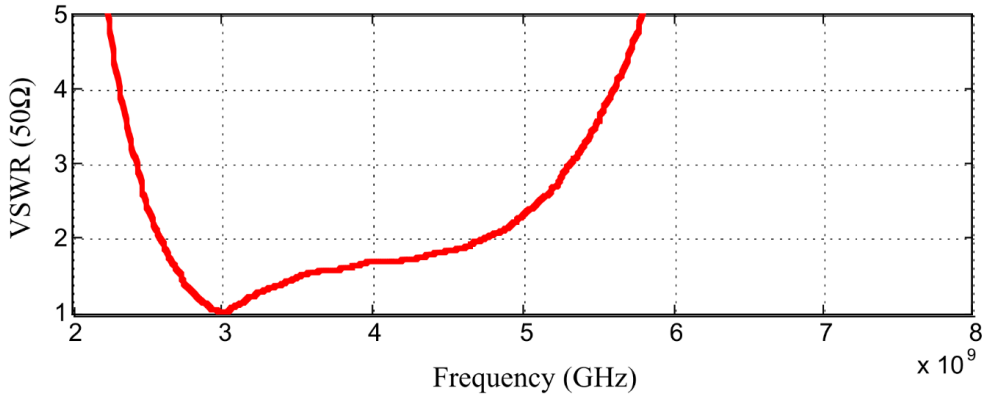

Figure 2.9: Geometry Configuration V - 58% Bandwidth for 100Ω VSWR in [27], pg. 118.

Additionally, by making positive use of the mutual impedance present, [27] was able to reduce the inter-element spacing necessary for a particular impedance bandwidth, allowing for the creation of more compact arrays.

Later on, this topic was further expanded upon in [28], sparking a great number of new studies in the area of ultra-wideband (UWB) antenna arrays, as demonstrated

in [29]–[38]. In detail, [28] describes how the method of tight-coupling essentially seeks to counteract the narrow impedance bandwidth of its elements via the introduction of additional reactances with opposite spectral behavior. In this way, the undesirable impedance of one element may be intentionally negated by that of a collection of other elements or electromagnetically-relevant structures. As an example, [28] goes on to describe how the impedance behavior of a classic dipole antenna, which is capacitive at frequencies below resonance and inductive at those above, as shown in fig. 2.10, may be brought close to match for an extended bandwidth using the parallel combination of a ground plane and free space (when seen through a dielectric layer acting as a $\frac{\lambda}{4}$ impedance inverter). The individual impedance behaviors of these two structures as well, are shown below in fig. 2.11 and fig. 2.12.

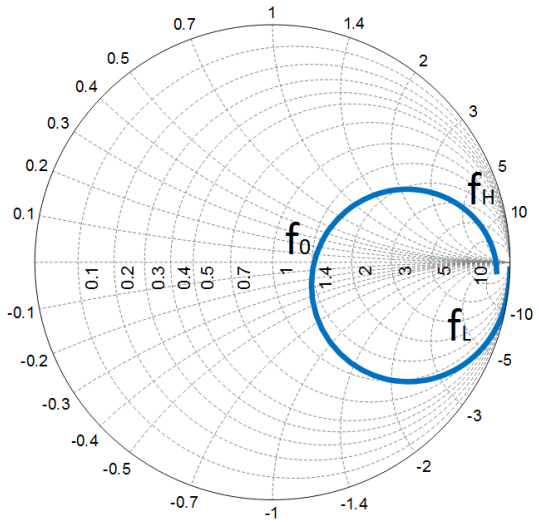

Figure 2.10: Impedance behavior of thin-wire dipole antenna designed in FEKO, 0.1-2.0GHz. Note the locations of the low and high frequencies. Reactive portion will be referred to as X_A.

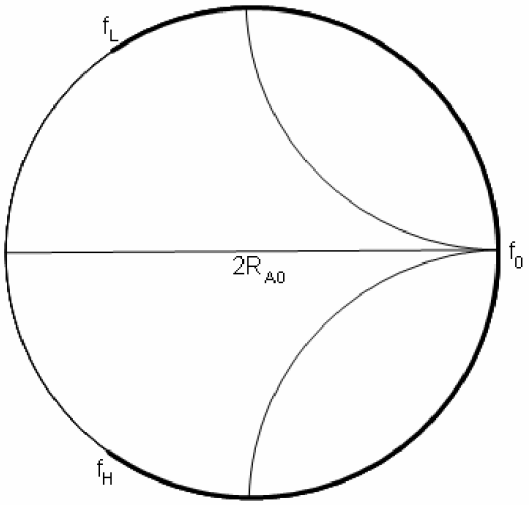

Figure 2.11: Impedance behavior of ground plane spaced by $\frac{\lambda}{4}$ away from antenna. Taken from [28]. Will be referred to as Z_1^+.

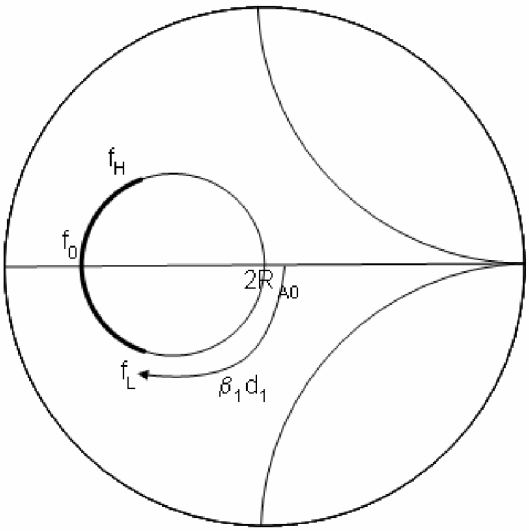

Figure 2.12: Impedance behavior of free space seen from antenna through a dielectric sheet acting as a $\frac{\lambda}{4}$ impedance inverter. Taken from [28]. Will be referred to as Z_1^-.

In using smith charts to visualize how the impedances of these three structures behave

around resonance, it becomes clear how a useful combination thereof could make for a broadband match. Inspecting the low and high frequency regions specifically, the reflection behavior of the ground plane very usefully diametrically opposes that of the dipole and the dielectric sheet, allowing for mutual negation. The resulting broadband match is visible (gray trace) in fig. 2.13.

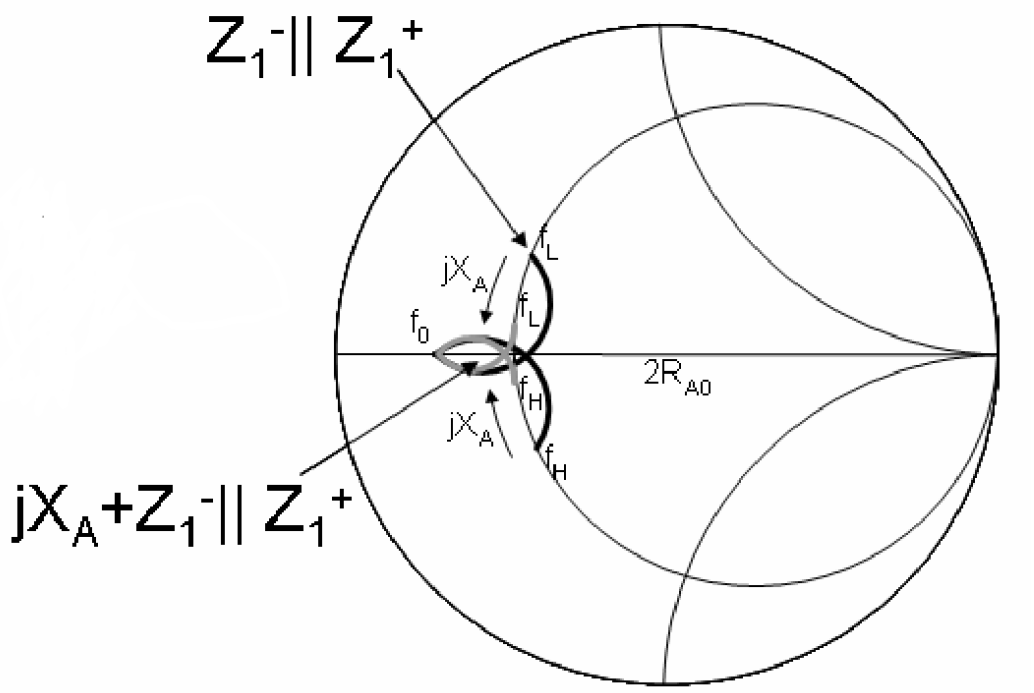

Figure 2.13: Broadband match created by careful impedance balancing. Note that the parallel combination of ground plane and dielectric sheet is in black, while the aggregate of all three is in gray. Taken from [28].

On the level of an array, inter-element coupling also comes into effect in the form of element spacing. Closely spaced series dipoles allow the dipoles' ends to couple capacitively, while parallel dipoles brought near enough may of course inductively couple. Additionally, [28] demonstrates an additional mode by which to add reactance, specifically capacitance, to a dipole array, employing inter-digital coupling between dipole

elements, as shown in fig. 2.14. This added method creates strong inter-element coupling, allowing greater control over the impedance environment seen by each dipole's terminals.

Figure 2.14: Interdigitally-coupled dipole array making use of tight-coupling. Taken from [28].

In summary, a few major aspects of tightly-coupling are worth reiterating. Firstly, in order to take advantage of tight-coupling as a technique, it is of course critical to have precisely characterized the spectral impedance behavior of not only the array elements to be used, but also the reactive mechanisms by which the broadband match will be created. In [28], these included ground planes, dielectric layers, and inter-digital capacitances; a multitude of other structures could be used, however, and it is necessary to understand the behavior of such. Secondly, it is inevitable that element spacing, given the compact nature of tightly-coupled arrays, will be one of these mechanisms. As such, it is often advantageous to regard this element spacing as a form of variable impedance

control, rather than as only a quantity extremized for the sake of maximizing array scan angles. Having stated this, however, it is simultaneously true, as previously mentioned in [27], that arrays making use of tight-coupling can in fact, sometimes be made more compact than traditional arrays, as the effects of mutual impedance are exploited rather than evaded. Finally, it will be necessary, as was the case in [28], to evaluate both capacitive and inductive mechanisms that cover the entire band(s) of interest. A single mechanism of course need not itself be only capacitive or only inductive over all such bands, but at every relevant frequency, some capacitance source and some inductance source must exist for a broadband match to be made.

2.4.3 Application to SUAS

In moving to a theoretical tightly-coupled SUAS-based array, a couple of considerations and adaptations must be made. Of primary concern is the category of aircraft to be used in modeling each SUAS element, along with the placement and style of antenna on said element, as all subsequent work will hinge upon these choices. Additionally, as was stressed in the previous section, the choice of coupling mechanisms will also be of great significance. To this end, for the purposes of this thesis, fixed-wing UAV aircraft, like those shown in fig. 2.15, will be used as both the modeled aerial platform, as well as the radiating bodies themselves.

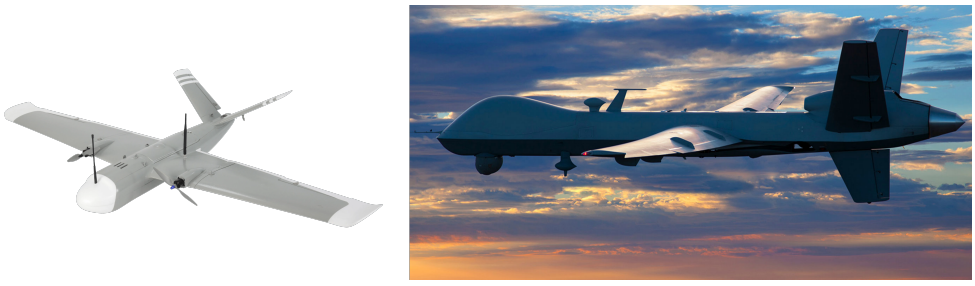

Figure 2.15: Examples of fixed-wing UAV. Left: SP7 Fixed Wing Drone. Right: MQ-9 Reaper.

In this way, by using the entire outer surface of the fixed-wing structure as a contoured, conductive sheet, the array element calculation complexity may, in a manner, be reduced, as the presence of parasitic conductances, namely defective ground planes, will be eliminated. Naturally though, this choice will make the excited portion of each element more complex; this complexity trade-off, however, does yield other, further advantages useful for array design. Specifically, by allowing the entire, metallized surface of the aircraft to radiate, omni-directional patterns, an essential property in the design of highly re-configurable, free space arrays, are much more easily achieved. Omni-directionality, in particular, permits fewer and narrower nulls, meaning a greater number of array configurations is possible; for SUAS, this property is especially beneficial as, from an aerodynamic viewpoint, a single UAV will likely only have a limited range of feasible orientations during any given SUAS operation. Consequently, omni-directionality allows multiple aircraft to more simply re-position themselves relative to each other, rather than re-orienting multiple elements such that their near-fields align more compatibly. In other words, the customary trade-off between aerodynamic and electromagnetic function is somewhat alleviated.

Furthermore, by utilizing the entirety of an aircraft's surface, larger antenna apertures are possible, before even accounting for the greater context of the SUAS array.

This of course follows from the fact that each element in the array will have increased electrical size (electrical size roughly follows physical size) for some given operating frequency, an attribute of enormous import, especially at lower operating frequencies, such as around the HF band. Consequently, this increased electrical size will allow each element to operate at higher efficiencies, thus reducing power consumption in already SWaP-constrained arrays. Secondly, as was first pointed out in a discussion by [39], and later improved upon by [40], the soft limit for antenna gain, G, of a radiating structure of given size can be defined such that

$$G \cong \frac{4a}{\lambda} \quad , \tag{2.15}$$

where a is the maximum dimension of the antenna. Gain values above this soft limit require massive degradation in impedance bandwidth, and are almost always undesirable for broadband applications. For the purposes of this theoretical SUAS-based array, this means that by increasing the physical size of each element, the maximum usable gain value can be increased as well, without damaging the element's bandwidth. Additionally, by increasing the SUAS elements' electrical size in this way, the effective volume per unit height is increased, which, according to [41], leads to a decreased antenna quality factor (Q-factor), or in other words increased impedance bandwidth, an antenna's Q-factor being inversely proportional to impedance bandwidth.

Additionally, in order to partially narrow the scope of this thesis, a large simplification will be made regarding the UAV bodies. Specifically, rather than dealing with the electromagnetic behavior of the entire, complex form of a fixed-wing aircraft, only the fuselage of each element will be considered, which will in turn be represented as large-radius, cylindrical dipole antennas, allowing the necessary electromagnetic field and impedance calculations to be carried out with greater ease. In a future work, the

entire aircraft may be considered, viewing the fixed-wing form as a type of crossed dipole with topological perturbations; for this thesis, however, large-radius dipoles will be of sufficient complexity, the necessary coupling mechanisms being more readily apparent. In particular, for a given array of cylindrical antennas, two main forms of inter-element coupling will be prevalent. For the first, consider two co-axial cylindrical antennas, spaced some distance, z, apart. Because these cylindrical antennas have radii comparable both to their lengths, and in some cases to the operating wavelength, the characterization of the end-cap behavior thereof will be unusually important, as both charges and currents will accumulate on said caps rather than vanishing. The first reactive coupling mechanism, consequently, will involve the parallel plate capacitance and inductance between the ends of each pair of co-axially aligned cylindrical antenna elements, represented in fig. 2.16 shown below.

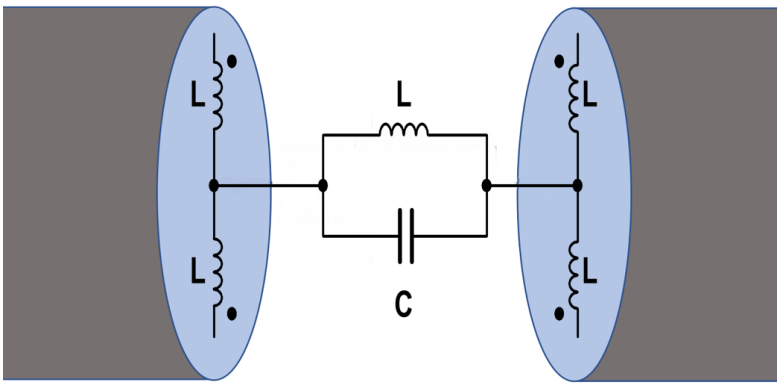

Figure 2.16: Concept of first reactive mechanism via parallel LC circuit in gap region between elements.

This first mechanism will be shown to be predominantly capacitive, as the excess of charge and parallel plate-like geometry at the dipole ends lend themselves to such effects more easily. This can be demonstrated by defining the capacitive reactance, X_C, between the two "plates" specifically, such that

$$X_C = \frac{1}{-2\pi f C} = \frac{-2s}{\pi^2 \epsilon f d^2} \quad , \tag{2.16}$$

where s and d are the plate separation and diameter, respectively. Defined in this way, it becomes clear how a negative reactance will be more dominant, especially at moderately small element separations; the only sources of inductive reactance, by contrast, will be somewhat negligible, resulting from the small, radial current paths on each plate, either converging to, or diverging from, the center of each plate. As a brief aside, it's worth noting that any actual calculation of self- or mutual-inductances between these plates is quite involved, well beyond its capacitive counterpart. If, for example, a static, radially-outward directed, rational current density, J, is defined on one plate such that

$$\bar{J}(\rho) = \frac{2J_0}{\rho d}\hat{\rho} \quad (A/m), \tag{2.17}$$

then the mutual inductance on plate two due to plate one, L_{12}, may be found by noting that

$$L_{12} \equiv \frac{\Phi_2}{I_1} = \frac{\int_{S_2}(\nabla \times \bar{A}) \cdot d\bar{s}}{\oint_0^{2\pi} \bar{J} \cdot d\bar{s}} = \frac{\int_{S_2}(\nabla \times \frac{\mu}{4\pi}\int_{S_1} \frac{\bar{J}}{R} ds) \cdot d\bar{s}}{\oint_0^{2\pi} \bar{J} \cdot \hat{\rho}\rho d\phi} \quad (H), \tag{2.18}$$

where Φ_2 is the magnetic flux through S_2, S_1 and S_2 are the plate surfaces, $\bar{A}$ is the magnetic vector potential, and R is the distance from a differential current source on S_1 to an observation point on S_2. R in this case would defined such that

$$R = \sqrt{z^2 + \rho^2 + \rho'^{\,2} - 2\rho\rho' \cos(\phi - \phi')} \quad , \tag{2.19}$$

where primed and unprimed coordinates indicate location on S_1 and S_2, respectively; note that S_1 has been assumed to be located at $z' = 0$ for simplicity. However, even

with this simplification, as well as that of assuming magnetostatic forms for both $\bar{J}$ and the Green's function in the innermost integral, equation 2.18 for the mutual inductance between the two plates is nonetheless comparable in difficulty, as would be the self-inductance of the entire gap region, to those to be solved via computational methods in later chapters. This difficulty is primarily due to the form of R, and consequently, the integration of similar integrals will become a primary focus in the more general time-varying case.

For the second mechanism, consider these same two cylindrical elements arranged in parallel, or more generally in echelon; in this case, an LC-circuit similar to that of the first mechanism can be used in modeling the reactance between the two antenna lengths. For this mechanism, however, inductance is expected to be the more dominant reactive effect. Using formulas derived in [42] and [43] in fact, a cursory analysis may be quickly made. Specifically, define an inter-element reactance, $X_{parallel}$, such that

$$X_{parallel} = X_C \big|\big| X_L \approx \frac{\cosh^{-1}(\frac{s^2-2a^2}{2a^2})}{-4\pi^2\epsilon f \ell} \big|\big| 2\mu f \ell \cosh^{-1}(\frac{s}{2a}) \quad , \tag{2.20}$$

where s is the axial separation of the elements, a represents element radius, ℓ represents element length, and $\big|\big|$ represents the placement of two impedances in parallel. Here, X_C grows more rapidly than X_L, being proportional to $\cosh^{-1}(x^2)$ rather than just $\cosh^{-1}(x)$, and thus contributes significantly less to the total reactance, per unit variability in X_C and X_L, at even moderate separations. In fact, using the realistic antenna parameters displayed in table 2.1, a clear example of how the reactance defined in equation 2.20 is determined almost exclusively by X_L is visible, as X_C can be easily replaced with an open-circuit with only negligible changes to $X_{parallel}$. While not an especially accurate model of the reactance between two parallel elements, equation 2.20 does provide a general way to predict qualitatively how this second coupling mech-

anism functions. More precise analysis of these mechanisms, however, will be conducted in a later chapter. In the next chapter though, will begin a review of the general theory and behavior of cylindrical antennas, focusing primarily on the less common, large-radius variant.

ϵ	μ	a (m)	s (m)	l (m)	f (MHz)	$X_L(\Omega)$	$X_C(\Omega)$	$X_{parallel}(\Omega)$	$X_{parallel}(2 \times X_L)$	$X_{parallel}(X_C = \inf)$
ϵ_0	μ_0	0.1	5	1	1	8.0859	-1.8409 $\times 10^4$	8.0894	16.1860	8.0859

Table 2.1: Note how the capacitance, X_C, has little effect on the total reactance, $X_{parallel}$.

Chapter 3

Theory of Cylindrical Antennas

3.1 Basic Dipole Theory

3.1.1 Introduction

Being perhaps the simplest of all antennas, in terms of both excitation and electromagnetic field response, the thin-wire dipole antenna has been studied and analyzed ad nauseam, almost every major literary work on antennas usually beginning with the thin dipole as an introductory example. As such, the survey of dipoles reviewed here, while necessary, will be kept as brief as possible, before moving into more rigorous, and consequently less common, analyses of dipoles that will directly aid in the eventual examination of thick dipoles. Additionally, the focus of this section will remain on the methods of analysis themselves, and less so on the actual results obtained therein.

3.1.2 The Infinitesimal Dipole Antenna

The first dipole form worth reviewing is the infinitesimal dipole. Being only a one dimensional structure, and having only minute length, the infinitesimal dipole is useful in demonstrating the general approach by which antennas may be analyzed, whilst minimizing the very real complexity typical of realizable antennas. As with almost

any vacuum electromagnetic calculation, the electromagnetic fields, $\bar{E}$ and $\bar{H}$, will of course be of primary interest. In antenna theory, these are very often found by way of the auxiliary magnetic potential, $\bar{A}$, defined very generally such that

$$\bar{A} = \frac{\mu}{4\pi} \int_V \bar{J} \frac{e^{-jkR}}{R} dV \quad , \tag{3.1}$$

where $\bar{J}$ is the current density distribution, and R relates the source and observation field points. Here in fact, the only limitation on generality is in the use of the the free-space Green's function for Helmholtz's equation, defined in [44]. However, in making use of the various assumptions inherent to the infinitesimal dipole, such as allowing a constant-valued I_z to replace $\bar{J}$ by noting the antenna's small, one-dimensional nature, this generality can be traded for simplicity. In this way, the current distribution has also been assumed to be exclusively axially directed, specifically along $\hat{z}$. After including a few other assumptions, the only remaining non-trivial magnetic vector potential component, A_z, can now be simplified, as

$$A_z = \frac{\mu I_z e^{-jkr}}{4\pi r} \int_{-\ell/2}^{\ell/2} dz' = \frac{\mu \ell I_z e^{-jkr}}{4\pi r} \quad . \tag{3.2}$$

Here, the infinitesimal physical size of the antenna has been used to reduce R to r by treating R as constant over the minuscule radiating length such that $r = \sqrt{z^2 + \rho^2}$. The magnetic and electric field intensities, $\bar{E}$ and $\bar{H}$, can subsequently be found by noting that

$$H_\phi = \left[\frac{1}{\mu} \nabla \times \bar{A} \right]_\phi = \frac{\ell I_z \rho}{4\pi r^2} \left[\frac{1}{r} + jk \right] e^{-jkr} \quad , \tag{3.3}$$

$$E_\rho = \left[\frac{1}{j\omega\epsilon} \nabla \times \bar{H} \right]_\rho = \frac{j\ell I_z \rho z}{4\pi\omega\epsilon r^3} \left[\frac{-3}{r^2} + \frac{-3jk}{r} + k \right] e^{-jkr} \quad , \text{ and} \tag{3.4}$$

$$E_z = \left[\frac{1}{j\omega\epsilon}\nabla \times \bar{H}\right]_z = \frac{-j\ell I_z}{4\pi\omega\epsilon r^2}\left[\frac{-3\rho^2}{r^3} + \frac{-3jk\rho^2}{r^2} + \frac{k^2\rho^2+2}{r} + 2jk\right] e^{-jkr} \quad . \tag{3.5}$$

From here, with respect to the infinitesimal dipole, the next quantity of interest is antenna gain. Making use of the time-averaged Poynting vector, $\bar{W_{av}}$, which can be defined as $\frac{1}{2}\mathrm{Re}\left[\bar{E} \times \bar{H}^*\right]$, where $\bar{H}^*$ is the conjugate magnetic field, the gain of this antenna may then be found such that

$$\begin{aligned} G_{dB} &= 10\log_{10}\left(\frac{4\pi r^2}{P_{in}}\left|W_{av}\right|\right) = 10\log_{10}\left(\frac{4\pi r^2}{2P_{in}}\left|\mathrm{Re}\left\{\bar{E} \times \bar{H}^*\right\}\right|\right) \\ &= 10\log_{10}\left(\frac{I_z^2\ell^2\eta k}{8\pi P_{in}}\sin^2\theta\left[1+\left(k^2-1\right)\sin^2\theta\right]^{\frac{1}{2}}\right) \quad . \end{aligned} \tag{3.6}$$

Here, spherical coordinates are now in use, η is the wave-impedance, and P_{in} is the power input to the system, excluding losses due to reflections along the transmission line. It is, however, vitally important to note that this relatively simplistic gain pattern was only found by excluding a number of the terms in $r^2\left|\mathrm{Re}\left\{\bar{E} \times \bar{H}^*\right\}\right|$, specifically those decaying faster than $\frac{1}{r}$, an action analogous to, but weaker than, the Sommerfeld radiation condition. This simplification, sometimes referred to as the far-field approximation, is of course valid only in a radiator's far-field, where more rapidly decaying terms contribute negligibly to the overall field pattern. Additionally, one other feature of note in this analysis is the way in which it deviates from slightly more standard ones, such as that given in [26]; specifically, by applying the far-field approximation while in cylindrical coordinates, the resulting gain pattern is mildly more complex. The above equation for antenna gain, consequently, hints at some of the subtler frequency-dependent behaviors of the infinitesimal antenna. The gain pattern of the infinitesimal dipole is pictured in fig. 3.1, demonstrating a very nearly isotropic pattern.

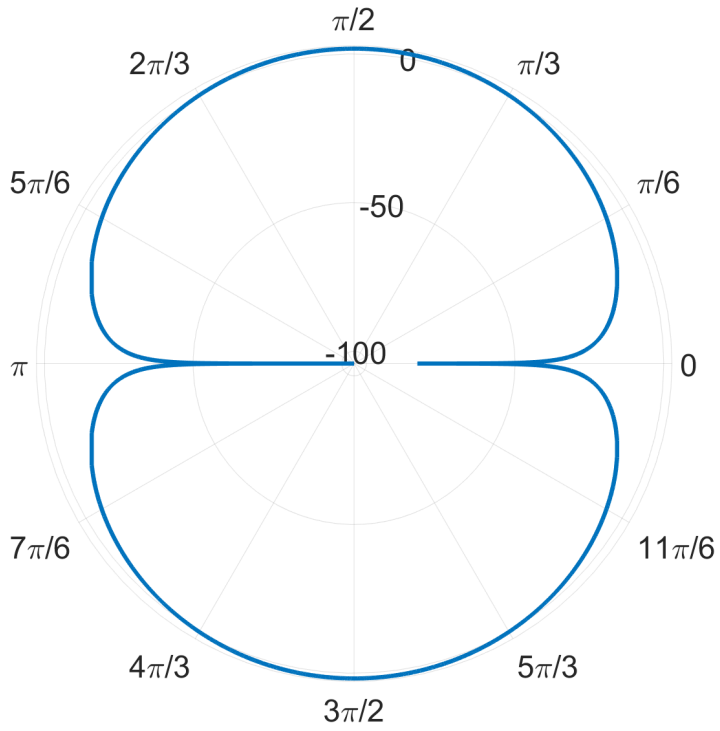

Figure 3.1: Gain (dB) Pattern of $\lambda/1000$ Infinitesimal Antenna Operating at 100 MHz.

Finally, the last relevant element of this infinitesimal analysis is the characterization of radiation resistance. Specifically, as is done in [26], the radiation resistance, R_r, of an antenna will be here defined such that

$$P_{rad} = \frac{1}{2} |I_z|^2 R_r \quad , \text{ where} \tag{3.7}$$

$$P_{rad} \equiv \oint_S \bar{W_{av}} \cdot d\bar{s} \quad , \tag{3.8}$$

S is generally taken to be a spherical surface of arbitrary radius, and R_{rad} is the total power radiated by the antenna. P_{rad} is of course related to P_{in} such that $P_{rad} = e_{cd} P_{in}$, where e_{cd} is the efficiency of the antenna, having losses due to conductive and dielectric heating. When defined in this way, R_r for the infinitesimal dipole is such that

$$R_r = \frac{\pi \ell^2 \eta}{\lambda^2}\left(\frac{2}{15} + \frac{3\pi}{16r}\right) = \frac{\pi \ell^2 \eta}{\lambda^2}\left(\frac{2}{15} + \frac{3\pi}{16N\lambda}\right) \quad ; \tag{3.9}$$

here, the extra $\frac{1}{r}$ term remains due to having taken the far-field approximation while in cylindrical coordinates. Consequently, this form of R_r gives mildly more information than, for example, its counterpart in [26], demonstrating easy observation, if r is taken such that $r = N\lambda$, of the effect of choosing different limiting values for boundary between the radiating and non-radiating near-fields. In particular, it should be noted that, as mentioned in [45], the radiative near-field for a very electrically small antenna has an approximate range of $[\lambda,\ 2\lambda]$. Thus, using (3.9) as the formula for radiation resistance, the formula given on pg. 155 of [26], which states that

$$R_r = 80\pi^2 \left(\frac{\ell}{\lambda}\right)^2 \quad , \tag{3.10}$$

may then be recovered by assuming an N-value of 1.84, meaning the radiation resistance value given by [26] considers all radiated power beyond 1.84λ, when operating at 500 MHz. Alternatively, the formula given in [26] may also be approximately recovered by forgoing the second term in (3.10), or in other words, allowing $r \to \infty$ such that

$$R_r \approx 32\pi^3 \left(\frac{\ell}{\lambda}\right)^2 \quad , \tag{3.11}$$

where $\eta \approx 120\pi\ (\Omega)$.

3.1.3 The Hertzian Dipole

In moving to moderately longer dipoles $\left(\ell \in \left[\frac{\lambda}{50}, \frac{\lambda}{10}\right]\right)$, an additional assumption is needed in order to maintain accuracy, as shown in [26]. Specifically, it will be as-

sumed, though innumerable empirical measurements have approximately verified this assumption, that the current along the length of the dipole is triangular, corresponding to a distribution like that shown in fig. 3.2.

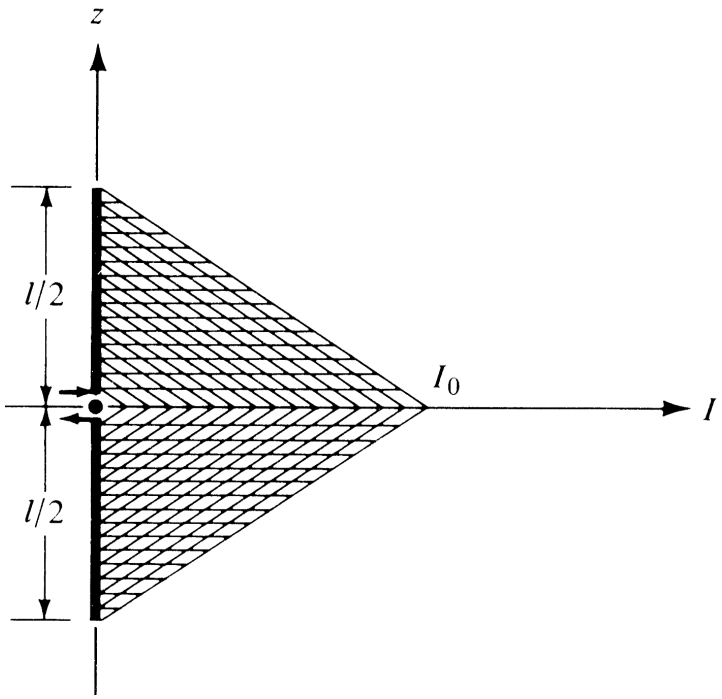

Figure 3.2: Triangular current distribution of Hertzian dipole antenna. Taken from [26], pg. 163.

Using the same analytical process as in the previous section, the Hertzian dipole may be easily inspected, the only distinction being the use of a piece-wise, linear current distribution. In this way, the axial current, A_z, may be found such that

$$A_z = \frac{\mu I_z e^{-jkr}}{4\pi r}\left(\int_{-\ell/2}^{0}\left[1+\frac{2}{\ell}z'\right]dz' + \int_{0}^{\ell/2}\left[1-\frac{2}{\ell}z'\right]dz'\right) = \frac{\mu \ell I_z e^{-jkr}}{8\pi r} \quad ; \tag{3.12}$$

this is exactly one half that of the infinitesimal dipole, which intuitively makes sense,

the relevant triangular current-area being half that of the rectangular constant current-area. The fields, $\bar{E}$ and $\bar{H}$, then naturally possess half the magnitude of those in section 3.1.2, while the Poynting vector, by virtue of its definition, will be one-fourth its previous value. With respect to radiation resistance however, the presence of a non-constant current distribution does necessitate a marginally greater degree of definitional precision. Specifically, because radiation resistance is defined to be inversely proportional to the square of the magnitude of axial current, I_z, it becomes necessary to denote specifically where said current is located on the antenna. Thus, for a wire antenna, radiation resistance, R_r will be defined at the location of maximum current, while the input resistance, R_{in}, will be defined to correspond to the current at the antenna's terminals. In many cases, these two current locations will be identical, especially for symmetric topologies like the center-fed dipole; in the general case with arbitrary excitations, however, this overlap is not guaranteed. Additionally, other resistances, such as that corresponding to the average current value, may of course be defined, but the two defined defined thus far will be of primary focus in this thesis. Following this improved delineation, the radiation resistance of the Hertzian dipole will be one-fourth that of its predecessor, the maximum current value being unchanged.

3.1.4 The Thin-Wire Dipole

Unsurprisingly, the next topic of review, the thin-wire dipole $\left(\ell > \frac{\lambda}{10}\right)$, permits even fewer of the initial infinitesimal assumptions, the most significant of these being the supposed quasi-constant behavior of the quantity R. Specifically, because the antenna is of size comparable to λ itself, R can no longer be presumed independent of the source position $\left(\rho', \phi', z'\right)$, meaning now

$$R = \sqrt{z^2 + \rho^2 + (z')^2 - 2zz'} = \sqrt{r^2 + (z')^2 - 2rz'\cos\theta} \quad , \tag{3.13}$$

where the spherical coordinates (r, θ, ϕ) have been mixed in. In particular, because the integral of a Green's functioning containing the quantity R is no longer trivial, and in fact can often be unsolvable depending on the choice of current distribution, a method by which to overcome this difficulty is needed. A common solution thereof is the generation of approximate series expansions; the form of R lends itself especially well to binomial series.

Binomial series, as discussed in [46] and [47], is a generalization of the binomial theorem, which states that

$$(x+y)^k = \sum_{n=0}^{k} \binom{k}{n} x^{r-k} y^k \quad , \text{ where} \tag{3.14}$$

$$\binom{k}{n} \equiv \frac{k!}{n!(k-n)!} \quad \text{for } k, n \in \mathbb{N}. \tag{3.15}$$

The important distinction between the binomial theorem and its corresponding generalization is in their respective limitations; specifically, the former allows any complex-valued x and y but only non-negative integers for k, while the latter, by contrast, may have any complex k, but requires that $|x| > |y|$. This restriction on the generalization is itself the convergence condition for binomial series, as this generalization, unlike its predecessor, will typically have an infinite number of terms. This in turn is due to the way in which the binomial coefficient, defined in equation (3.15), is itself extended to arbitrary k, as factorials are not typically defined for values other than non-negative integers (though the gamma function can sometimes be used to overcome this limitation). As a result, binomial series is then defined such that

$$(x+y)^k = \sum_{n=0}^{\infty} \binom{k}{n} x^{r-k} y^k \quad , \text{ where} \tag{3.16}$$

$$\binom{k}{n} \equiv \frac{(k)_n}{n!} \quad , \tag{3.17}$$

and $(k)_n$ is the n^{th} falling Pochhammer function of k.

Thus, the quantity R may be represented via binomial series such that

$$R = \left(\left[r^2 \right] + \left[(z')^2 - 2rz' \cos\theta \right] \right)^{\frac{1}{2}} = \sum_{k=0}^{\infty} \sum_{n=0}^{k} \frac{\left(\frac{1}{2}\right)_k}{n!\,(k-n)!} r^{1-k-n} \left(z'\right)^{k+n} \left(-2\cos\theta\right)^{k-n} \quad , \tag{3.18}$$

where an application of the standard binomial theorem has been utilized as well. In this way, the terms of an approximate binomial expansion of R may be easily generated, especially with the aid of symbolic algebra systems, such as those in MATLAB and Wolfram Mathematica. Consequently, the first several terms of this expansion, when rearranged, are such that

$$\begin{aligned} R \approx r - z'\cos\theta + \frac{1}{r}\left(\frac{\left(z'\right)^2}{2} \sin^2\theta \right) + \frac{1}{r^2}\left(\frac{\left(z'\right)^3}{2} \cos\theta \sin^2\theta \right) \\ + \frac{1}{r^3}\left(\frac{\left(z'\right)^4}{2} \left[\frac{5}{8}\sin^2\theta\cos^2\theta - \frac{1}{8}\sin^2\theta \right] \right) \quad . \end{aligned} \tag{3.19}$$

Given that this expansion yields a power series in terms of z' (or a Laurent series in terms of r), the benefit in using this method to approximate R is now quite clear, power series being much more easily integrated than radicals. The desired accuracy of the expansion will then of course be directly determined by the number of terms used; for an

antenna's far-field, the first two terms alone are often considered sufficient. It is worth repeating here that in order for R to be well represented by the above expansion, it is imperative that $|r^2| > \left|(z')^2 - 2rz'\cos\theta\right|$, lest the full binomial series fail to converge. This requisite is easily fulfilled whenever $r \gg z'$, and consequently this expansion is of general use only in the radiating near- and far-fields (Fresnel and Fraunhofer regions) of the antenna.

The second complication in moving to longer dipole antennas is in the form assumed by the current distribution. Being a significant portion of λ lengthwise, it is no longer appropriate, in general, to presume simple current schemes like the constant current or triangular current models. That being said however, for wire antennas whose radii a are sufficiently close to zero ($a \lll \lambda$), it has been empirically found that the current distribution is closely approximated by a sine wave, in a fashion similar to fig. 3.3.

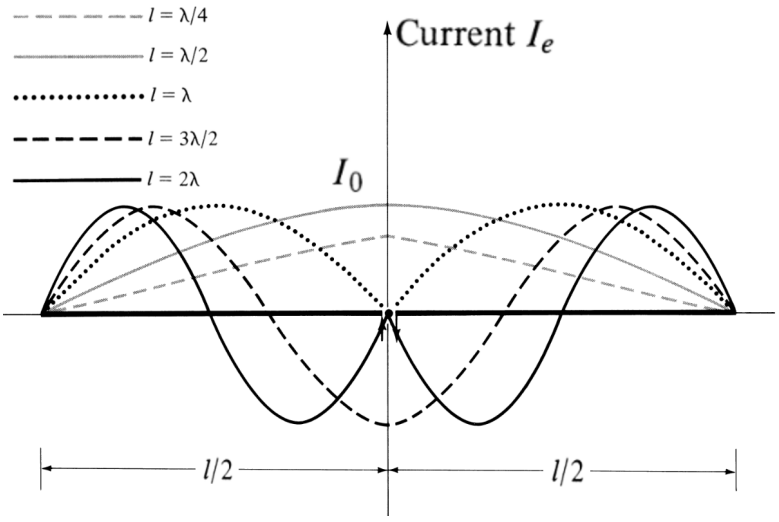

Figure 3.3: Assumed sinusoidal current distribution. Valid when $a \lll \lambda$. Taken from [26], pg. 176.

In the more general case of cylindrical dipoles, however, the aforementioned sine-

wave presumption is not entirely appropriate, and even for very thin dipoles, more accurate analyses may be made by avoiding such assumptions. Consequently, the obvious question becomes what current distribution $should$ be presumed, or better still, how might such an ideal distribution be determined analytically? In the following sections, the development of such an analytical method will be reviewed. Additionally, the now relevant question of antenna excitations will necessarily be addressed.

3.2 Analysis of Thin Cylinders

3.2.1 On The Formulation of R and Other Assumptions For Thin Cylinders

When thin dipole antennas with non-zero radii, which will often be referred to as thin cylindrical antennas, are considered, several adjustments to the form of the magnetic vector potential integral formula, equation (3.1), will necessarily be made. The first of these will be the way in which the current density, $\bar{J}$, is treated. Specifically, as was mentioned in the previous section, the current density along even a quasi-1D dipole antenna is best calculated directly, rather than assumed $a\ priori$. For even slightly thicker cylindrical antennas, this is doubly true. In its place however, a different assumption will be made by utilizing the thin nature of the cylindrical antennas discussed here; in particular, by assuming the current density distribution to be entirely z-directed, or in other words having only components in the $\hat{z}$ direction, the complexity of calculating said current will be drastically reduced. Rephrased, this is to say that said antenna will be of a sufficiently small, cylindrical radius, $(a \ll \lambda)$, such that the antenna may be assumed too thin to host radially or circumferentially directed oscillations. In fact, by presuming this singly-directed current distribution, in coordination with one other as-

sumption, the current density, $\bar{J}$ may be replaced entirely with a scalar axial current, I_z. Here, the aforementioned additional assumption is that of rotational, as well as radial, symmetry; specifically, due to the topological symmetry of the antenna and its corresponding excitation, this presumption regarding azimuthal independence will be able to be leveraged quite frequently.

The next major distinction when analyzing three-dimensional antennas will be in the form of the Green's function used. While the Green's function will maintain the same form with respect to the quantity R, R itself however, being the distance between differential source and observation segments, will require re-examination. Consequently, it will be useful here to discuss how the most general form of R for cylindrical coordinates may be achieved, and subsequently which assumptions may be used to lessen the soon to be accumulated complexity. By inspecting fig. 3.4,

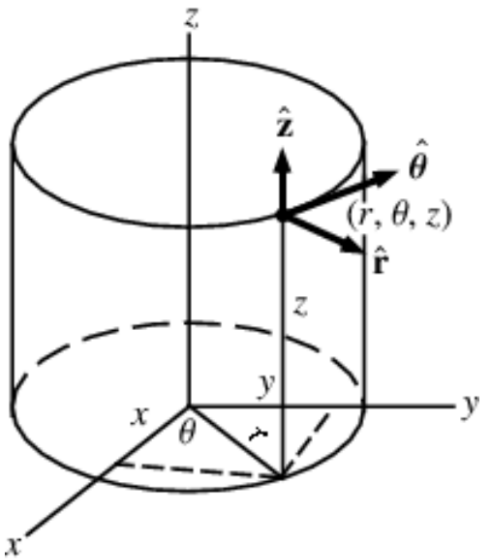

Figure 3.4: Visualization of a cylindrical coordinate system. Taken from [48].

a position vector R_1 for arbitrary (ρ, ϕ, z) may be generated, as

$$R_1 = \rho\cos\phi\hat{x} + \rho\sin\phi\hat{y} + z\hat{z} \quad ; \tag{3.20}$$

here obviously, the R_1 has been held in Cartesian coordinates to avoid the inconstancy of cylindrical unit vectors. Thus, as $R = |R_2 - R_1|$ where R_2 and R_1 are the position vectors of the differential observation and source segments respectively, R may then be expressed such that

$$\begin{aligned} R = |R_2 - R_1| &= |[\rho\cos\phi - \rho'\cos\phi']\,\hat{x} + [\rho\sin\phi - \rho'\sin\phi']\,\hat{y} + [z - z']\,\hat{z}| \\ &= \sqrt{(z-z')^2 + \rho^2 + (\rho')^2 - 2rr'\cos(\phi - \phi')} \quad . \end{aligned} \tag{3.21}$$

From here, using the assumption of small radii ($a \ll \lambda$) once again, ρ' may then be allowed to vanish ($\rho \to 0$) such that

$$R = \sqrt{(z-z')^2 + \rho^2} \quad . \tag{3.22}$$

Proof for the accuracy of this simplification is given in section 1.7 of [49]. When R in this form is substituted back into the free-space Green's function of equation (3.1), that Green's function becomes what is commonly referred to as the $approximate$ kernel of Hallén's equation. By contrast, R in its unabridged form corresponds to the $exact$ kernel.

Finally, given that current density distributions may no longer be assumed, a brief discussion on antenna excitations is necessary, before beginning the derivation of Hallén's equation. With particular respect to dipole antennas, two common forms of excitation are common, with the second one, the magnetic frill source, being purely theoretical. Because, for the purposes of this thesis, the focus will be centered primarily on the determination of largely source-independent impedance matrices of both individual an-

tenna elements, as well as entire arrays, the precise method by which the elements are excited is not of great importance. It is nonetheless useful, however, to at least distinguish, for a given analysis, which excitation is being presently considered such that appropriate comparisons may be made. The first of the aforementioned methods of excitation is the more classical voltage-gap excitation, which presumes some constant voltage, V_0 drop across the antenna terminals, and will be assumed in the following several sections. The magnetic frill source, however, can be of great usefulness at times, as demonstrated in [50].

3.2.2 Derivation of Hallén's Equation

The goal of the section will be the demonstration of how a fairly general equation, from which an axial current I_z may be determined, may itself be derived from Maxwell's equations; this integral equation is most often known as Hallén's equation. As many parts of this section will contain well-worn aspects of electromagnetic theory, the ordering of this section will be based heavily upon the presentations made in [49], [51], [52]. For the sake of continuity, Maxwell's equations may be restated such that

$$\nabla \cdot \bar{E} = \frac{\rho}{\epsilon} \quad , \tag{3.23}$$

$$\nabla \cdot \bar{B} = 0 \quad , \tag{3.24}$$

$$\nabla \times \bar{E} + \frac{\partial \bar{B}}{\partial t} = 0 \quad , \text{ and} \tag{3.25}$$

$$\nabla \times \bar{B} - \mu\epsilon \frac{\partial \bar{E}}{\partial t} = \mu \bar{J} \quad . \tag{3.26}$$

Linear, homogenous, and isotropic material assumptions have of course been made. Thus, noting that $\bar{B}$ is purely solenoidal by equation (3.24), $\bar{B}$ may then, by Helmholtz's

decomposition theorem, be set equal to the solenoidal portion of an otherwise arbitrary vector field, $\bar{A}$, such that $\bar{B} = \nabla \times \bar{A}$. Additionally, because $\bar{A}$ is partially arbitrary, and thus has an unspecified irrotational term, $\bar{A}$ may be defined such that $\bar{A} \equiv \bar{A}_0 - \nabla\psi$, where then $\bar{B} = \nabla \times \bar{A} = \nabla \times \bar{A}_0$. Assuming the vector field $\bar{A}$ to have continuous second derivatives everywhere outside the antenna, $\nabla \times \bar{A}$ may then be substituted into Faraday's law, equation (3.25), such that

$$\nabla \times \bar{E} + \frac{\partial}{\partial t}\left(\nabla \times \bar{A}\right) = \nabla \times \left(\bar{E} + \frac{\partial \bar{A}}{\partial t}\right) = 0 \quad , \tag{3.27}$$

where the order of partial derivatives applied to $\bar{A}$ has been reversed. Here, the sum in the middle portion of equation (3.27) is visibly lamellar, such that it may itself be freely equated, once again by Helmholtz decomposition theorem, to the negative gradient of a scalar field, ϕ, meaning

$$\bar{E} = -\nabla\phi - \frac{\partial \bar{A}}{\partial t} \quad . \tag{3.28}$$

If $\bar{A}$ is then substituted for $\bar{A}_0 - \nabla\psi$, then

$$\bar{E} = -\nabla\phi - \frac{\partial}{\partial t}\left(\bar{A}_0 - \nabla\psi\right) = -\nabla\phi - \frac{\partial \bar{A}_0}{\partial t} + \nabla\left(\frac{\partial \psi}{\partial t}\right) = -\nabla\phi_0 - \frac{\partial \bar{A}_0}{\partial t} \quad , \tag{3.29}$$

where ϕ has been set equal to $\phi_0 + \frac{\partial \psi}{\partial t}$. This last substitution is valuable in and of itself as it demonstrates how the two potential functions defined thus far, $\bar{A}$ and ϕ, may be inter-related, as well as how the assumption of potential functions for $\bar{B}$ and $\bar{E}$ has lead to the creation of an entirely unspecified scalar function, ψ. Specifically, ψ represents a degree of freedom in the treatment of these fields, and will consequently be of paramount importance in defining the Lorenz gauge shortly. In order to define this

Lorenz gauge, however, the degree of freedom represented by ψ must first be utilized; ψ, in particular, will be defined such that

$$\nabla \cdot \bar{A}_0 - \nabla^2 \psi + \mu\epsilon \frac{\partial \phi_o}{\partial t} + \frac{\partial^2 \psi}{\partial t^2} = 0 \quad . \tag{3.30}$$

Satisfaction of this partial differential equation is exceptionally useful as it leads directly to the Lorenz gauge, equation (3.31), by making use of the definitions of $\bar{A}$ and ϕ, or namely that

$$\nabla \cdot \bar{A} + \mu\epsilon \frac{\partial \phi}{\partial t} = 0 \quad , \text{ as} \tag{3.31}$$

$$\nabla \cdot \bar{A} = \nabla \cdot \bar{A}_0 - \nabla^2 \psi \quad , \text{ and} \tag{3.32}$$

$$\frac{\partial \phi}{\partial t} = \frac{\partial \phi_0}{\partial t} + \frac{\partial^2 \psi}{\partial t^2} \quad . \tag{3.33}$$

This established gauge condition is in turn worthwhile, as it functions as a de-coupling mechanism when Maxwell's equations are raised to the second order via substitution of the potential functions such that

$$\nabla \times \nabla \times \bar{A} - \mu\epsilon \frac{\partial^2 \bar{A}}{\partial t^2} + \mu\epsilon \nabla \left(\frac{\partial \phi}{\partial t} \right) = \mu \bar{J} \quad , \text{ and} \tag{3.34}$$

$$\nabla^2 \phi + \frac{\partial}{\partial t} \left(\nabla \cdot \bar{A} \right) = -\frac{\rho}{\epsilon} \quad . \tag{3.35}$$

Specifically, equations (3.34) and (3.35) may be de-coupled such that

$$\nabla \times \nabla \times \bar{A} - \mu\epsilon \frac{\partial^2 \bar{A}}{\partial t^2} - \nabla\nabla \cdot \bar{A} = \mu \bar{J} \quad , \text{ and} \tag{3.36}$$

$$\nabla^2 \phi - \mu\epsilon \frac{\partial^2 \phi}{\partial t^2} = -\frac{\rho}{\epsilon} \quad . \tag{3.37}$$

Finally, using the vector identity that

$$\nabla \times \nabla \times \bar{A} - \nabla\nabla \cdot \bar{A} = -\nabla \cdot \nabla \bar{A} = -\nabla^2 \bar{A} \quad , \tag{3.38}$$

which may be taken as the definition of the vector laplacian in arbitrary coordinates, equation (3.36) is transformed such that

$$\nabla^2 \bar{A} + \mu\epsilon \frac{\partial^2 \bar{A}}{\partial t^2} = -\mu \bar{J} \quad ; \tag{3.39}$$

this equality is typically referred to as the inhomogenous Helmholtz equation.

From here, Helmholtz's equation, along with equation (3.37), where ϕ corresponds to the scalar charge potential, may be simplified by the application of some of the aforementioned assumptions regarding thin cylindrical antennae. Firstly, because all antenna systems mentioned throughout this thesis are strictly linear, and thus no frequency scaling of any kind occurs, the time-harmonic condition, $\frac{\partial}{\partial t} \rightarrow j\omega$, may be introduced into equation (3.39) such that

$$\nabla^2 \bar{A} + k^2 \bar{A} = -\mu \bar{J} \quad , \tag{3.40}$$

where k is once again the operational wave number. Additionally, by assuming a strictly z-directed current density, such that $\bar{J} = I_z$, where I_z is a scalar function of z, the magnetic vector potential will be similarly transformed such that $\bar{A} = A_z \hat{z}$, as the

direction of $\bar{A}$ follows that of $\bar{J}$ by equation (3.1). This transformation is visible when

$$\nabla^2 A_z + k^2 A_z = -\mu I_z \quad . \tag{3.41}$$

By subsequently assuming circumferential symmetry of A_z, and by picking ρ to be $just$ beyond the boundary of the cylindrical antenna, equation (3.41) may then be further simplified such that

$$\left[\frac{d^2}{dz^2} A_z + k^2 A_z\right]_{\rho=a} = -\mu I_z \quad . \tag{3.42}$$

Now, because the voltage-gap excitation model has been used in the preceding analysis, a couple of brief caveats are in order. Firstly, by virtue of assuming a physical gap in the center of the cylindrical antenna, say from $-\delta$ to δ, there exists a small region between the antenna halves through which no current may flow. Consequently, the domain over which equation (3.42) is applicable is reduced from $[-\ell/2, \ell/2]$ by removing this gap region. Additionally, because the excitation is centrally located along the length of the dipole, exclusively even-symmetric current modes will exist, meaning the subsequent analysis, despite being restricted to just the upper half of the antenna, will apply equally well to both halves. Finally, equation (3.42) may be generalized to partially include the effects of conduction loss, as is done in [49], by equating Ohm's law for electromagnetics, which states that

$$\left(\bar{E}_z\right)_{\rho=a} = \frac{1}{\sigma}\bar{J} = \frac{1+j}{2\pi a}\sqrt{\frac{\omega\mu}{2\sigma}} I_z = z^i I_z \quad , \tag{3.43}$$

to the time-harmonic definition of $\bar{E}$, where, due to the Lorenz gauge,

$$\bar{E} = \frac{\omega}{jk^2}\left(\nabla\nabla\cdot\bar{A} + k^2\bar{A}\right) \quad . \tag{3.44}$$

Thus, by forming this equality, the $-\mu$ term of equation (3.42) may be replaced with the more general $j\omega\mu\epsilon z^i$, such that

$$\left[\frac{d^2}{dz^2}A_z + k^2 A_z\right]_{\rho=a} = j\omega\mu\epsilon z^i I_z \quad ; \tag{3.45}$$

here, z^i may be viewed as the surface impedance of the cylindrical dipole, the exact of derivation of which is contained in [53].

In order to continue progressing towards Hallén's equation, a general solution to equation (3.45) will be necessary; from the theory of ordinary differential equations, it is well-established that this may be achieved through the superposition of homogenous solutions, along with a particular solution of the inhomogenous form. The general homogenous solution for differential equations of this sort is well known, where

$$A_{homogenous} = C_1 \cos kz + C_2 \sin kz \quad , \tag{3.46}$$

and where C_1 and C_2 are of course as of yet undetermined. The particular solution is provided by [49], where

$$A_{particular} = j\omega\mu\epsilon z^i \int_{\delta}^{z} I(s) \sin k(z-s) ds \quad ; \tag{3.47}$$

that this particular solution is indeed a solution to equation (3.45) may be verified by use of the general formula for derivatives of a definite integral, which states that when

$$\Psi = \int_a^b f(s,z) ds \quad , \tag{3.48}$$

$$\frac{d\Psi}{dz} = \int_a^b \frac{df}{dz} ds + f(b,z)\frac{db}{dz} - f(a,z)\frac{da}{dz} \quad . \tag{3.49}$$

It is worth noting here that, in order to maintain even-symmetry, $A_{homogenous}$ has its second term negated for the lower half of the antenna, while the lower limit of $A_{particular}$ becomes $-\delta$.

Before synthesizing the full form of Hallén's equation, however, analysis of the charge potential function described in equation (3.37) will allow the determination of one the undetermined constants in equation (3.46). In particular, (3.37) has a time-harmonic form where

$$\left[\frac{d^2}{dz^2}\phi + k^2\phi\right]_{\rho=a} = \frac{1}{j\omega\epsilon}\frac{dI_z}{dz} \quad , \text{ as} \tag{3.50}$$

$$j\omega\rho + \frac{dI_z}{dz} = 0 \tag{3.51}$$

by the principle of charge conservation. Additionally, similar to equations (3.43) and (3.44), the differential equation for scalar charge potential may be generalized to include the effects of surface impedance. This is done by first noting that the Lorenz gauge has a simplified, time harmonic form such that

$$\frac{dA_z}{dz} = -j\omega\mu\epsilon\phi \quad , \tag{3.52}$$

before then re-equating, and subsequently differentiating, Ohm's law with the definition of $\bar{E}$ in terms of the potential functions. Consequently,

$$-\frac{d}{dz}\left(\bar{E}_z\right)_{\rho=a} = \frac{d^2\phi}{dz^2} + j\omega\frac{dA_z}{dz} = \frac{d^2\phi}{dz^2} + k^2\phi = -z^i\frac{dI_z}{dz} \quad , \tag{3.53}$$

where ϕ has similar upper-half solutions defined such that

$$\phi_{homogenous} = j\nu\left[-C_1 \sin kz + C_2 \cos kz\right] \quad , \text{ and} \tag{3.54}$$

$$\phi_{particular} = -kz^i \int_{\delta}^{z} I(s) \cos k(z-s) ds \quad . \tag{3.55}$$

Here, ν is the phase velocity of propagation. The constants C_1 and C_2 are maintained through application of the time-harmonic Lorenz gauge, equation (3.52), which leads to an expected odd-symmetry in the scalar charge potential function. Thus, the voltage-gap, V_δ is then subsequently determined such that

$$V_\delta = \phi(\delta) - \phi(-\delta) = 2\phi(\delta) = 2j\nu\left[-C_1 \sin k\delta + C_2 \cos k\delta\right] \quad , \tag{3.56}$$

which in turn leads to a value for C_2, as now

$$C_2 = \frac{C_1 \sin k\delta - \frac{jV_\delta}{2\nu}}{\cos k\delta} \quad . \tag{3.57}$$

Now, finally, by equating equation (3.1) with the general solution to equation (3.45), Hallén's equation for a thin cylindrical antenna (upper-half only) may be obtained such that

$$\left(\int_{-h}^{-\delta} + \int_{\delta}^{h}\right) I_z(z') K_{thin} dz' = \frac{2\pi}{\eta \cos k\delta}\left[2\nu C_1 \cos\left(k\left[z-\delta\right]\right) - jV_\delta \sin kz\right] + 4\pi j\omega\epsilon z^i \int_{\delta}^{z} I(s) \sin\left(k\left[z-s\right]\right) ds \quad , \tag{3.58}$$

where

$$K_{thin} = \frac{e^{-jkR}}{R} \quad , \text{ and} \tag{3.59}$$

$$R = \sqrt{(z - z')^2 + a^2} \quad . \tag{3.60}$$

The value η is of course the relevant wave-impedance. For the lower half of the antenna, the first of the two terms on the right in equation (3.58), as well as the lower limit on the rightmost integral, are negated. Additionally, when the voltage-gap is assumed to be negligible in terms of physical size such that $\delta \to 0$, equation (3.58) reduces to the more common form, stating that

$$\int_{-h}^{h} I_z(z') K_{thin} dz' = \frac{2\pi}{\eta} \left[2\nu C_1 \cos\left(k\left[z - \delta\right]\right) - jV_0 \sin k|z| \right] \quad . \tag{3.61}$$

From here, as pointed out in [54], C_1 may be determined by making use of another assumption reserved for $thin$ cylindrical antennas, namely that the current distribution vanishes at the ends of the antenna, $I_z(\pm h) = 0$. Interestingly, this assumption also hold for cylinders with semi-spherical end caps. Equation (3.61), consequently, is one of the more common forms of Hallén's equation, which may be used to solve for the approximate current distribution, when used in conjunction with equations (3.59) and (3.60).

3.3 Notes on General Cylindrical Antenna Analysis

The derivation of the previous section does of course come with some significant caveats and limitations, however. In particular, aside from the assumption of a purely

axial, z-directed current distribution along the radiating cylinder, a vital assumption made was that of a thin dipole structure, $(a \ll h)$. If this assumption is restricted, the previously defined K_{thin} quantity is necessarily substituted for K_{thick}, where

$$K_{thick} = \int_{-\pi}^{\pi} \frac{e^{-jkR}}{R} d\phi \quad , \text{ and} \tag{3.62}$$

$$R = \sqrt{(z - z')^2 + \rho^2 + a^2 - 2\rho a \cos(\phi - \phi')} \quad . \tag{3.63}$$

Here, it is important to note that the inclusion of this "exact" kernel into Hallén's integral equation drastically complexifies any potential solution to such an extent that virtually all analytical solutions involve method of moments (MoM) formulations like those described in the next chapter. In fact, while [49] does offer some non-MoM, series solutions to the approximate kernel formulation in equation (3.61), this equation too, is now virtually always solved via MoM-based methods. Nonetheless, a useful series representation of K_{thick}, first presented in [55], is such that

$$K_{thick} = \frac{e^{-jkR}}{R} - jk \sum_{n=1}^{\infty} \frac{(k^2 \rho a)^{2n} (2n-1)!! h_{2n}^{(2)}[kR]}{(2n)! (2n)!! (kR)^{2n}} \quad , \tag{3.64}$$

where $h_{2n}^{(2)}[kR]$ is the spherical Hankel function of the 2^{nd} kind and order $2n$.

Another formulation of Hallén's equation useful for excitation via external, incident waves, often referred to as Pocklington's equation, can be found in [50]. Here,

$$\left(\frac{\partial^2}{\partial^2 z} + k^2\right) \oint_{S'} J_z(\bar{r}') K_{thick}(\bar{r}, \bar{r}')\, dS' = -j\omega\epsilon E_z^i(\bar{r}) \quad . \tag{3.65}$$

In equation (3.64), the presumption of the homogeneity of the z-directed current density, $\bar{J}_z$, with respect to azimuth and radius has notably been dropped.

Chapter 4

The Method of Moments

4.1 General Methodology

Broadly speaking, the Method of Moments is a generalized procedure by which inhomogenous linear equations may be solved. In particular, as is done in [56], consider the general linear form where

$$Lf = g \quad . \tag{4.1}$$

Here, f, g, and L are defined such that $f : U \to V$, $g : U' \to V'$, and $L : V \to V'$ respectively, though it will be assumed herein that $U = U'$. In using moment methods, it is also generally the case that g, being the "system input", is assumed known, while f, being the "system response", is not. Additionally, let f be such that it may be expanded in an infinite series such that

$$f = \sum_n \alpha_n f_n \quad , \tag{4.2}$$

where α_n are as of yet undetermined constants, and f_n are pre-selected basis functions. In the case of time-harmonic electromagnetics, these basis functions are often trigonometric functions, complex exponential functions, Bessel functions, or something simi-

larly useful. It is important to note here that, now that f has been expanded into a series wherein only the constants α_n are undetermined, the subsequent steps described herein will seek to determine the values α_n rather than f directly, as equation (4.2) will yield f from α_n.

Furthermore, the question of whether f may in fact be represented by such an expansion is not necessarily trivial. Because equation (3.61) for example, whether in the approximate or exact form, contains a factor of $\frac{1}{R}$, and is thus prone to singularities near the voltage gap at the center of the cylinder, this question is often, surprisingly, of great import. In fact, attempts to efficiently circumvent the singularities that do arise is a very common theme in MoM-related antenna literature, as can be seen in [50], [57]–[59]. For the sake of computability, equation (4.2) is also typically reduced to an approximate, finite sum of size N, wherein solution convergence is then partially dependent upon the size of this sum.

Subsequently, this sum may be substituted back into equation (4.1), where, by the linearity of the operator L,

$$\sum_n \alpha_n L f_n = g \quad . \tag{4.3}$$

Next, in order to reduce equation (4.3) into a matrix problem from which α_n may be extracted, the known product Lf_n will necessarily be made the argument of a linear functional. Typically, this functional is an inner product defined such that

$$\langle w_m, Lf_n \rangle = \int w_m L f_n dU \quad . \tag{4.4}$$

The function w_m is a "weighting" function, and the choice of such will, like the basis functions, greatly impact the rate at which the end solution for f will converge, as N and M are increased. M is of course the number of unique but related weighting

functions, w_m, used to form an $M \times N$ matrix, although setting M equal to N is also common. As such, more often than not, the functions w_m are either chosen to match the basis functions f_n (Galerkin's method), or are selected to be Dirac delta functions that "sample" Lf_n and g across the domain U (point matching). Thus, in the case of Dirac delta functions,

$$\langle w_m, Lf_n \rangle = \int \delta(m) Lf_n dU = Lf_n \Big|_m \quad . \tag{4.5}$$

This also means equation (4.3) may now be re-written such that

$$\sum_n \alpha_n \langle w_m, Lf_n \rangle = \langle w_m, g \rangle \quad . \tag{4.6}$$

Finally, the constants α_n may then be extracted via inverting, or in some other manner solving, the matrix equation that states

$$\begin{bmatrix} \langle w_1, Lf_1 \rangle & \langle w_1, Lf_2 \rangle & \dots & \langle w_1, Lf_N \rangle \\ \vdots & \ddots & \ddots & \vdots \\ \langle w_M, Lf_1 \rangle & \dots & \dots & \langle w_M, Lf_N \rangle \end{bmatrix} \begin{bmatrix} \alpha_1 \\ \vdots \\ \alpha_N \end{bmatrix} = \begin{bmatrix} \langle w_1, g \rangle \\ \vdots \\ \langle w_M, g \rangle \end{bmatrix} \quad . \tag{4.7}$$

Consequently, the Method of Moments, while not necessarily complex when treated in a generalized manner, does hinge on a few key factors. Firstly, as was discussed above, it is critical to ensure that the function f is unlikely to possess discontinuities or any other abnormalities that would render its representation by way of series expansion invalid. In the case that such an abnormality does appear, efforts to isolate and extract the singularity-causing portion of f are often advisable, as is done in [57], [58].

Secondly, as appropriate choice of basis functions can greatly reduce computation times, it is often useful to choose basis functions close in shape to the expected solu-

tion, when known. To this end, it can also be tremendously convenient to use "subsectional" basis functions, wherein each f_n is non-vanishing for only a small subset of U. Common examples of these include pulse functions, triangle functions, and windowed trigonometric functions like those used in [58], [60], [61]. Additionally, when using subsectional bases, it is interesting to note that the $M \times N$ matrix of equation (4.7), when applied to radiators like those described in equations (3.64) and (3.67), is equivalent to the impedance matrix described in equation (2.13), the cylinder forming an N-port matrix that relates every subsection to every other.

Finally, while point-matching may be an especially convenient choice of weighting function, Galerkin's method does at times hold an advantage, in particular when the basis functions in use have orthogonality conditions over the domain U. This is in fact typical in cases such as Fourier series, or Chebyshev, Legendre, or Laguerre polynomials, etc.

4.2 Intricacies Related to The Modeling of Cylindrical Antennas

In this thesis, because common antenna properties have been assumed, namely properties such as passivity and linearity, a few useful insights regarding the modeling of cylindrical radiators may be noted. Firstly, by virtue of the two aforementioned properties, it can be expected that the response spectrum of such an antenna system will very closely match that of the initial excitation. Consequently, as opposed to using, for example, whole-domain, Fourier series basis terms, wherein a single term, α_i, may be defined such that $\alpha_i = a_i \sin(\omega_i t)$, subsectional basis terms may be quite advantageous. Specifically, while whole-domain α_n will have a single term corresponding to the modeled excitation frequency, every term in subsectional α_n will be at the appropriate frequency, in a form similar to $\alpha_i = a_i \sin(\omega t) w_i(t)$, where $w_i(t)$ is an arbitrary

windowing function. Further advantages of subsectional bases are discussed in [58], where particular focus is placed on the limited accuracy of whole-domain techniques with respect to electrically shorter, thicker cylinders.

Additionally, as one considers the specific strategy by which to model a cylindrical antenna, the electrical and relative proportions of the antenna become a significant factor. In particular, as the electrical size, length-to-radius ratio, and subsection, or "mesh", size of the cylinder shrink, significant limitations and restrictions may become relevant. Specifically, if one were to take the operator L as the integral of equation (3.64), wherein the simpler, approximate kernel is utilized, the approximate nature of K_{thin} would greatly affect the accuracy of any solution to the currents on the cylinder. The bounds suggested in [58] are such that use of K_{thin} should be limited to cylinders where

$$\frac{\Delta}{a} \geq 10 \quad and, \tag{4.8}$$

$$\frac{\lambda}{a} \geq 100 \quad . \tag{4.9}$$

Here, Δ is the size of a single subsection, and a is of course the cylinder radius. These bounds prevent the radius from becoming large relative to either the excitation wavelength or the subsection size, at which point the accuracy of K_{thin} has been shown to be minimal. Further restrictions are of course implicit in the aforementioned ones, as a sufficient number of subsections are required in any moment method in order to ensure accuracy. Thus, as the radius, a, becomes larger, it becomes increasingly necessary that

$$\frac{L}{\lambda} \not< 0.5 \quad and, \tag{4.10}$$

$$\frac{L}{a} \not< 100 \quad , \tag{4.11}$$

lest the previous limitations be encroached upon. L, here, is the length of the cylinder in question.

Utilization of the kernel in equation (3.67), K_{thick}, will of course, by contrast, obviate the need for any of these restrictions, as it represents the "exact" kernel to Hallén's equation, maintaining only a few of the initial assumptions made early in the derivation of Hallén's equation. This increase in accuracy does, however, naturally come with a tremendous increase in complexity; the nature of analytical solutions under such added complexity is visible in works such as [58], [60], [61]. Even so, the model studied in [60] and [61] is of particular value as it also takes into account the ramifications of charges collected at the end caps of the radiating cylinder, in addition to axially-directed current distributions. As this thesis concerns itself with the study of the serial coupling between coaxially-aligned cylinders, this added consideration would understandably be immensely useful. However, at this point, while the combined works of [60] and [61] do present an extremely comprehensive analysis of the cylindrical radiator, the computational costs of utilizing closed-form analytical solutions become more relevant. In particular, many of the numerous integrals involved in [60] are necessarily solved via intricate series solutions; many of these series solutions, in turn, converge rather slowly relative to their purely numerical counterparts. In fact, in comparison to the speed of common commercial electromagnetic solving software like Ansys HFSS or CST, such analytical methods are highly impractical, presenting less converged solutions in a greater amount of time. This problem is then, of course only exacerbated by

extending the analysis to an array of large-radius cylinders. Consequently, the remainder of this thesis, starting in chapter 5, will focus exclusively on analyses performed in Ansys HFSS.

Chapter 5

Trends in the Singular Thick Dipole

5.1 Degradation in Impedance Behavior

As discussed at the end of the previous chapter, because of the tremendous complexity involved in seeking purely analytical solutions to the fields of not only individual cylinders with substantial radii, but also cylindrical antenna arrays, the results demonstrated herein will be taken from simulations built in Ansys HFSS. Furthermore, when discussing cylindrical antennas, it is rather useful to highlight how the behavior of such antennas is related to, and deviates from, that of more idealized wire antennas. In fig. 5.1, for example, the impedance behavior of an ideal dipole is shown, where the half-wave behavior (at 3 MHz) is around the expected value.

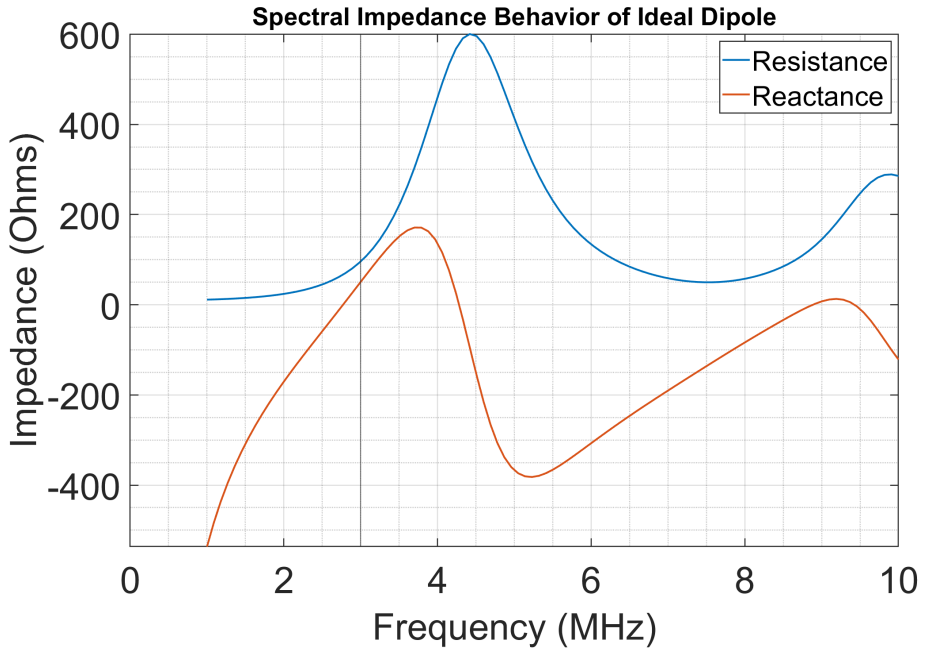

Figure 5.1: Spectral Impedance Behavior of an Ideal, Half-wave (at 3 MHz) Dipole

However, as shown in fig. 5.2 and 5.3, these same curves change drastically as the radius of the wire antenna grows with respect to the dipole's length. The first observation to be made here, in fig. 5.2, is how both the peak resistance and that corresponding to a half-wavelength (3 MHz) drop off rather rapidly as the antenna radius grows, or equivalently, as the length-to-radius ratio shrinks, the metric used in the legend in fig. 5.2 and 5.3. Understandably, this trend is troublesome for most applications for a number of reasons. In particular, this trend will be most problematic for performance metrics like radiation efficiency and mismatch loss. As is described in [26], radiation efficiency, e_{cd}, is such that

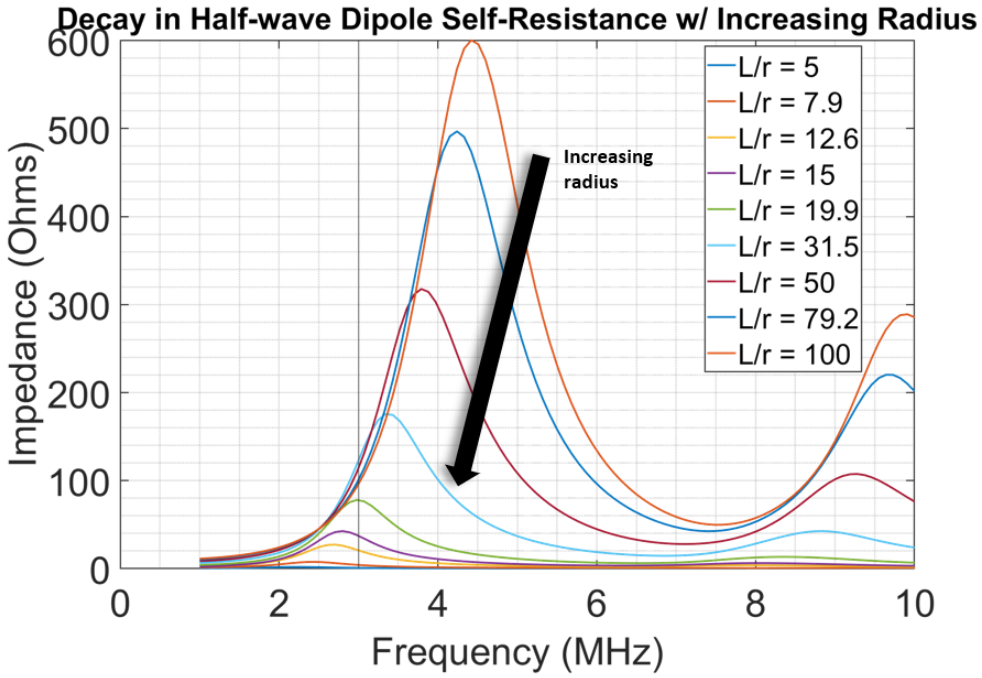

Figure 5.2: Degradation in Resistance of a Half-wave (at 3 MHz) Dipole

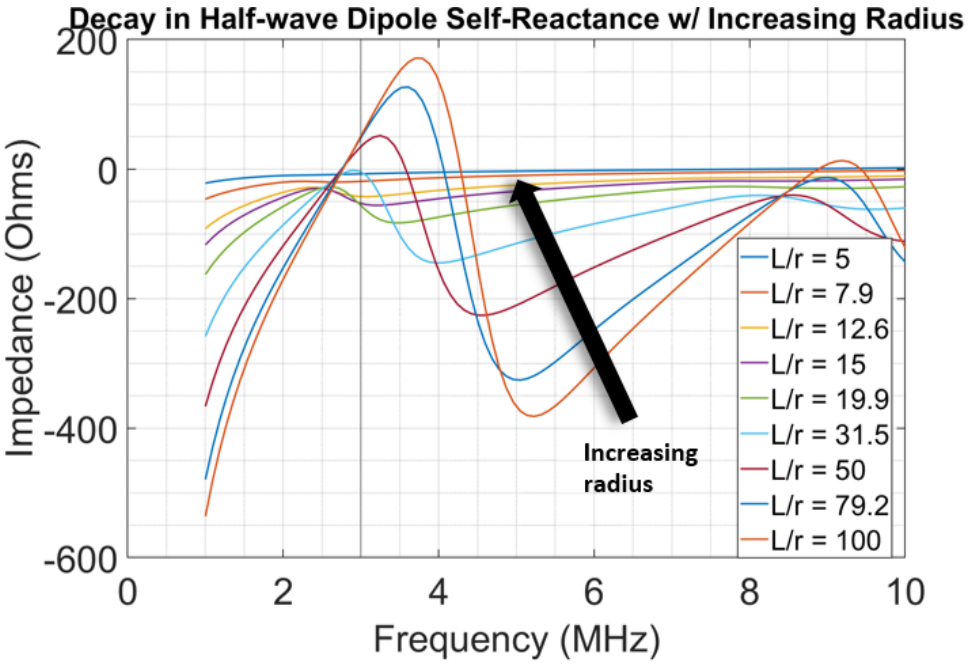

Figure 5.3: Degradation in Reactance of a Half-wave (at 3 MHz) Dipole

$$e_{cd} = \frac{R_r}{R_r + R_L} \quad , \tag{5.1}$$

where R_r is the same radiation resistance as shown in fig. 5.1 and 5.2, and R_L is the equivalent loss resistance due to the thermal dissipation of energy in the antenna's conducting and dielectric materials. Thus, as the radiation resistance of the cylindrical antenna drops, even if the antenna can still be matched to some low-impedance system, the radiation efficiency of the antenna would nonetheless continue to plummet. This in turn of course means an increase in the amount of waste heat present in the system, indicating poor use of the system's available resources. Additionally, for the majority of more realistic systems which cannot be easily designed to have arbitrarily small characteristic impedance, the mismatch loss between the antenna and system will also grow rapidly.

A readily obtained, albeit somewhat simplified, explanation for this behavior is possible by relating the current paths along the surface of a cylindrical dipole to the lumped resistors found in basic circuit theory. Specifically, if one pictures the ideal, infinitesimally thin, half-wave dipole, wherein only a single current path exists, as a singular, high-valued resistor (the reactive portion of the dipole being momentarily ignored), then a thicker, cylindrical dipole may in turn be viewed as any number of similar resistors, connected in parallel, as a large number of parallel current paths exist on the surface of a thick cylinder. Additionally, as the "resistance" of these current paths is primarily determined by said path's length, it is understandable how the cumulative effect of these parallel paths is to reduce the "equivalent resistance" of the overall cylinder, analogous to the behavior of parallel resistors in elementary circuit theory. Thus, this also explains the asymptotic behavior of the cylinder's resistance as it drops toward zero with increasing radius, as, in the lumped case,

$$\lim_{N\to\infty} \sum_{i=1}^{N} \left[\frac{1}{R_i}\right]^{-1} = 0 \tag{5.2}$$

with asymptotic decay. Similarly, with respect to reactances, hypothetical, parallel capacitors and inductors may of course be conceived. In this case, the change in frequency behavior in fig. 5.3 is reasonably explained by way of analogy to lumped components once again. In particular, as capacitances and inductances act oppositely when situated in parallel, it is easy to imagine how, with increasing cylinder radius, the resultant effects on the cylinder's effective capacitance and inductance will also be opposites. Consequently, the overall cylinder reactance will of course be affected, as the ratio $\frac{Z_L}{Z_C}$ will change proportionally to LC, L now being the cylinder's effective inductance.

Furthermore, as the electrical length of this single dipole shrinks, it is to be expected that the antenna's total resistance would shrink even more, as the current paths' lengths will naturally be reduced. Therefore, as is visible in fig. 5.4, it is clear that a cylinder with a length of $\lambda/20$ would be expected to have minimal radiation resistance, making it a very poor radiator in isolation. In fig. 5.5, similar effects of short electrical length are present; namely, the relatively flat, monotonic spectral behavior observed is easily explained by the inability of such an electrically small structure to support resonant modes anywhere in the tested band.

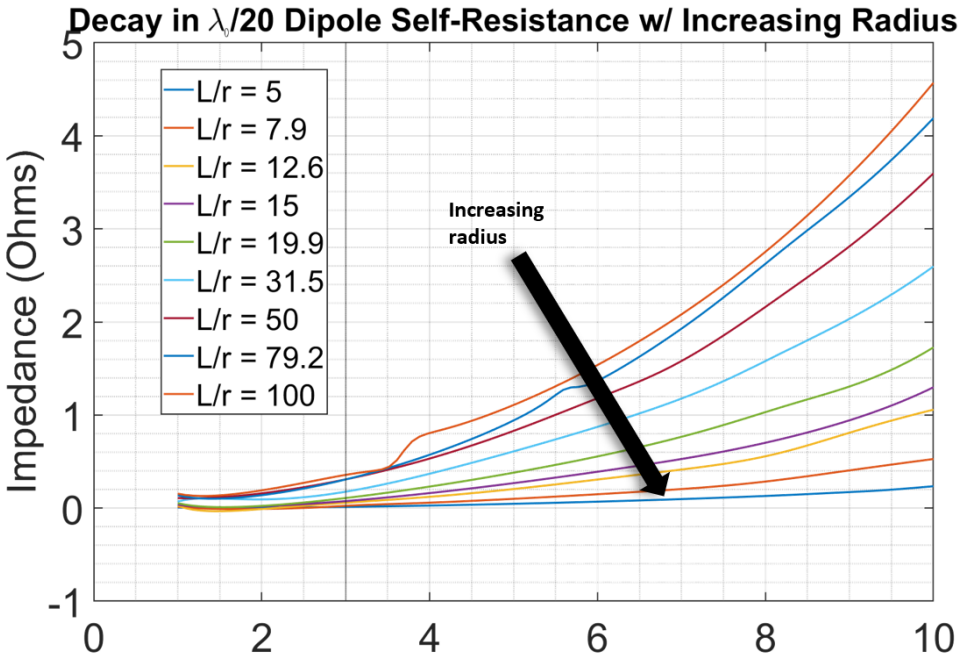

Figure 5.4: Degradation in Resistance of a $\lambda/20$ (at 3 MHz) Dipole

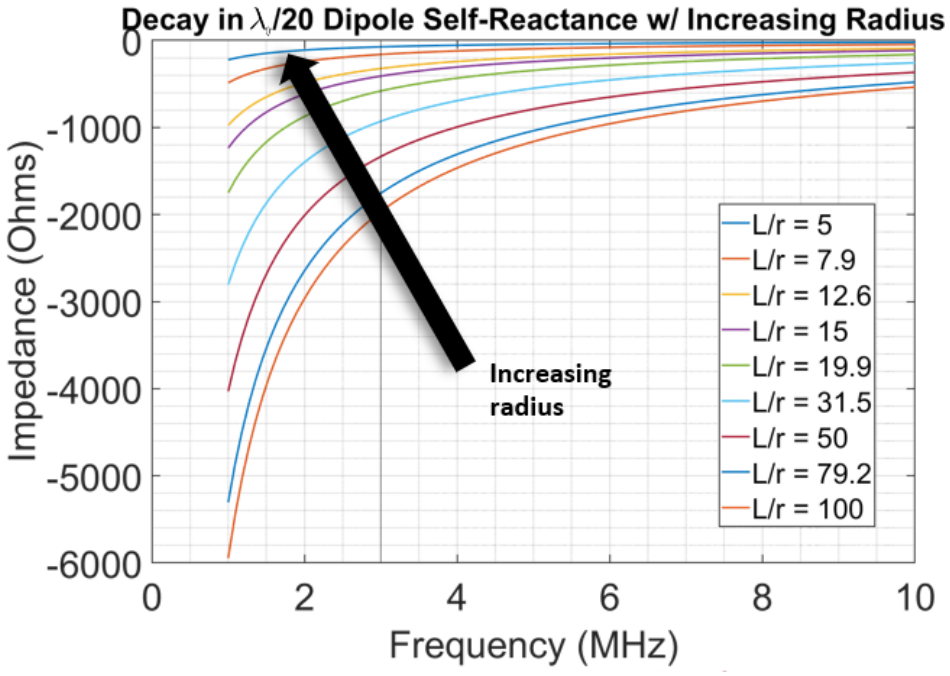

Figure 5.5: Degradation in Reactance of a $\lambda/20$ (at 3 MHz) Dipole

In summary, as is visible throughout this section, any move away from the ideal, half-wave dipole towards a more cylindrical radiating body serves as a detriment to performance. In particular, the hardest-hit property is that of radiation resistance. In terms of performance, this defect will naturally manifest as poor radiation efficiency and increased return loss. Thus, it is these two performance factors that will be of central importance moving forward, and, in the context of tightly-coupled dipole arrays, it will be these negative trends that this thesis aims to counter.

5.2 Introduction of Total Efficiency

As was discussed in the previous section, losses due to heating and mismatch are of primary importance in the coming analyses. Consequently, in this section, a somewhat more atypical metric will be introduced that effectively combines the two types of loss into a more useful, single parameter, namely total efficiency. In particular, radiation efficiency, in addition to the definition presented in equation (5.1), is also often defined such that

$$e_{cd} = \frac{Radiated\ Power}{Delivered\ Power} \quad where, \tag{5.3}$$

$$\tag{5.4}$$

$$RadiatedPower = \frac{1}{2} \oint_S Re\left[\bar{E} \times \bar{H}^*\right] dS \quad . \tag{5.5}$$

Mismatch efficiency is, by contrast, typically such that

$$e_m = \frac{Delivered\ Power}{Incident\ Power} \quad , \tag{5.6}$$

which in turn means that total efficiency is easily defined so that

$$e_{tot} = \frac{Radiated\ Power}{Incident\ Power} = \frac{Radiated\ Power}{Delivered\ Power + Reflected\ Power} \quad . \tag{5.7}$$

Applying this new metric to the data presented in section 5.1 tells a clearer story of the previously discussed trends. In particular, as can observed in fig. 5.6, the total efficiency for varying cylinder dimensions is now a single metric through which the performance of later arrays may also be measured, without concern about the individual impedances and port parameters of each element in the array. In other words, total efficiency here gives a clear measurement regarding the ability of any radiating aperture to efficiently radiate, relative of course to some characteristic system impedance (typically 50 or 75 ohms). Returning to fig. 5.6, it is evident that the most significant detriment to a cylinder's ability to radiate is its electrical length, though a clear drop in radiative ability is also visible as a cylinder's radius increases relative to its length. Note that for electrical lengths less than about 0.35λ, the cylinder has vanishingly small total efficiency, irrespective of radius (within the realm of large-radius dipoles). If tightly-coupled arrays are to address these issues, any such improvements will be visible in the arrays' total efficiencies.

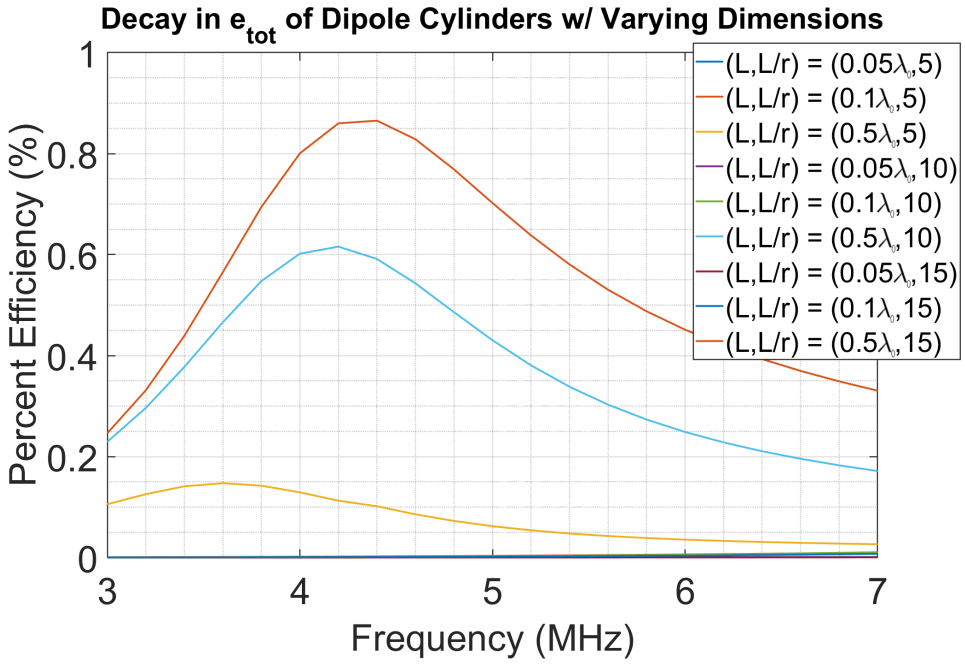

Figure 5.6: Degradation in Total Efficiency of a Single Cylindrical Antenna (5 MHz center). Note that 6 of the traces have vanishingly small total efficiency over the entire band of interest.

As a brief final remark for this section, realized gain measurements will also be of immense importance in the coming array analyses, as it will be important obviously to know not only an array's ability to radiate, but also the radiation pattern that is subsequently yielded. Fig. 5.7, for example, displays the azimuthal patterns for the same configurations used in fig. 5.6.

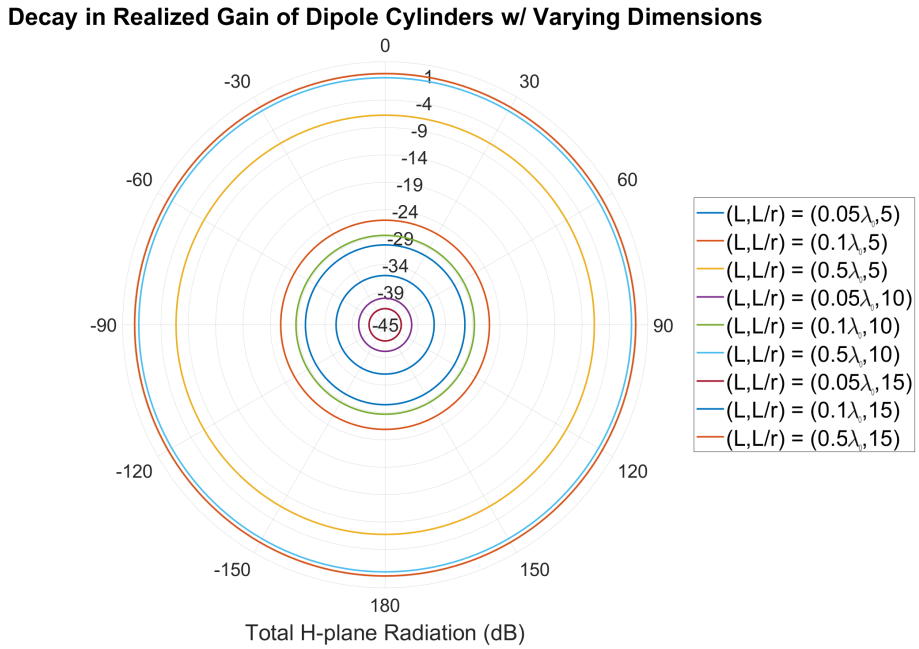

Figure 5.7: Degradation in Realized Gain of a Single Cylindrical Antenna (5 MHz). Note that the inner 6 traces have extremely low realized gain.

5.3 Array Factor-based Analysis

In this final section of chapter 5, the dipole array configurations to be used will be introduced, and some final baseline measurements of the single, cylindrical radiator will be established. In particular, as inter-element coupling will not be discussed until chapter 6, the array analyses presented here in this section will be based purely on the concept of array factors, a notion heavily employed in phased-array theory, for example. The radiation pattern of the single cylinder introduced in section 5.2 will be replicated for each of the 5-elements such that far-field interference patterns may be developed. Consequently, no inter-element coupling is allowed in this section's analysis. While this baseline is somewhat artificial in nature, as the array patterns shown will technically be non-physical given the close proximity of the elements, it nonetheless serves as an

interesting baseline against which to compare the performance of later arrays. In other words, given some cylinder dimensions, and some array configuration, can the array that makes proper use of tight-coupling outperform even the "best possible" mutual impedance-free array? As will be discussed in future chapters, the answer, in some cases, is yes.

To begin, the three 5-element array configurations used in this thesis are displayed in fig. 5.8-5.10. In particular, the three were chosen such that different combinations of inductive coupling could be studied (as will be discussed in the next chapter, the capacitive, series coupling mechanism mentioned previously will turn out to be minimally useful). These configurations specifically include a classic broadside array, as well as a cornered array configuration and a crossed one, two additional formations in which a small swarm of UAS could plausibly fly. As will be seen shortly, each formation will have its own characteristic radiation patterns, which may or may not be useful, depending heavily on the desired application.

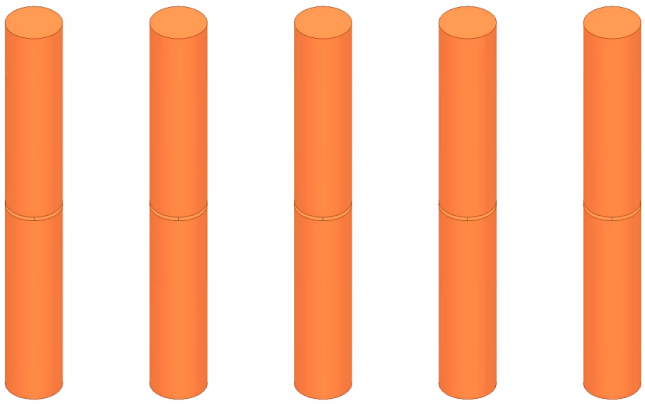

Figure 5.8: 5-element Broadside Cylinder Array Configuration

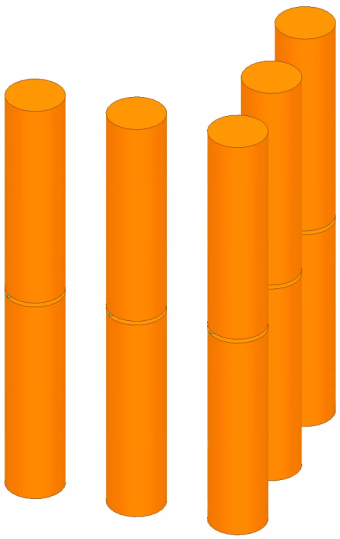

Figure 5.9: 5-element Cornered Cylinder Array Configuration

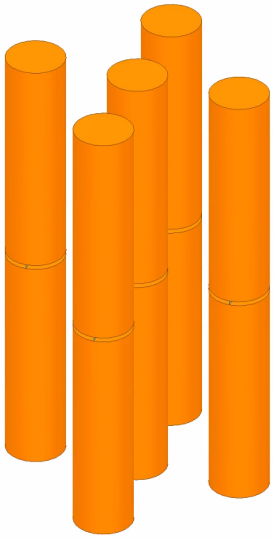

Figure 5.10: 5-element Crossed Cylinder Array Configuration

Beginning with the largest dimensions and the broadside formation, the realized gain patterns of several half-wavelength dipole arrays with varying inter-element separations are visible in fig. 5.11-5.13. The most noteworthy outcomes amount to the

following. Firstly, it's worth noticing the general shape of the gain patterns in each of these figures; the broadside array, classically, has two opposite beams that become more focused with increased separation, albeit with increased side-lobe levels (SLL) as well. It is a common focus of phased array theory to minimize such SLL, while maximizing the gain of the main beam, as well the maximum scan angle achievable by the array. Here, however, it is sufficiently useful to note this trend in gain pattern behavior. Secondly, it will be one of the goals of this project to have each tightly-coupled array, presented in chapters 7 and 8, surpass the maximum gain value of its respective coupling-free counterpart, presented in this section. For this particular setup, the maximum gain achieved is around 9 dB.

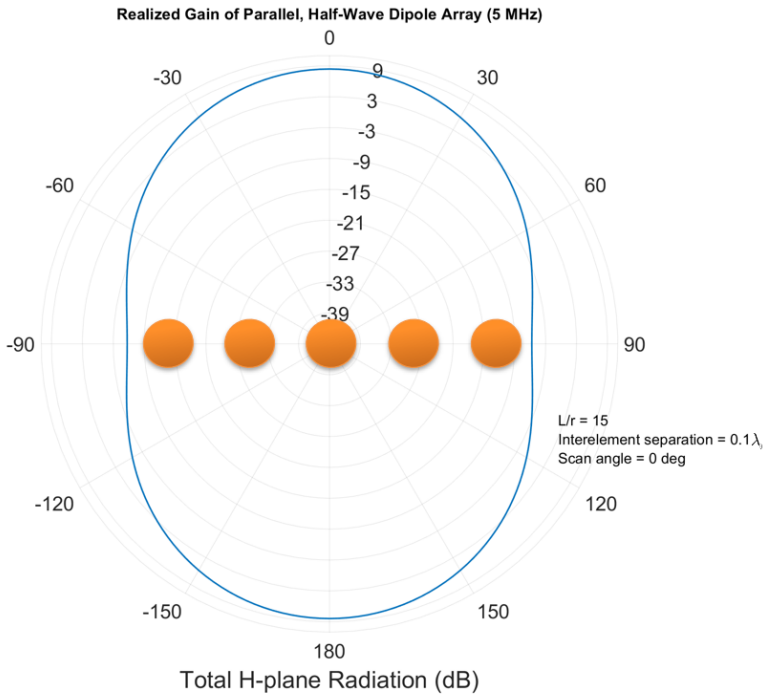

Figure 5.11: 5-element Broadside Cylinder Array Configuration w/ no side lobes

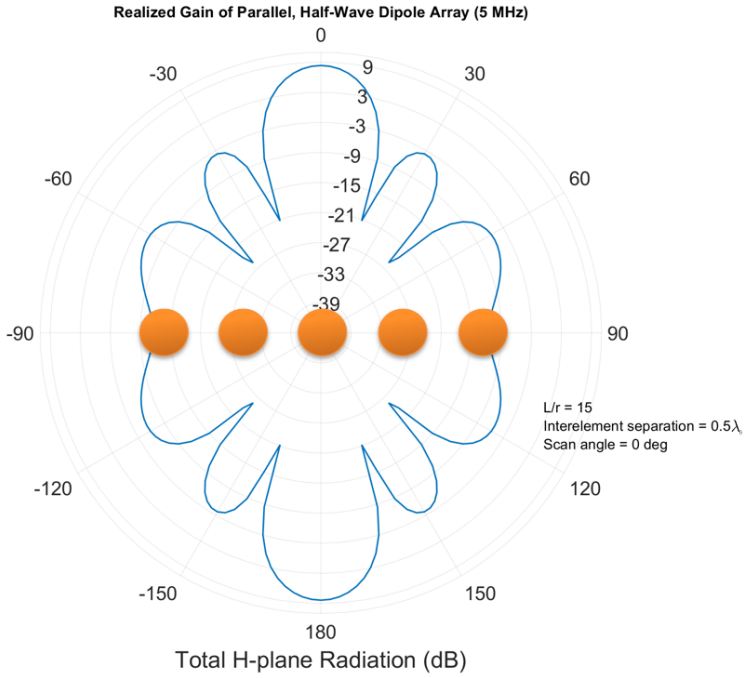

Figure 5.12: 5-element Broadside Cylinder Array Configuration w/ mild side lobes

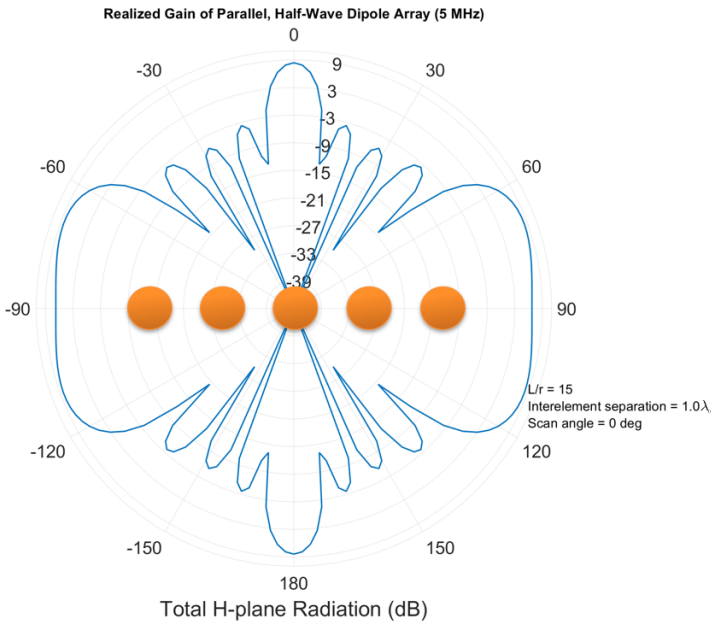

Figure 5.13: 5-element Broadside Cylinder Array Configuration w/ drastic side lobes

In fig. 5.14-5.16, the same broadside array's realized gain patterns are visible, with the physical dimensions of the broadside array shrinking with each step. In particular, it can be seen, when comparing these figures to fig. 5.11-5.13, how the maximal gain is dependent entirely on the physical dimensions of the individual radiators, rather than the inter-element separation itself. Likewise, the precise pattern shape is primarily dependent on the element spacing, as opposed to other factors; the SLL however, can be somewhat affected by reduced element size, as seen in fig. 5.18. Additionally, once again, it can be noted how reductions in electrical length lead to more drastic drops in performance than similar changes in radius.

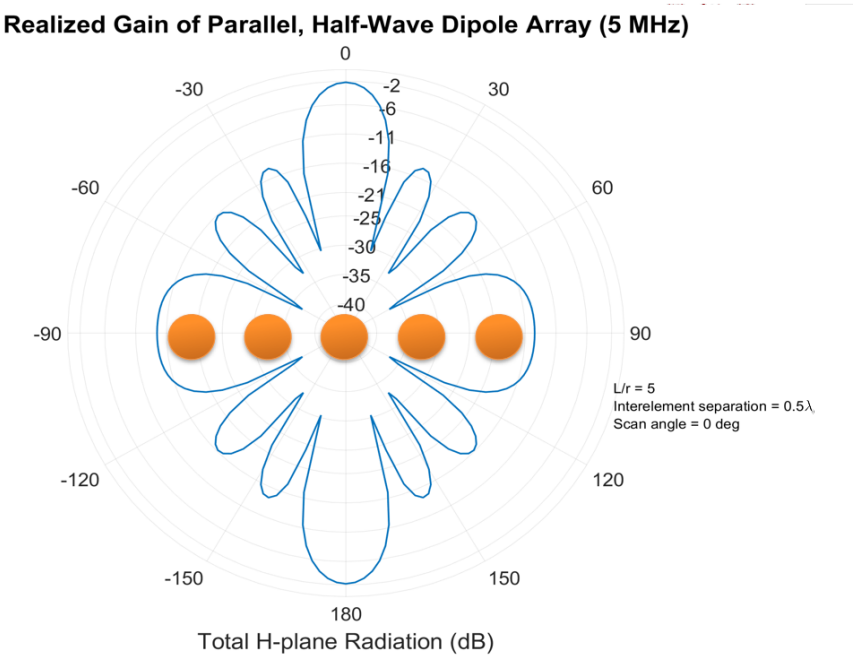

Figure 5.14: 5-element Broadside Cylinder Array Configuration w/ mild side lobes

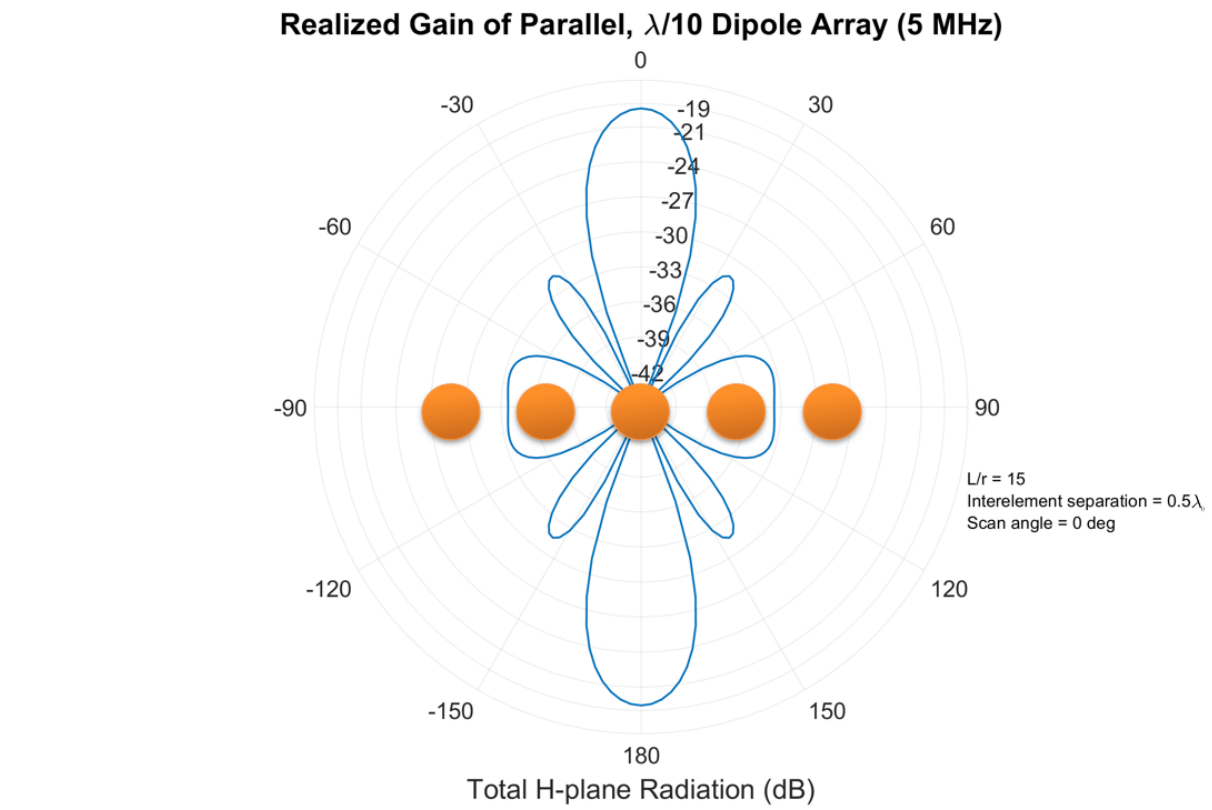

Figure 5.15: 5-element Broadside Cylinder Array Configuration w/ mild side lobes

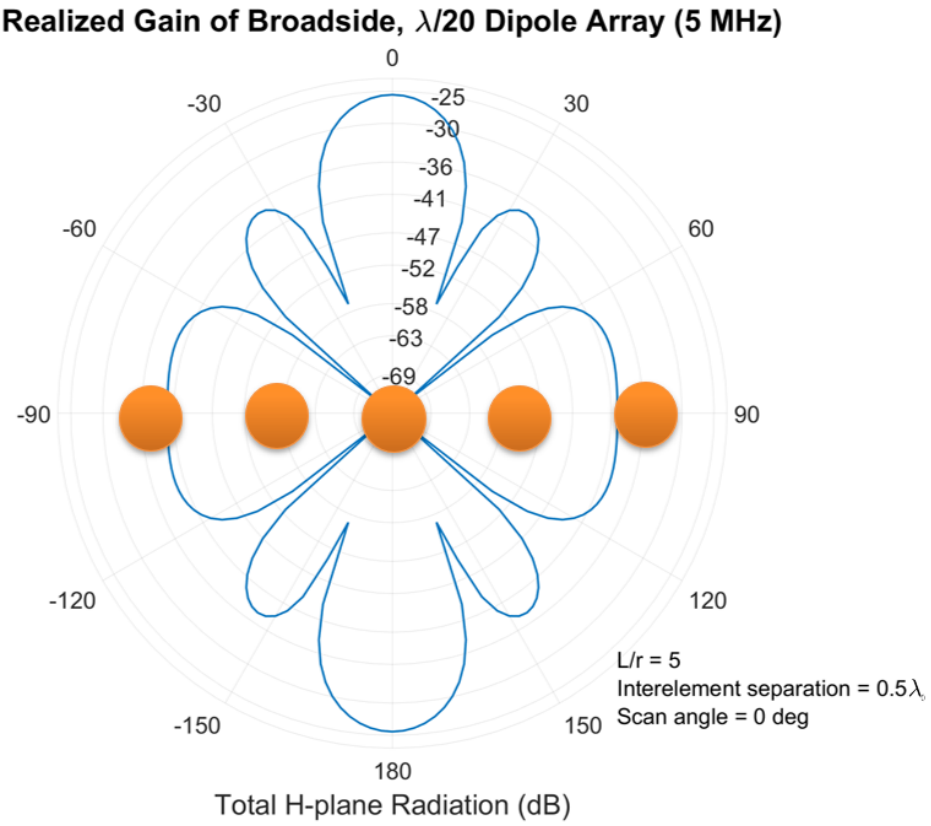

Figure 5.16: 5-element Broadside Cylinder Array Configuration w/ mild side lobes and a moderate-width ”beam”

Finally, as can be seen in fig. 5.17-5.18, while a change in the configuration of the cylinder array does result in a change in the pattern, neither the maximal realized gain, nor the SLL, is especially affected. In fact, this trend continues for the rest of the possible dimensions for both the cornered and crossed arrays. As such, further analysis here of the cornered and crossed arrays is not needed, the baseline having been well established by the broadside parallel array. The pattern for the crossed array will consequently be introduced in chapter 7.

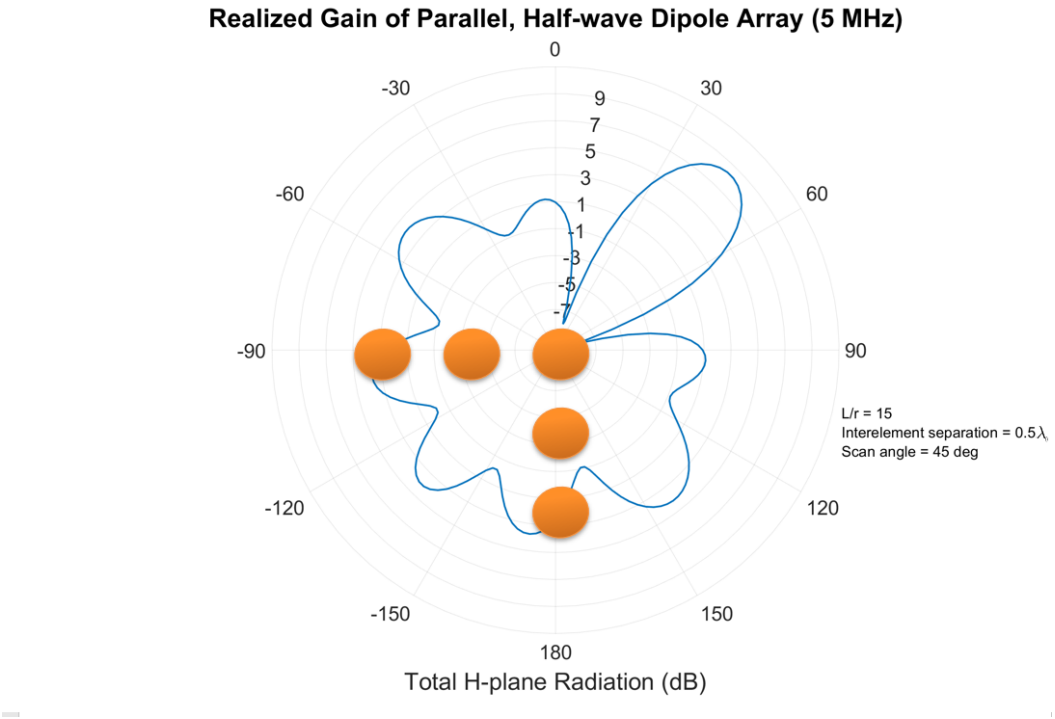

Figure 5.17: 5-element Cornered Cylinder Array Configuration w/ significant side lobes

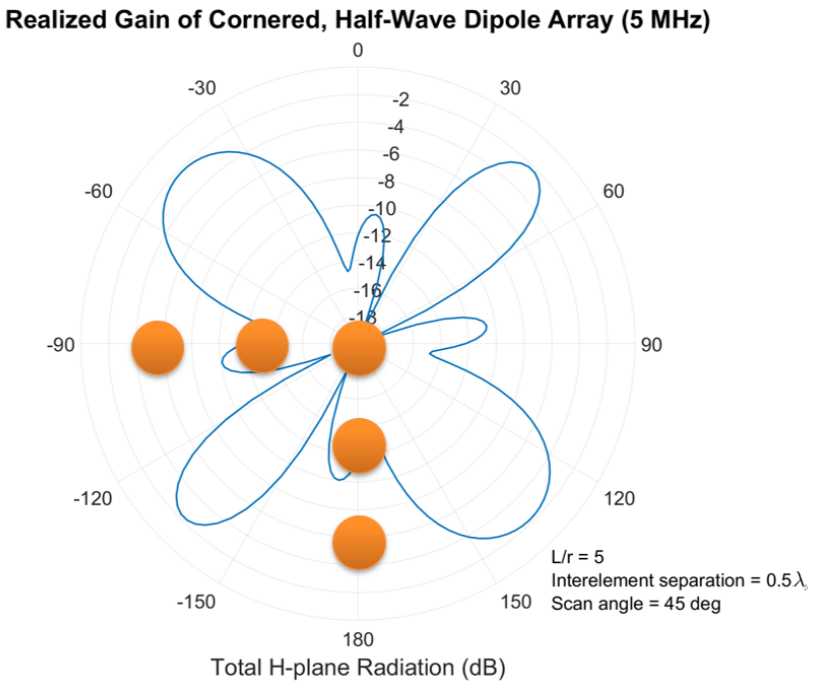

Figure 5.18: 5-element Cornered Cylinder Array Configuration w/ extreme side lobes

Chapter 6

Coupling Mechanisms Revisited

6.1 Mutual Impedance Calculations

As was discussed in chapter 2, one of the central preliminary analyses needed in the exploration of the feasibility of tightly-coupled airborne arrays is on the ability of two elements to couple, using only mechanisms available to such arrays. In the context of this thesis, those two mechanisms are once again, serial plate coupling between the end caps of cylindrical elements, and longitudinal, parallel coupling between the lengths of two elements. In particular, this "coupling ability" will be assessed in two ways: firstly, by measuring the coupling strength in terms of mutual impedance, and secondly, by measuring the usefulness of said coupling in terms of total efficiency improvement, or at least deviation. Beginning with the longitudinal mechanism, it can be seen in fig. 6.1, how, for a wide variety of inter-element separations, the coupling strength between two parallel, half-wave dipoles (represented by the real part of the Z-parameter, Z_{21}) varies significantly in both its strength and the frequency location of its extrema. This behavior is rather auspicious, as it demonstrates the ability of just two elements to couple fairly strongly, the mutual resistance being often on the same order as, if not much stronger than, the self-resistance of the singular cylinders, described in chapter 5. Additionally, the moderate variation in location of the extrema is also particularly

useful, as it suggests potential for later arrays to possess some degree of frequency reconfigurability.

At this point, however, a few major limitations should be noted. Specifically, it can be seen that for the data displayed in fig. 6.1, the inter-element separations with the strongest coupling are of course those with the closest spacing; in fact, this spacing becomes quite infeasible at the smallest separations, especially for separate aircraft where significant inter-craft spacing is typically imperative. Additionally, this strong coupling displayed thus far is of course limited exclusively to the largest length cylinders, at a half-wavelength. Subsequent similar observations can be made with respect to the data displayed in fig. 6.2; here, the mutual reactance between the same two cylinders is shown. Once again, variation in impedance strength and extrema location should be noted.

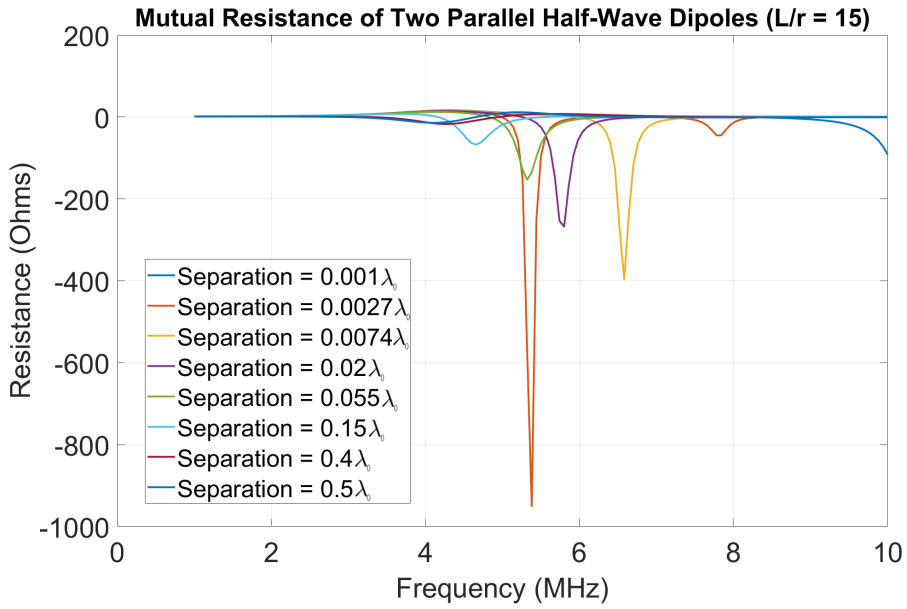

Figure 6.1: Variation in the strength and extrema location of the mutual resistance between two half-wavelength cylinders $(L/r = 15)$. Notice how the strength in coupling generally decreases as the inter-element separation is increased.

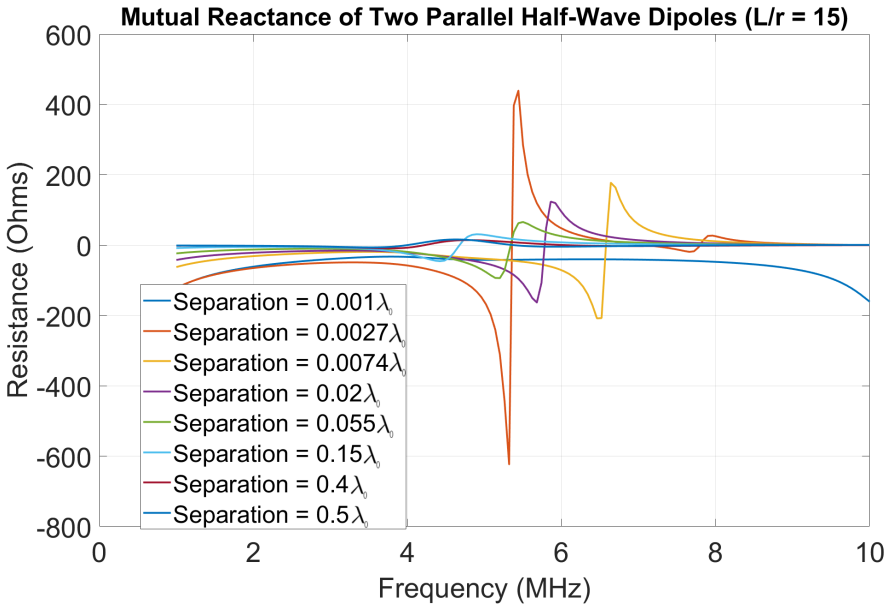

Figure 6.2: Variation in the strength and extrema location of the mutual reactance between two half-wavelength cylinders $(L/r = 15)$. Notice how the resonant location cycles around the band as the inter-element separation is increased.

In the next two data sets, fig. 6.3-6.4, very similar measurements are represented, save for a single change in the cylinder radii, namely the decrease from a length-to-radius of 15, to one of 5. In doing so, fig. 6.3-6.4 demonstrate how larger radii weaken the ability of two cylinders in parallel to couple effectively. In particular, two observations should be made, the first being the notable decrease in the magnitude of the extrema of both the mutual resistance and mutual reactance between the two cylinders, across all variations. This decrease, of course, indicates a weaker ability for currents on one cylinder to influence the open-circuit voltage at the port of the other cylinder, per equation (2.12), meaning the role of tight-coupling as a technique is correspondingly reduced. The second change worth noting is the reduced number of distinct inter-element separations corresponding to significant coupling strengths. This in turn, of course, indicates both a reduced ability for frequency tuning to exist between two cylinders,

as well as a decrease in the feasibility of application to airborne systems, as only the more infeasible separations remain significant. Nonetheless, this does not yet indicate (and will turn out to not indicate at all) that tight-coupling is not applicable to larger radii-cases; rather, it merely demonstrates how SUAS incorporating wider cylindrical forms will likely require somewhat greater numbers of swarm elements in order to compensate appropriately.

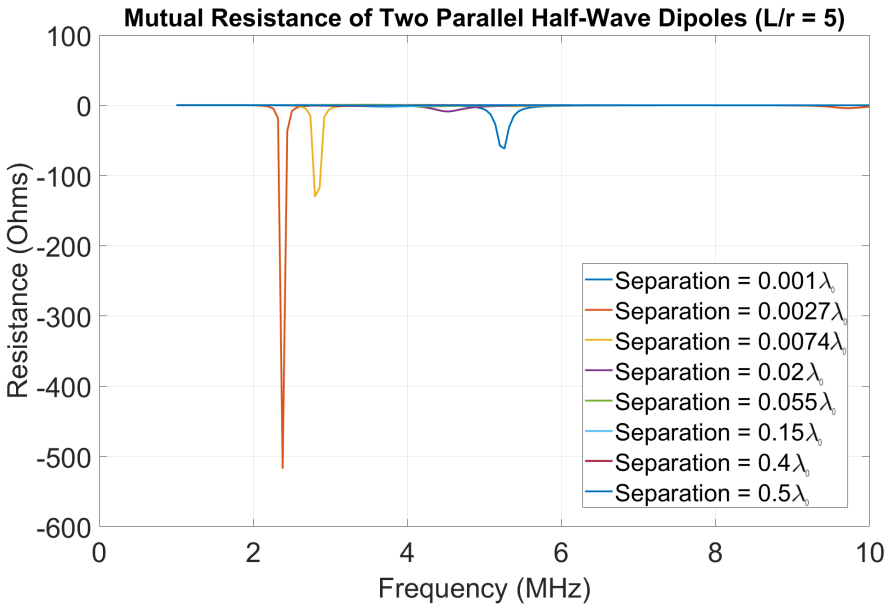

Figure 6.3: Variation in the strength and extrema location of the mutual resistance between two half-wavelength cylinders $(L/r = 5)$. Notice how the strength in coupling is everywhere weakened relative to the $(L/r = 15)$ case.

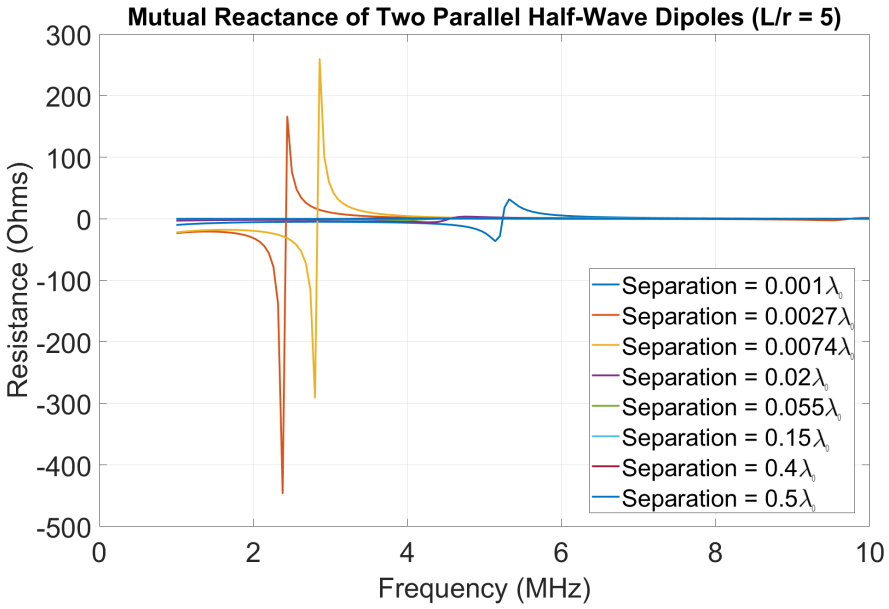

Figure 6.4: Variation in the strength and extrema location of the mutual resistance between two half-wavelength cylinders $(L/r = 5)$. Notice how fewer distinct resonant locations are present relative to the $(L/r = 15)$ case.

Now, in the previous four figures, all of the measurements were restricted to half-wavelength (at 5 MHz) cylinders, demonstrating the capabilities of the parallel coupling mechanism without electrical size constraints. In fig. 6.5-6.8, however, the mutual impedance for very electrically small, specifically $\lambda/10$, cases is considered. In these cases, however, unlike those of fig. 6.3-6.4 where the only constraint involved increased radii, the additional constraint of diminished electrical size has an incredibly detrimental effect on the coupling strength of the two cylinders in question. Particularly, for fig. 6.5 and 6.7, the displayed mutual resistance, for both the $(L/r = 15)$ and $(L/r = 5)$ cases, displays nearly trivial magnitudes, ranging from a couple of ohms, down all the way to a few hundredths of an ohm, even for infeasibly close inter-element separations. As such, unlike in the preceding paragraph where sufficient compensation via additional elements may be reasonably expected, it is unlikely that mutual resistance of this

magnitude will allow for the use of tight-coupling at such small electrical dimensions. Consequently, for the parallel coupling mechanism, it can be reasonably assumed that the boundary separating the applicability and inapplicability of tight-coupling corresponds to an electrical length somewhere between $\lambda/2$ and $\lambda/10$ (it will turn out to be at around 0.35λ in the $L/r = 15$ case). Additionally, in fig. 6.6 and especially in fig. 6.8, it is once more clear how the reduction in electrical length has also caused drastic degradation in the magnitude of inter-cylinder mutual reactance. While these decrements are not necessarily comparable to those corresponding to mutual resistance, they also do little to compensate for the minute self-resistance typical of cylinders at such small electrical lengths.

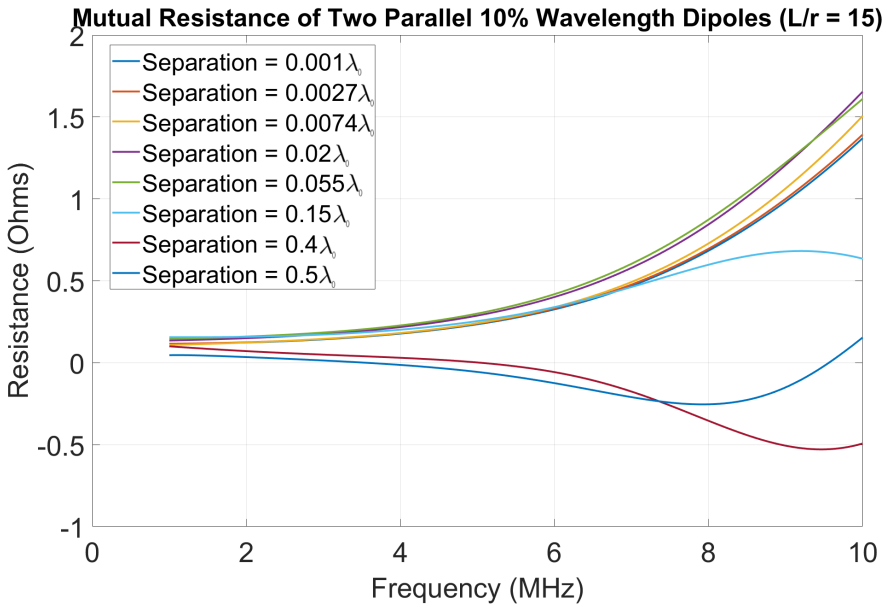

Figure 6.5: Variation in the strength and extrema location of the mutual resistance between two $\lambda/10$ cylinders $(L/r = 15)$. Notice how the strength in coupling is minimal.

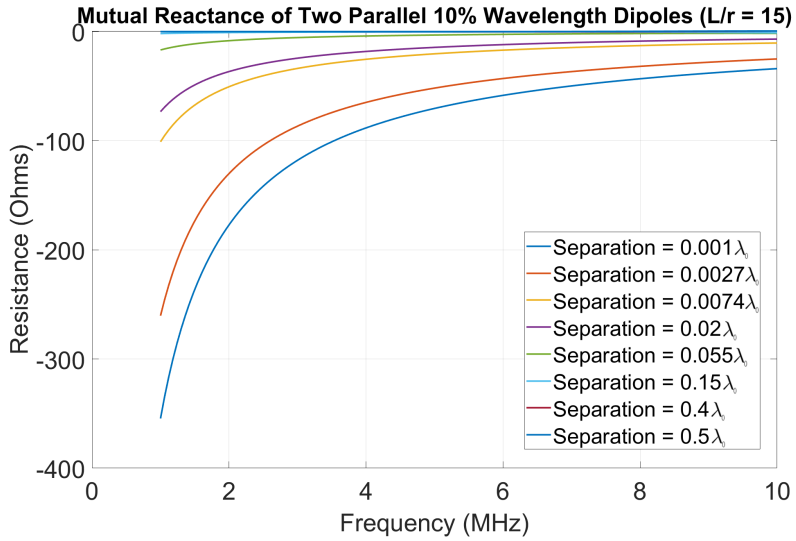

Figure 6.6: Variation in the strength and extrema location of the mutual reactance between two $\lambda/10$ cylinders $(L/r = 15)$. Notice how the strength in coupling is minimal.

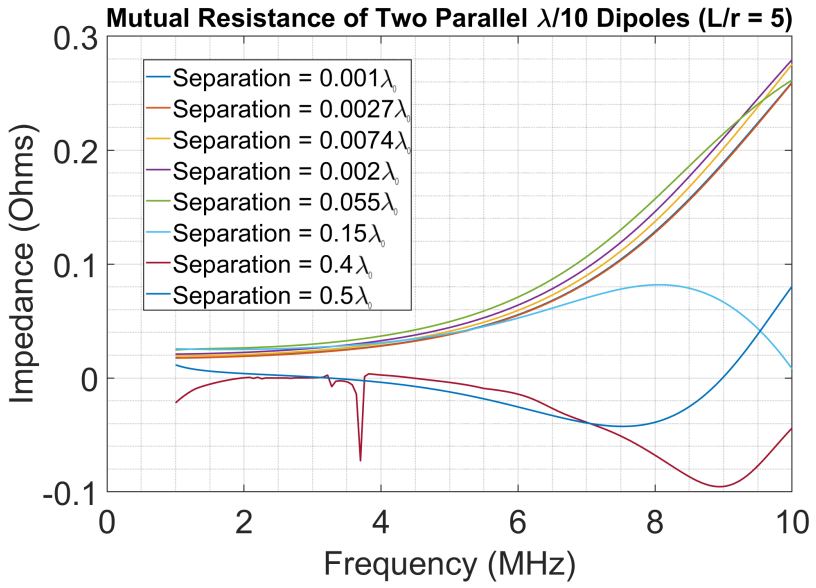

Figure 6.7: Variation in the strength and extrema location of the mutual resistance between two $\lambda/10$ cylinders $(L/r = 5)$. Notice how the strength in coupling is minimal.

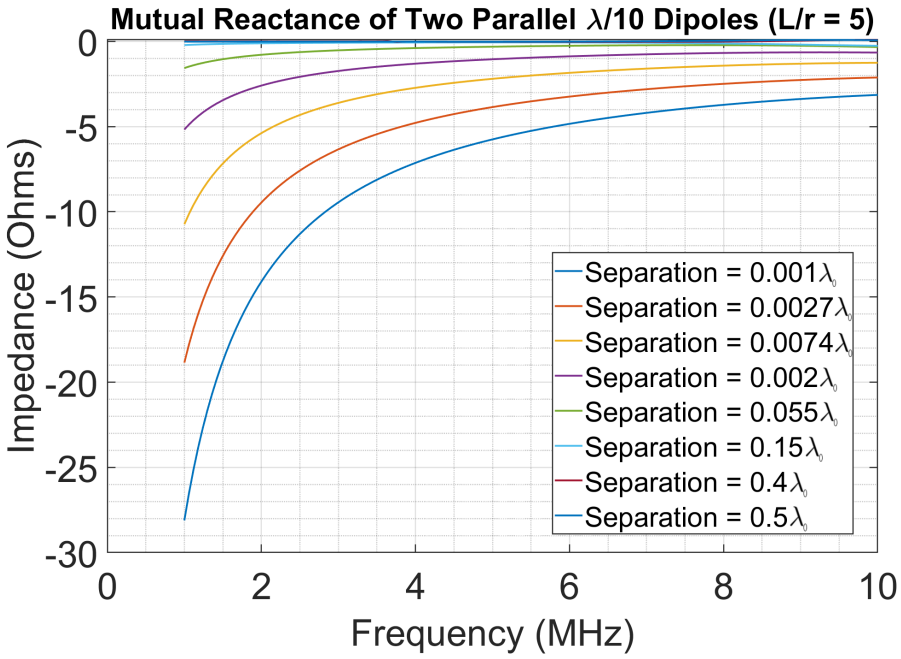

Figure 6.8: Variation in the strength and extrema location of the mutual reactance between two $\lambda/10$ cylinders $(L/r = 5)$. Notice how the strength in coupling is minimal.

The other coupling mechanism explored in this thesis, as previously mentioned, is the serial plate coupling between coaxially aligned cylinders. Similar to that of fig. 6.1-6.2, the data displayed in fig. 6.9-6.10 corresponds to the half-wavelength, smaller radii case, wherein the inter-element coupling is strongest. However, by directly comparing the two mechanisms themselves in terms of mutual resistance and reactance, it is also clear that the serial mechanism falls short of its parallel counterpart by roughly a factor of 10, making it the weaker mechanism by far. That being said, the serial mechanism does, nonetheless, have one interesting characteristic relative to the previous mechanism; specifically, for two cylinders designed to be a half-wavelength each at 5 MHz, the spectral location of the extrema displayed in fig. 6.9-6.10 is somewhat low, especially in comparison to their parallel coupling counterparts. Were the magnitudes of these extrema moderately greater, this plate coupling mechanism as a whole may have

even proved to be of some significant value.

However, for a few reasons, this coupling mechanism will not, moving forward, be used in the design of tightly-coupled apertures in this thesis. The first of these reasons is of course visible in this section alone; specifically, the order of magnitude of the mutual impedance observed between two serial cylinders is quite weak relative to the parallel mechanism. Consequently, as will be seen in the next section, this factor will act as a significant setback for the serial mechanism, in terms of improving the total efficiency of the total radiating aperture, relative to the singular cylinder discussed in chapter 5. Secondly, while both inter-element coupling mechanisms available to UAV bodies have been hereto explored, it is worth noting that the second of these mechanisms presents some difficulty in physical realizability. To be precise, it is obvious that any functioning, fixed-wing aircraft will not possess flat ends on its fuselage, but rather some degree of curvature or tapering. Electromagnetically, this distinction is critical as it vastly reduces the ability for any form of serial coupling to occur. In particular, while this serial coupling was previously described as being heavily capacitive, it is clear from fig. 6.10 that this coupling has some significant degree of inductivity involved as well, given the positive reactance present for parts of the observed band. Thus, as the currents hosted on these end caps will naturally be less able to couple under non-parallel conditions, the inductive portion of the mechanism will be considerably weakened. Additionally, as is described in [60] and [61], it is the presence of these end caps, specifically their edges perpendicular to the cylinder's length, that allows for the accumulation of charges, without which the serial mechanism becomes less capacitive. Rephrased, this means that as the well-defined end cap is deformed towards a more rounded, even semi-spherical shape, thus being more representative of a true fuselage, the existence of serial, inter-cylinder coupling is minimized. Furthermore, it is easily imagined how coaxial alignment, unlike longitudinal alignment, may present an espe-

cially difficult control problem, even without consideration of weather-related factors. In summary, a number of physical issues specific to the serial-coupling mechanism exist, and as such, only the parallel mechanism will be considered, starting with the next chapter.

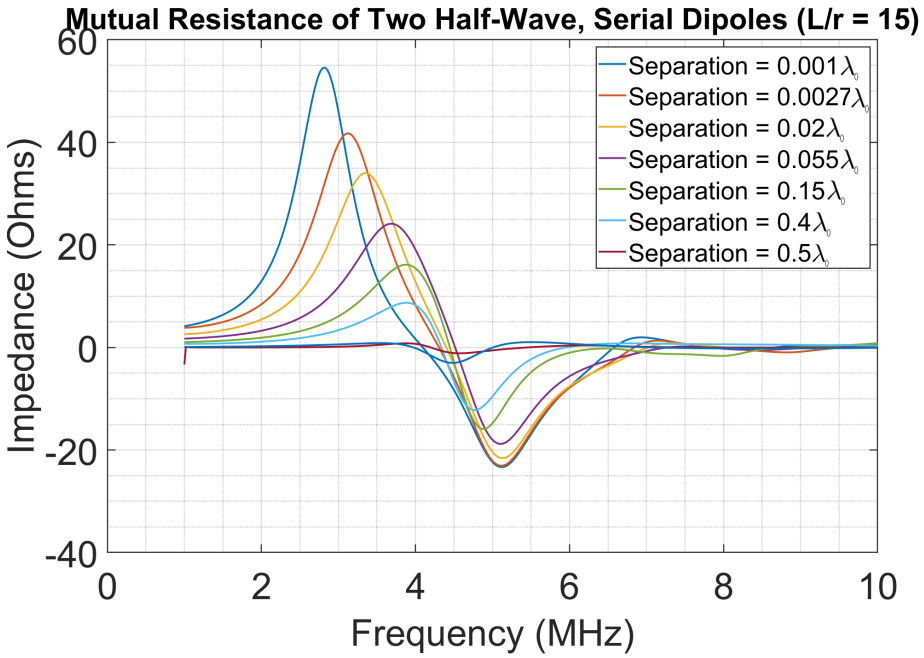

Figure 6.9: Variation in the strength and extrema location of the mutual resistance between two half-wavelength cylinders $(L/r = 15)$. Notice how the strength in coupling is low relative to that in fig. 6.1, and also somewhat lower in frequency.

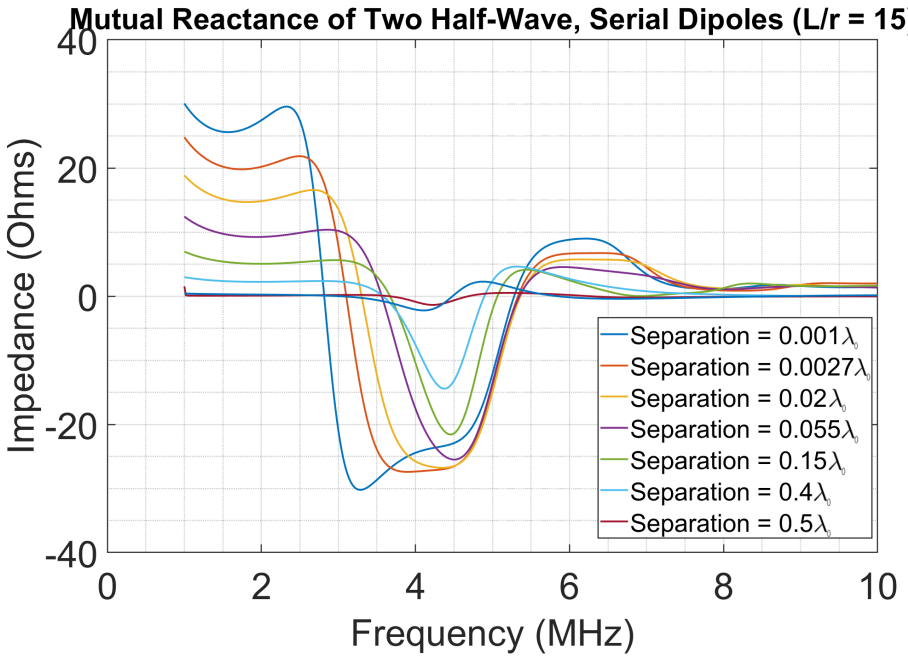

Figure 6.10: Variation in the strength and extrema location of the mutual reactance between two half-wavelength cylinders ($L/r = 15$). Notice how the strength in coupling is low relative to that in fig. 6.1, and also somewhat lower in frequency.

Reinforcing the previous discussion, when the larger radii case of the serial coupling mechanism is observed in fig. 6.11-6.12, very little -inter-element interaction is visible, a drop in performance even worse than that experienced by the parallel mechanism. In fact, the coupling present in this case is comparable to the $\lambda/10$ case discussed for fig. 6.5-6.8, meaning that this coupling mechanism is likely to be of little use, even at larger electrical lengths. Therefore, the possible applicability of this second mechanism is clearly narrower, meaning it will not likely be useful for a large number of the project goals presented in this thesis. If there is one interesting characteristic of this $L/r = 5$ case, nonetheless, it is in the fact that its most significant extrema occurred for moderate separations, as opposed to the numerous cases wherein coupling strength was strongly inversely proportional to element separation.

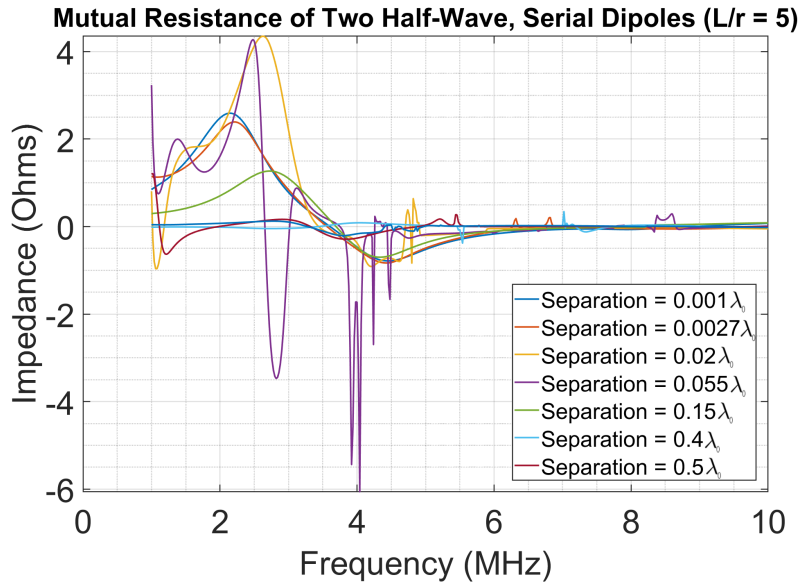

Figure 6.11: Variation in the strength and extrema location of the mutual resistance between two half-wavelength cylinders $(L/r = 5)$.

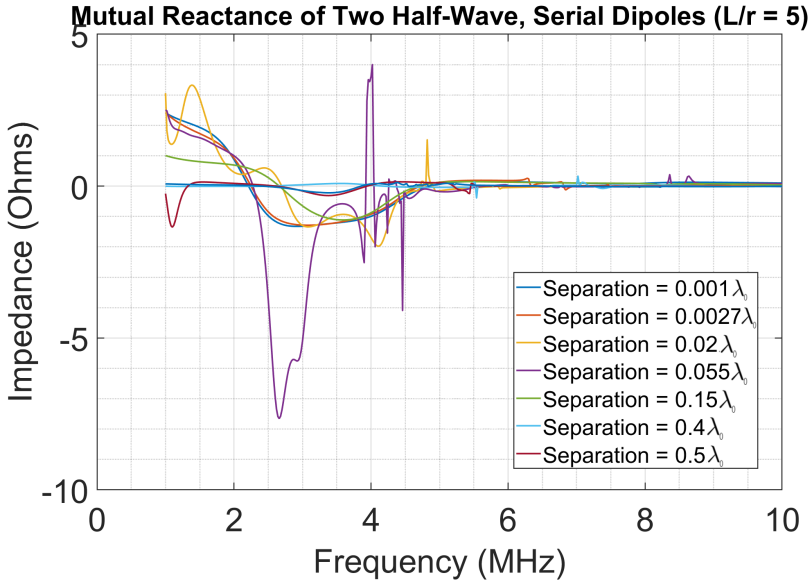

Figure 6.12: Variation in the strength and extrema location of the mutual reactance between two half-wavelength cylinders $(L/r = 5)$.

6.2 Total Efficiency Calculations

In this section, the two coupling mechanisms are briefly analyzed once more, this time in terms of their radiative performance, the utilized metric now being total efficiency. In fig. 6.13 the total efficiency of the two-cylinder aperture is displayed, with the dashed line indicating the total efficiency of the singular cylinder first discussed in chapter 5. Several important aspects here should be noted. Firstly, relative to the single cylinder case, mild improvements in the maximum total efficiency are clear for several distinct inter-element separations, improving the efficiency from around 85% to upwards of 90%. While this improvement may not necessarily be drastic, the fact that it is visible at all for the two cylinder case is auspicious for larger element apertures, as it can be expected that as the number of elements in the array increase, the total efficiency will, in the best case, approach 100% asymptotically. Secondly, while not all of the different separation values have extrema exceeding the base case, a number of very non-trivial extrema exist nonetheless, suggesting that in larger arrays, some amount of frequency tuning may be possible, as each separation obviously corresponds to a different physical reconfiguration of the dipole array. Moreover, the ability of active arrays (here meaning non-parasitic, not non-passive) to utilize phase control will be particularly useful to this end. Thus, by merely shifting the relative positions of the elements within the aperture, the operational band's center and extents may possibly be shiftable. Alternatively, this result may be interpreted as yielding a small degree of positional tolerance; specifically, this means that even in poorly controlled arrays where significant instability in the relative positioning of the elements is present, some usable operational frequency may still exist.

Finally, it should be noted that, despite the results of the previous section, the most significant extrema here in fig. 6.13 correspond to the largest separation values, with

even moderately useful traces extending all the way down to 0.02λ, as displayed in the green trace. This is, of course, a very worthwhile point as it grants greater likelihood to the realizability of a full, tightly-coupled SUAS.

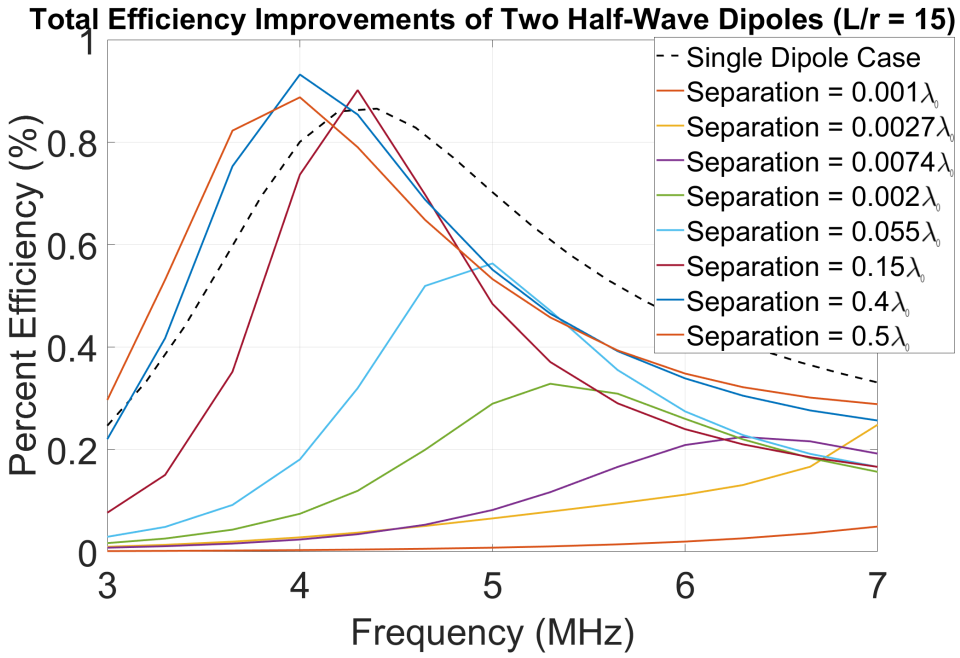

Figure 6.13: Variation in the total efficiency of the parallel coupling mechanism for various inter-element separation lengths. $(L/r = 15)$ case.

In fig. 6.14, even more meaningful results can be seen, where the focus is now on the coupling performance for two $(L/r = 5)$ cylinders. While the traces in fig. 6.14 do of course have somewhat diminished extrema compared to those in fig. 6.13, those same peaks relative to the single dipole, $(L/r = 5)$ base case are an excellent improvement. In fact, many of the previously discussed points regarding the $(L/r = 15)$ case are present again here; in particular, much greater frequency separation in the extrema can be observed, thus reinforcing the notion of a frequency reconfigurable system. If this case does have a drawback, however, it can be seen in the particular traces having the greatest extrema. Specifically, the separation values providing the greatest improve-

ment in total efficiency are among the smaller and more moderate cases, the largest ones now having little to offer.

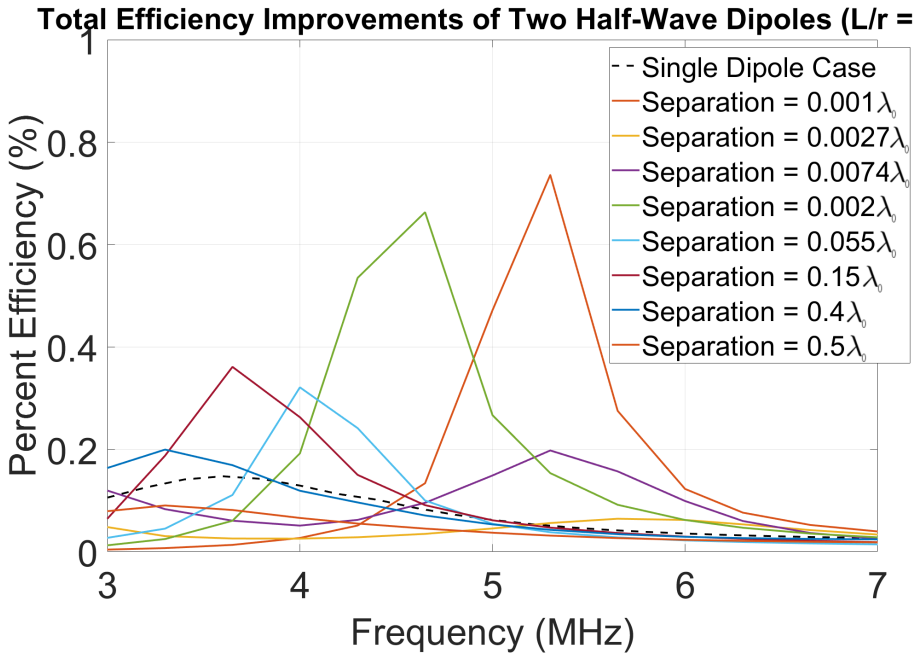

Figure 6.14: Variation in the total efficiency of the parallel coupling mechanism for various inter-element separation lengths. $(L/r = 5)$ case.

In fig. 6.15-6.16, two similar cases are displayed, now focusing on the serial coupling mechanism. While, like the parallel coupling case, some change in the shape of the frequency response is clearly visible here, it is also clear that these changes are less significant than in the previous pair of cases. This speaks to this mechanism's decreased ability to affect each cylinder's performance away from that of the singular case. This is especially accurate for the $(L/r = 5)$ case, where only minimal deviation at all is observable. Deviation aside, however, the other aspects mentioned for the previous mechanism are readily observed for this one as well.

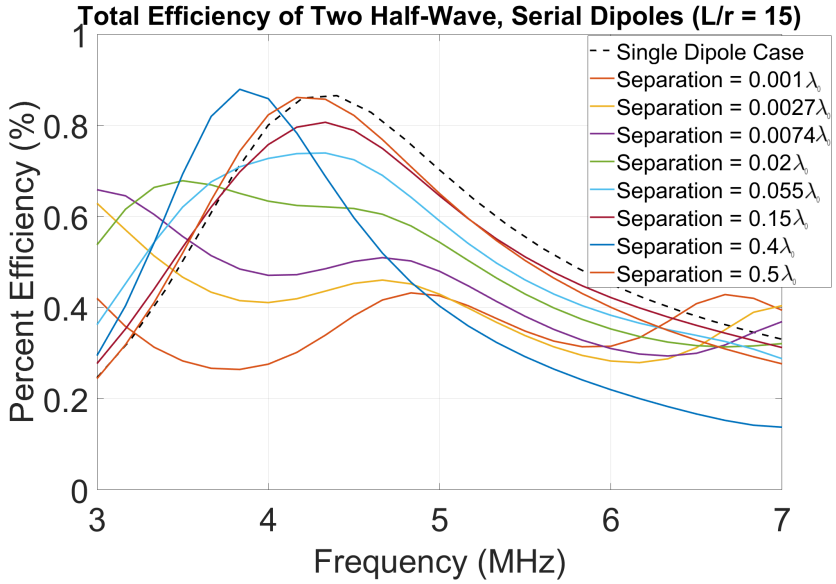

Figure 6.15: Variation in the total efficiency of the serial coupling mechanism for various inter-element separation lengths. $(L/r = 15)$ case.

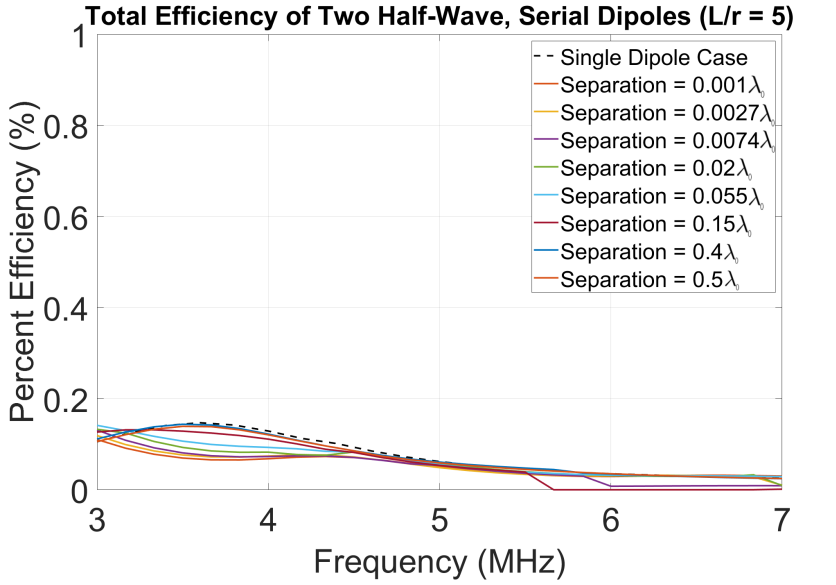

Figure 6.16: Variation in the total efficiency of the serial coupling mechanism for various inter-element separation lengths. $(L/r = 5)$ case.

Chapter 7

Five-element Parasitic Dipole Arrays

In much the same way as was done in chapter 6, this chapter will serve as an analysis of the improvements that can be made to an antenna aperture's total efficiency. In this case, however, the main focus will be on apertures comprised of parasitic, 5-element arrays using the same array configurations as were introduced in chapter 5. For each of the array configurations discussed, the central element will be driven by a lumped excitation, in line with the theoretical voltage-gap of chapter 3, while the remaining cylinders will be purely parasitic, metalized bodies.

Beginning with the half-wave, $(L/r = 15)$ case, as is presented in fig. 7.1, the efficiency behavior of the broadside array, for a number of different separation values, is visible. While this particular figure doesn't offer *much* in the way of demonstrated improvement, it does still demonstrate one variation for which some improvement exists, namely for the plenty physically realizable inter-element separation of 0.5λ. For this particular variation, while the maximum value is not improved, but rather reduced, it does present some improvement in the bandwidth over which the array is measured, assuming the mild decline in efficiency is operationally tolerable, or can be partially alleviated through the use of matching networks, mismatch loss being a factor in total efficiency.

Another interesting, albeit not necessarily useful, characteristic found in the explo-

ration of these parasitic arrays is displayed in fig. 7.2. Namely, this figure shows how, for the single mentioned circumstance in fig. 7.1 (the blue trace with improved efficiency), the realized gain pattern (H-cut plane only) varies across the useful portion of the band (roughly 3.25 MHz - 5.25 MHz, moving from a more end-fire beam shape to a more traditional broadside beam shape. Additionally, the maximum realized gain for a number of these traces greatly exceeds that of the single dipole (displayed with a dashed line); these traces also perform reasonably well relative to the arrays mentioned in section 5.3, those idealized results being non-physical anyway. While the discussion thus far does suggest that this particular array may not necessarily be applicable to wide-band transception, it may be so for narrowband operations wherein both beam and frequency reconfiguration are needed.

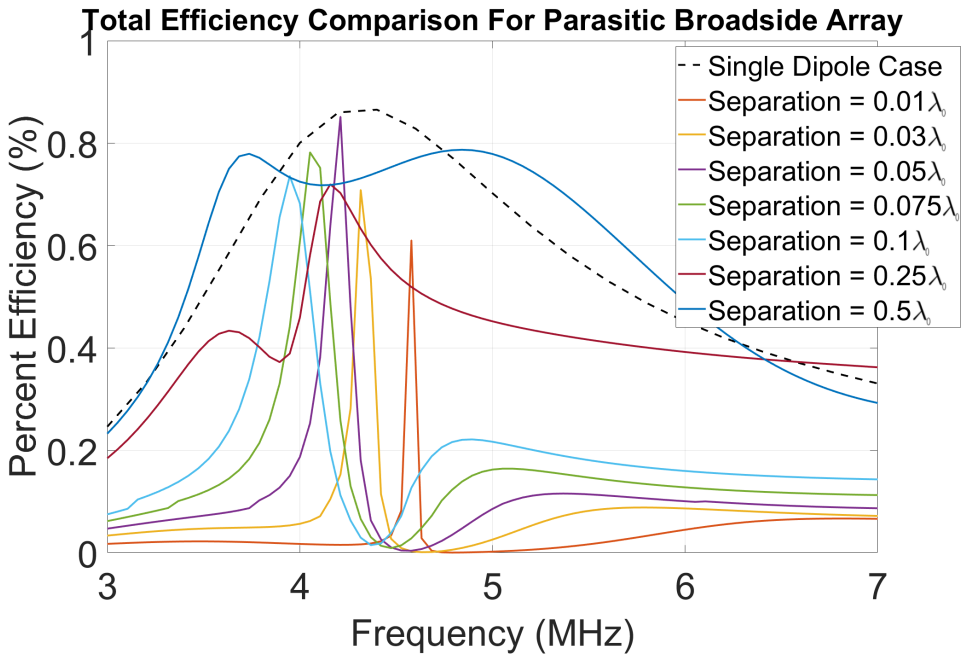

Figure 7.1: Variation across element separation in total aperture efficiency of a parasitic, broadside array ($L/r = 15$).

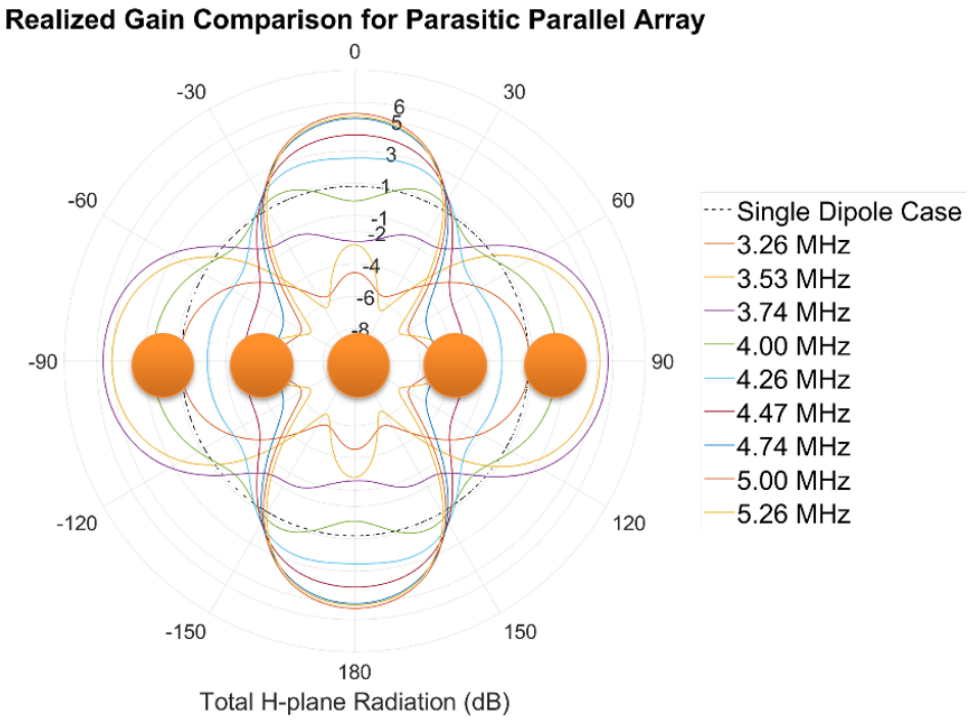

Figure 7.2: Variation across frequency in realized gain of a parasitic, broadside array ($L/r = 15$). Note that all traces here correspond to the single, dark blue trace in fig. 7.1

In moving to the $(L/r = 5)$ case (fig. 7.3), the magnitudes of these improvements are much improved, whether in an absolute sense with respect to their single dipole baseline, or in a relative sense with respect to the data of fig. 7.1; note that this trend very much parallels that found in section 6.2, and will, in fact, be a common one throughout the remaining chapters. Moreover, the data in fig. 7.3 demonstrates a moderate degree of frequency tuning; by merely shifting the relative separation of the aperture's elements, different operational bands become achievable, which may well be of application-specific use.

Another useful discussion worth raising here is in the concept of efficiency and bandwidth. Particularly, many common antenna metrics have similarly common, well-

established standards for what distinguishes a "good" radiator from a "bad" radiator or a "wide-band" system from a "narrow" one; for VSWR bandwidth, for example, a common standard distinguishes a narrowband antenna from a wideband one at a fractional bandwidth of 20%, and a wide band antenna from an ultra-wideband one at 50%, wherein VSWR is below some threshold, such as 1.5 or 2. Total efficiency, however, being an atypical metric, does not have such standards. In fact, even the more common metric of radiation efficiency tends to have only application-specific standards, as opposed to industry-wide ones. Consequently, for the sake of consistency, if total efficiency bandwidth is to be discussed in a precise manner in this thesis, it will be useful to define a cursory standard with which to operate. To this end, if the numbers provided in [62], for example, can be utilized, then a "good" antenna may be viewed as having a radiation efficiency of "$50 - 60\%$". Total efficiency of course, compared with radiation efficiency, factors in mismatch loss as well, meaning it provides a somewhat more conservative measurement of the amount of energy dispersed throughout a radiative system. Consequently, subsequent discussion of efficiency bandwidth will be relative to a total efficiency of 50%, the boundaries between narrowband and wideband systems being unchanged. In this way, the single, useful trace of fig. 7.1 may be viewed as having an approximately 50% fractional bandwidth, as opposed to the $2 - 3\%$ bandwidths of fig. 7.3.

In fig. 7.4, the traces displayed are once again realized gain, but, unlike those in fig. 7.2, each one of these traces corresponds to one of the worthwhile extrema from fig. 7.3. Of particular note here is how the several beams produced by these extrema are predominantly end-fire in shape. Additionally, it is easily observed that the maximum realized gain values achieved by this larger radii case are comparable to those of the smaller, $(L/r = 15)$ case; in fact, even relative to the goal of -2 dB set for half-wave, $(L/r = 5)$ apertures set in chapter 5 (fig. 5.14), the patterns presented demonstrate

a very successful improvement in the radiative ability of the array. Consequently, fig. 7.3 and 7.4 together suggest a system wherein frequency tuning by way of mechanical reconfiguration may indeed be quite realizable, albeit only with narrow bands, as a fair degree of beam stability is also present across extrema.

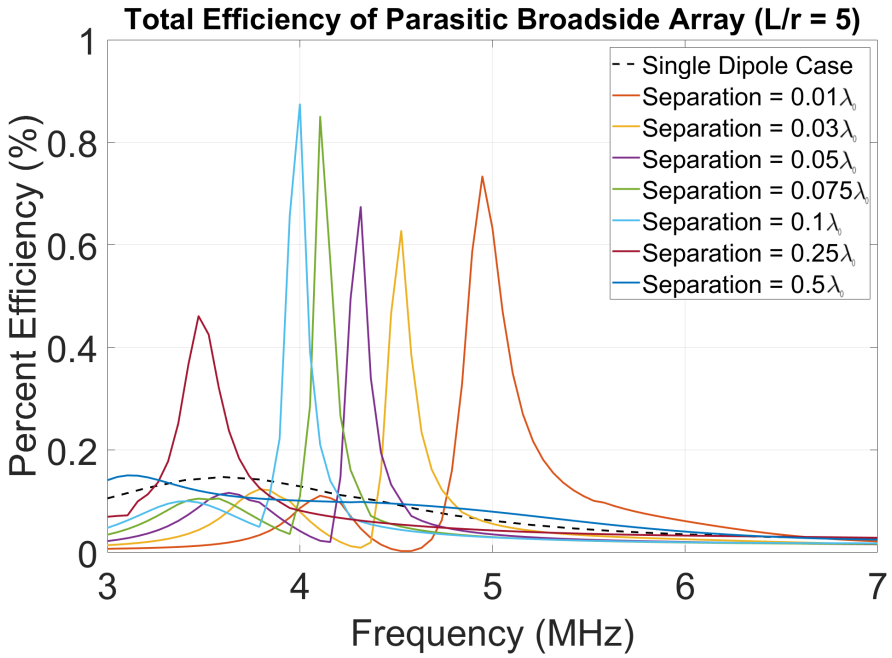

Figure 7.3: Variation across element separation in total aperture efficiency of a parasitic, broadside array ($L/r = 5$).

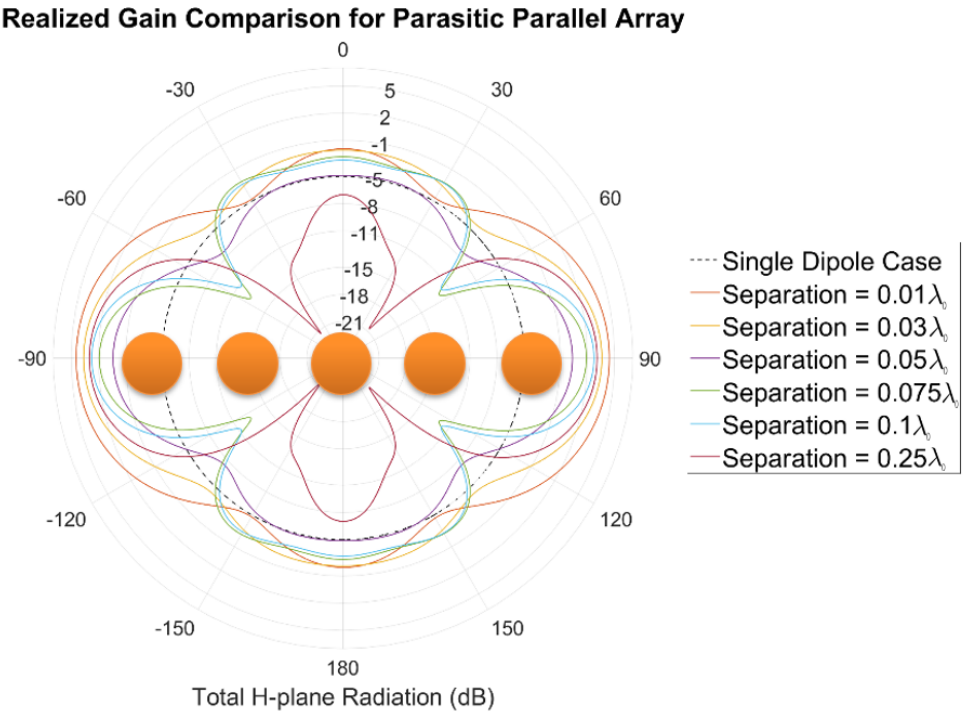

Figure 7.4: Variation across frequency in realized gain of a parasitic, broadside array ($L/r = 5$). Note that each trace here corresponds to a different trace's extremum in fig. 7.3.

As was discussed previously in this thesis, the threshold for dipole electrical length, beyond which the parallel coupling mechanism becomes only minimally useful, is at around 0.35λ, for the $(L/r = 15)$ case. As can be seen in fig. 7.5-7.6 with $\lambda/4$ length elements, this value holds, as the efficiency curves only become "significant', now roughly defined as $e_{tot} > 50\%$, at around 7 MHz. At this frequency, an antenna, corresponding to $\lambda/4$ at 5 MHz, has an electrical length of almost exactly 0.35λ at 7 MHz. In the case of fig. 7.6, this threshold is obviously pushed closer to the $\lambda/2$ mark. While both of these figures do demonstrate efficiency improvements relative to their base cases ($e_{tot} \ll 1\%$), these improvements are nonetheless of little use.

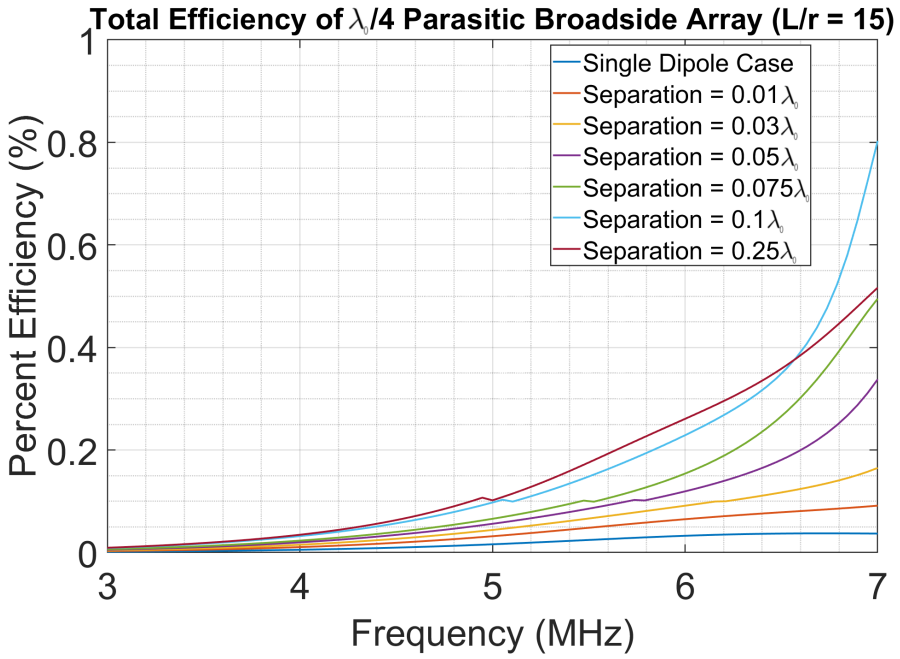

Figure 7.5: Variation across element separation in total aperture efficiency of a $\lambda/4$, parasitic, broadside array ($L/r = 15$).

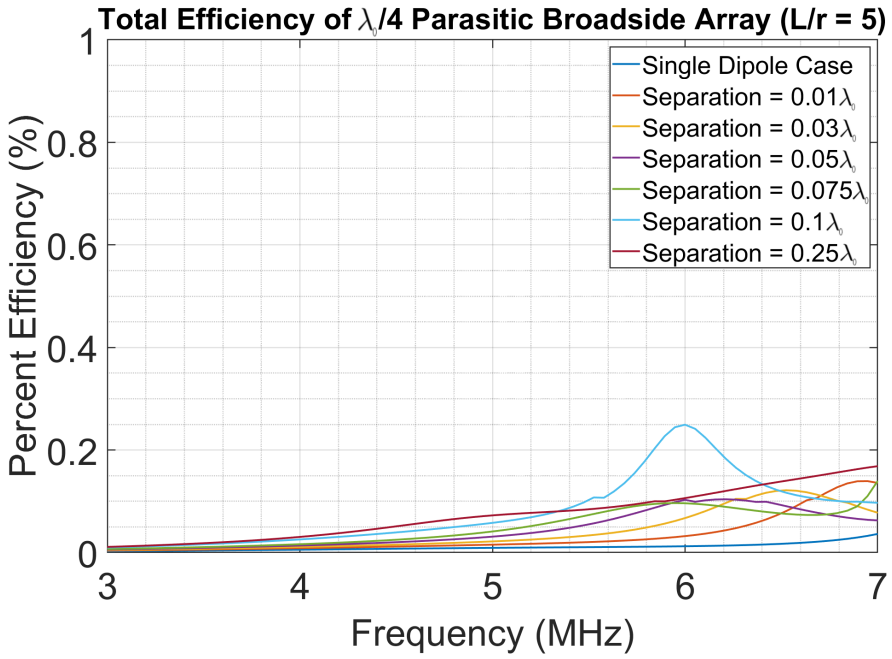

Figure 7.6: Variation across element separation in total aperture efficiency of a $\lambda/4$, parasitic, broadside array ($L/r = 5$).

In addition to the broadside array, the cornered and crossed arrays' results have interesting aspects worth discussing. In particular, for the $(L/r = 15)$ case, the total efficiency profiles of these two additional configurations, as displayed in fig. 7.7 and 7.11, align very closely to that of the broadside array, the only marked difference being the increase in depth in the dip present in the middle of the band of the singularly improved trace, which corresponds to an inter-element separation of 0.5λ in each case. As this dip brings a possibly advantageous increase in the two extrema at the end of the band, the variation in efficiency pattern across these three configurations may hold some application-specific benefits.

In terms of the realized gain patterns yielded by these two alternate configurations, very distinct behavior is visible not only between the two configurations themselves, but also across their respective bands, very similarly to fig. 7.2. Specifically, in fig.

7.8, a single, moderately focused beam is produced by the cornered aperture, with significant variation over the band, while in fig. 7.12, the crossed configuration yields a multi-beam pattern that shifts mildly, in terms of beam and null location across the band. Relative to their shared, single dipole, base case, both of these configurations have field patterns that, much like the broadside aperture, have increased realized gain, reaching maximums of 5-6 dB. Once again, moreover, these patterns do not quite meet the 9 dB goal put forth by the idealized, but non-physical, arrays presented in chapter 5.

The total efficiency of the cornered and cross configurations, when changed to the $(L/r = 5)$ case (fig. 7.9 and 7.13), once again behave extremely similarly to that of the broadside array, save for the shape of the field patterns of course. These patterns, as previously noted in chapter 5, depend almost exclusively on factors such as element configuration, and to a lesser extent, element separation and excitation frequency, as opposed to efficiency. In contrast, total efficiency of an aperture, as suggested in fig. 7.3-7.4, is dependent also on element spacing, but does not itself greatly impact the shape of the radiated fields. Further evidence of this trend is clearly visible in fig. 7.10 and 7.14, where, despite plotting the realized gain for extrema with different magnitudes from different traces, the approximate shapes of the field patterns remained unchanged. Rather, only the *magnitude* of the realized gain achieved by each of the two alternate configurations varies in fig. 7.10 and 7.14, as this metric *is* directly impacted by total efficiency. Additionally, one final observation on this topic can be easily made; specifically, in comparing fig. 7.8 to fig. 7.10, and fig. 7.12 to fig. 7.14, the resulting effect of increasing the elements' radii can be described as a broadening, or de-focusing, of the generated beams. The multi-beam pattern of the crossed aperture in fig. 7.12 especially, is deformed into a much more omni-directional pattern.

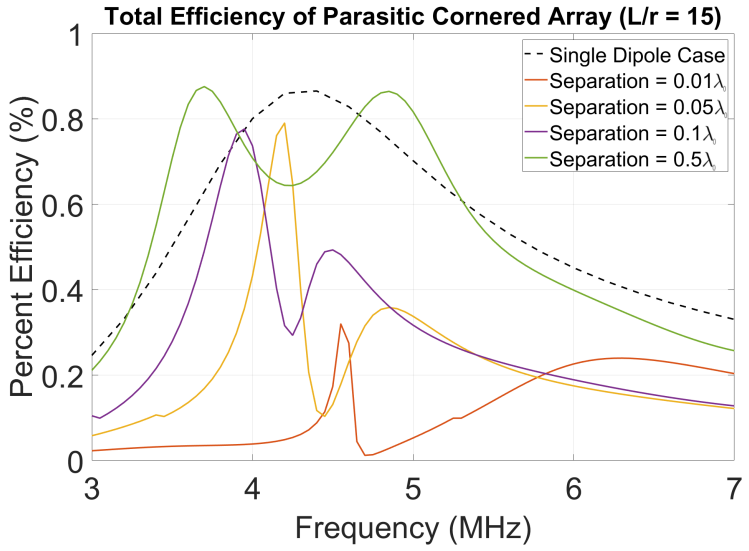

Figure 7.7: Variation across element separation in total aperture efficiency of a parasitic, cornered array $(L/r = 15)$.

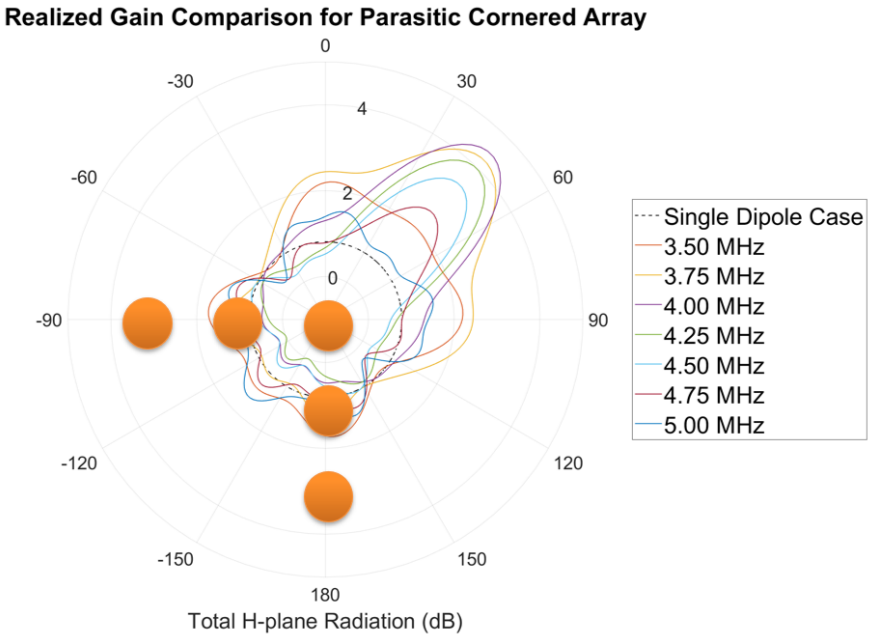

Figure 7.8: Variation across frequency in realized gain of a parasitic, cornered array $(L/r = 15)$. Note that all traces here correspond to the single, green trace in fig. 7.7

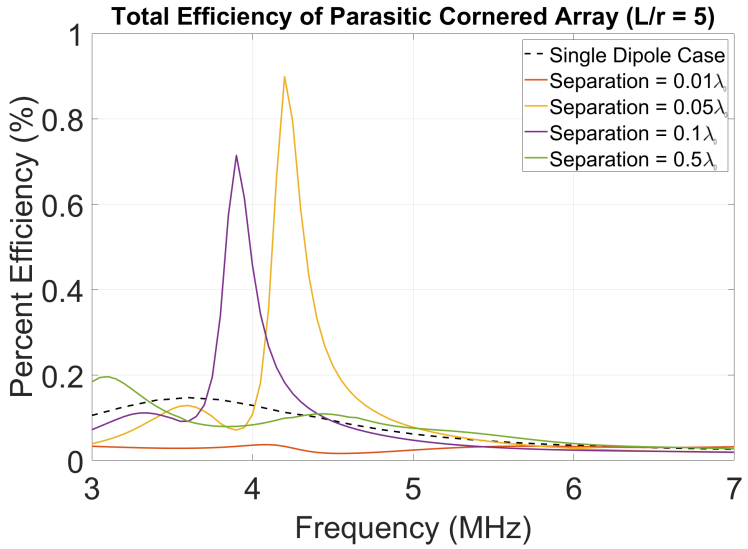

Figure 7.9: Variation across element separation in total aperture efficiency of a parasitic, cornered array $(L/r = 5)$.

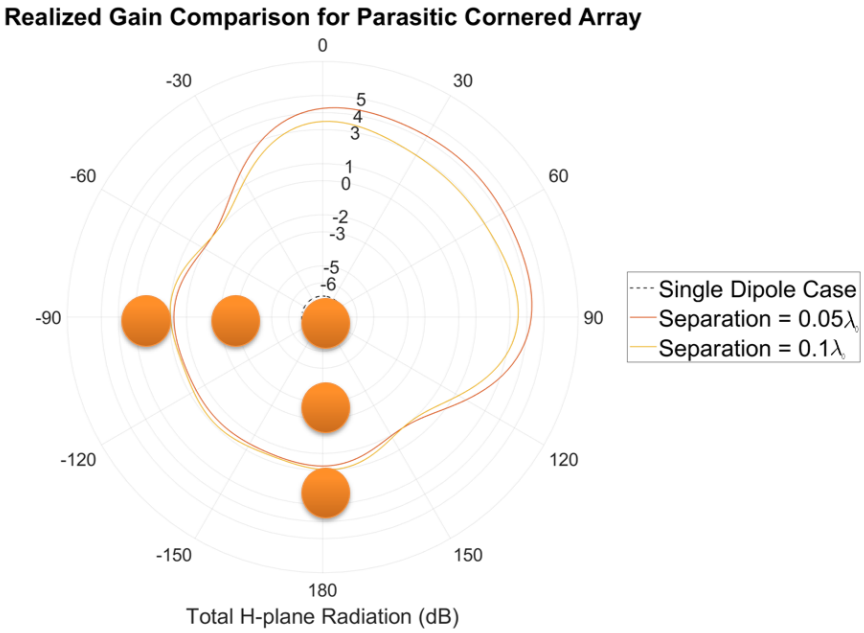

Figure 7.10: Variation across frequency in realized gain of a parasitic, broadside array $(L/r = 5)$. Note that each trace here corresponds to a different trace's extremum in fig. 7.9.

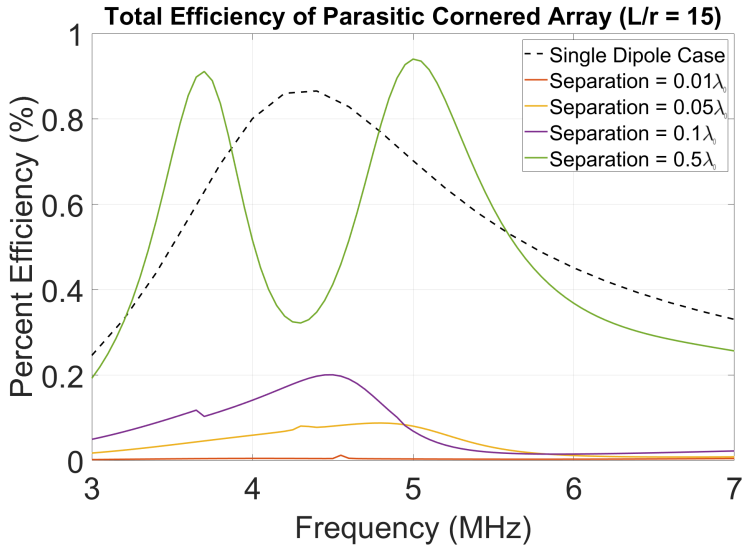

Figure 7.11: Variation across element separation in total aperture efficiency of a parasitic, crossed array $(L/r = 15)$.

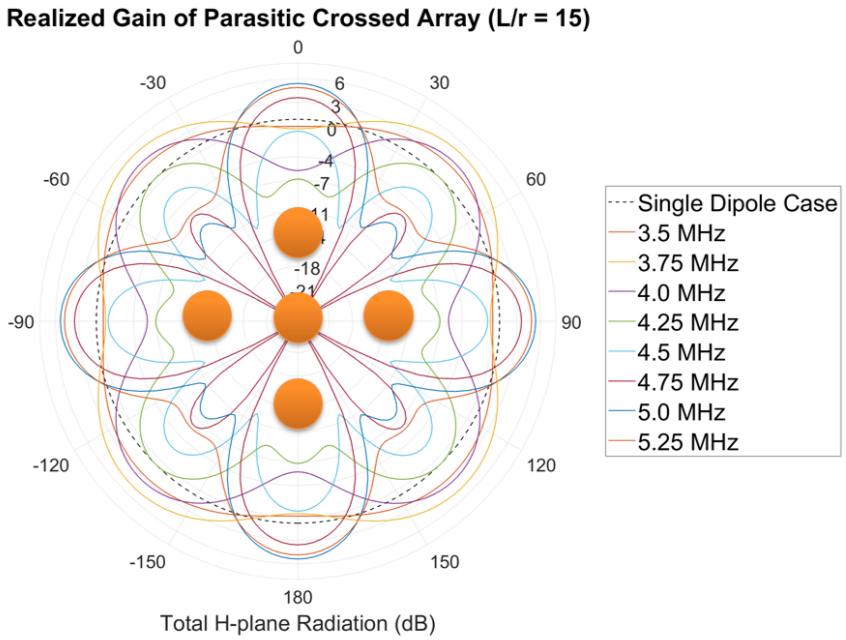

Figure 7.12: Variation across frequency in realized gain of a parasitic, broadside array $(L/r = 15)$. Note that all traces here correspond to the single, green trace in fig. 7.11

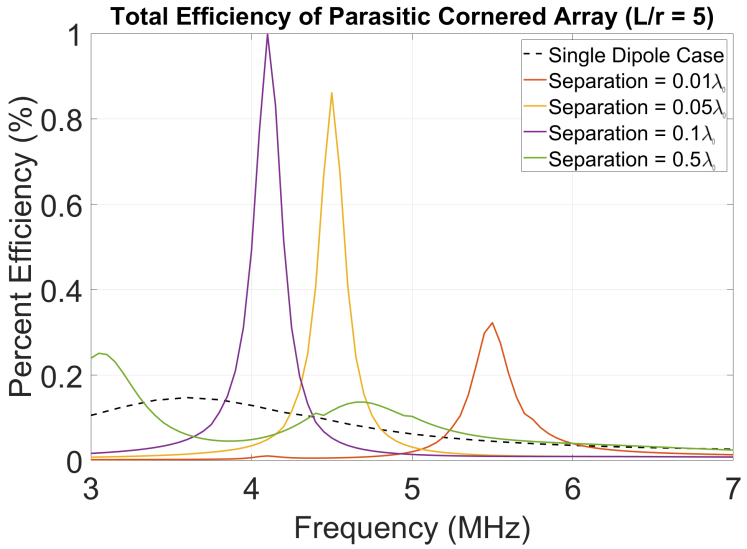

Figure 7.13: Variation across element separation in total aperture efficiency of a parasitic, crossed array $(L/r = 5)$.

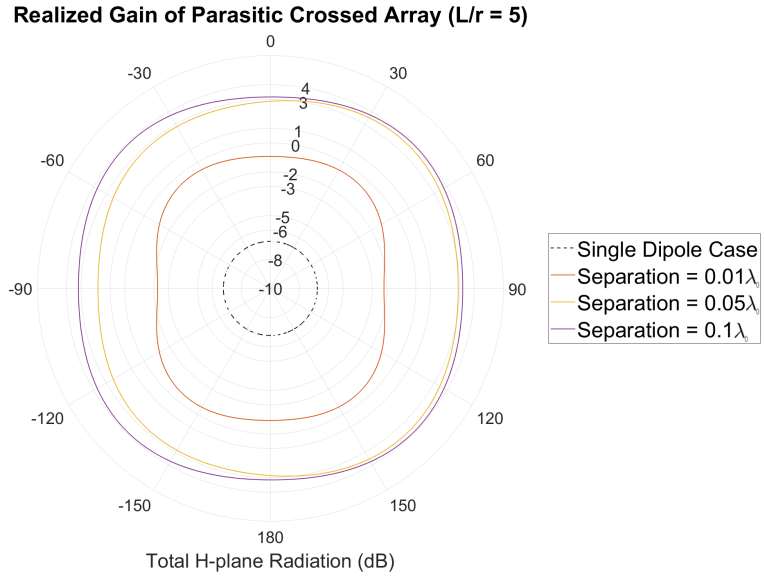

Figure 7.14: Variation across frequency in realized gain of a parasitic, broadside array $(L/r = 5)$. Note that each trace here corresponds to a different trace's extremum in fig. 7.13.

In summary, many of the total efficiency and realized gain calculations in this chapter suggest various application-specific utilities, especially in the case of the larger radii apertures, wherein a degree of frequency reconfigurability was evident. Additionally, the variation in azimuthal field patterns across the three aperture configurations was useful in characterizing the causal relationships between various metrics such as total frequency, efficiency magnitude, total efficiency bandwidth, gain shape, gain magnitude, and so on. Of particular interest was the direct relationship between field pattern shape and array configuration, the only other significant factor being frequency, suggesting how knowledge of the total efficiency of one configuration lends great insight into that of another. Finally, it's worth remarking that these trends continue with driven dipole arrays, which are explored in the next chapter.

Chapter 8

Five-element Driven Dipole Arrays

8.1 Chapter Overview

In this chapter, the same array configurations from chapter 7 will be considered anew, now with all 5 elements in each aperture driven by a gap-voltage source. One particularly important distinction between this chapter and the previous one, however, is in the control mechanisms used to reconfigure the given aperture. Specifically, while the tuning control mechanism used in chapter 7 was limited to array configuration and inter-element spacing, the arrays explored in this chapter will have the added control mechanism of phase shifting. Specifically, within a measured aperture, the elements will have relative phase offsets in order to properly make use of tight-coupling; the mutual impedance curves described in chapter 6 can thus be used more effectively, as, per equation (2.14), the driving-point impedance of a radiator at its port is heavily influenced by not only the self- and mutual impedances present in the nearby environment, but also by the ratio of currents on these nearby structures. Therefore, the relevance of this ratio, naturally, is not limited to the magnitudes of said currents, but rather includes the differences in excitation phase as well. While the precise nature of the phase relationship between a voltage excitation and the resulting current, that is the degree of either leading or lagging present in said current, is of course a function of

the self- and mutual impedances present, control over voltage phase is nonetheless a useful tool, as will be demonstrated. Additionally, for the sake of somewhat simplifying the subsequent analyses, all excitations will have unitary magnitudes, leaving the aforementioned current ratio as solely a ratio of phase angles.

Furthermore, beyond the discussion of phase control, this chapter will also treat the two different radii cases common in previous chapters, $(L/r = 5)$ and $(L/r = 15)$, with increased distinction, hence the subsequent section titles of "Larger Radii" and "Smaller Radii". Both of these cases are of course, in the more general study of radiating cylinders, well described as having "large" radii; the terminology presented herein serves only to better distinguish the two analyzed cases. While other dipole length-to-radius ratios may of course be of interest depending on the application, the two used throughout this thesis simply represent the bounds of the region of immediate interest. Finally, while the previous chapter focused fairly evenly on all three of the named array configurations in order to demonstrate the differences in their respective radiation pattern shapes, this chapter will focus primarily on the cornered array, as well as the broadside array to a lesser extent, for a couple of reasons. In particular, beyond just brevity, the trends that will be seen in this chapter, just as was the case in the previous chapter, will apply very similarly to all three configurations, consequently limiting the utility of showing the entire breadth of calculated variations.

8.2 The Larger Radii Case

As was observed in the previous chapter, the larger radius case, $(L/r = 5)$, when set in the context of a parallel coupling-based array, has a tendency to produce peaks in total aperture efficiency such that different inter-element spacings have extrema at different frequencies. In other words, as long as the previously established threshold of

50% total efficiency can be reached, this larger radii case often demonstrates a strong potential for frequency reconfigurability applications. This trend visibly continues in the driven array domain as well, specifically in fig. 8.1-8.3, where each figure displays variation in the efficiency extrema with changing inter-element spacing; fig. 8.2 and 8.3 are particularly well suited as evidence of this trend, having both reasonably large extrema and significant separation in the bands corresponding to different spacings. Furthermore, these three figures together begin to demonstrate an exceptionally important characteristic specific to driven arrays with phase control.

To expand on this characteristic, note firstly that the three figures differ only in terms of the phase step, $\Delta\theta$, present between each of the elements in the observed aperture. In other words, if the central cylinder in the array is defined to have an "initial" phase of 0°, then the immediately adjacent elements would be assigned a phase addend of $\pm\Delta\theta$, while the outer elements would likewise be assigned addends of $\pm 2\Delta\theta$. Secondly, note that as this phase step grows across the three figures, so too do the separations values possessing significant extrema for that phase step. Accordingly, this proportionality speaks to the expected, larger three-way relationship that exists for tightly-coupled arrays between frequency, phase length, and physical size; this relationship of course is quite similar to that common to virtually all electromagnetics. In particular, for any constancy in one of the three aspects, there exists a specific proportionality between the other two. To be explicit, firstly, as was just mentioned, as the size of the antenna array is increased by way of the inter-element spacing, it follows that in order for the aperture's peak operating frequency (defined here in terms of total efficiency) to remain unchanged, the phase length of the array should necessarily be increased proportionally. This is obviously achieved via control of the inter-element phase-step. Secondly, for a single phase step value, it should be expected that the peak operating frequency follows the physical size of the array; this is easily observed in fig. 8.1-8.3, as increas-

ing the physical spacing is shown to lead to extrema at lower frequencies. Finally, the third proportionality will be elaborated upon shortly, as well as in the next section.

The preceding discussion is rather useful as it partially clarifies the nature of a tightly-coupled array, in contrast to both single-body radiators, and more traditional, mutual impedance-free arrays. In particular, it should be noted here that the above references to phase length are, in a sense, distinct from electrical size, as the phase length is artificially controlled via the excitation phase step, while electrical length is of course directly determined by physical size. Consequently, tightly-coupled arrays like those in this thesis, which do not experience currents (save for possibly displacement currents) across their lengths, are unlike single radiators, wherein electrical and phase length are mutually determined, all other factors being the same. Additionally, relative to phased array-type structures, wherein mutual impedance is necessarily mitigated such that each element experiences minimal change in impedance behavior upon insertion into the larger array, tightly-coupled arrays, as hereto presented, drastically change the behavior of the individual elements. This is evidenced by the previously described proportionalities presented in fig. 8.1-8.3, as well as those throughout the rest of this chapter.

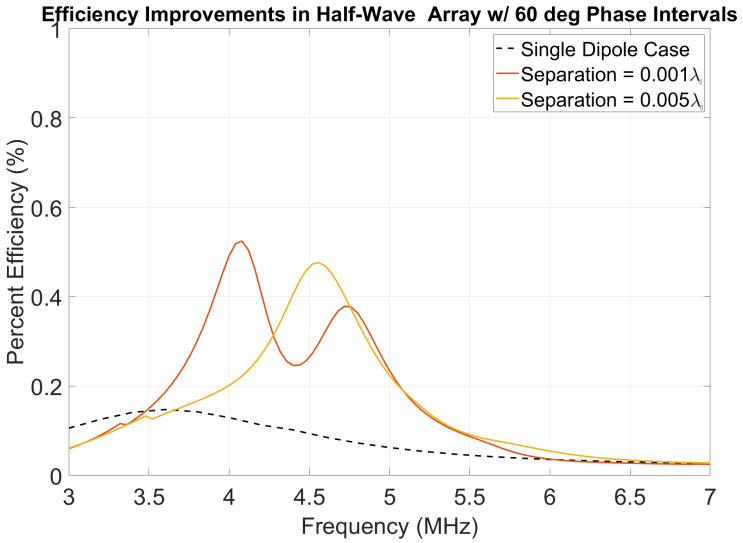

Figure 8.1: Separation values with total efficiency curves possessing significant extrema at $\Delta\theta = 60°$. Half-wave broadside array. $(L/r = 5)$.

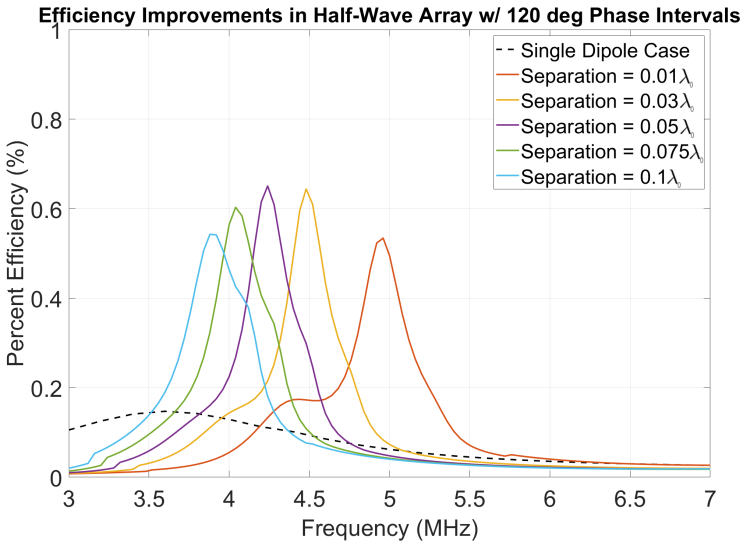

Figure 8.2: Separation values with total efficiency curves possessing significant extrema at $\Delta\theta = 120°$. Half-wave broadside array. $(L/r = 5)$.

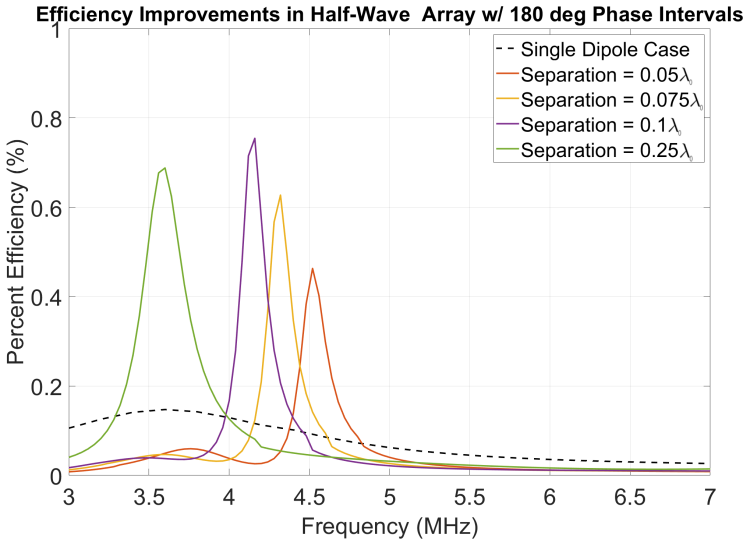

Figure 8.3: Separation values with total efficiency curves possessing significant extrema at $\Delta\theta = 180°$. Half-wave broadside array. $(L/r = 5)$.

A more complete transition across phase step, this time for the cornered array, can be seen in fig. 8.4-8.13, where $20°$ phase steps are used. Note how many of the previously characterized relationships are once again present in this series of figures. In particular, notice how the smallest two separations have their maximal extrema in the range of $60° - 100°$, the middle few spacing values are approximately maximized from $120°$ onward, and the largest separation values only reach maximal peak values close to $180°$. This transitional series provides a very clear example of how certain antenna apertures may achieve frequency reconfigurability by way of control mechanisms such as physical reconfiguration and excitation phase adjustments.

Additionally, with the respect to the third proportionality relationship referred to above, this is reasonably visible in these figures, as, for any choice of a separation value, and by extension some physical array length, the extremum of that curve moves up in frequency with increasing phase separation. This trend can in fact be observed

throughout much of this chapter.

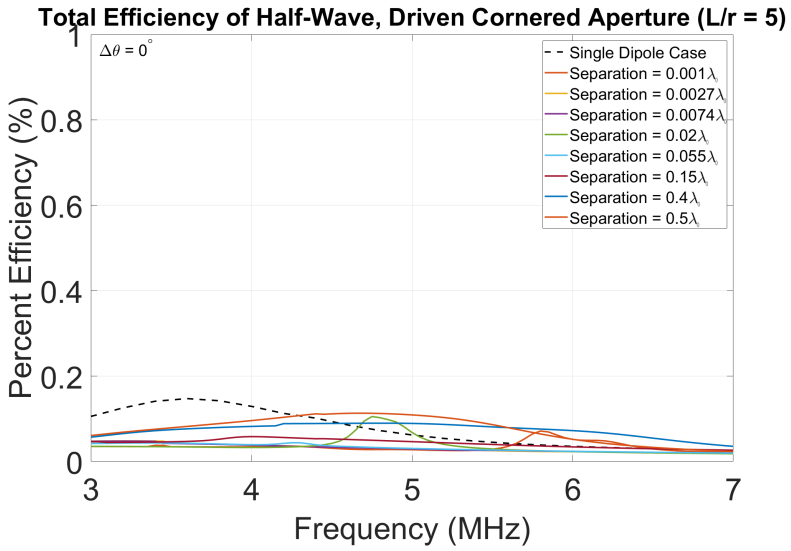

Figure 8.4: All total efficiency curves at $\Delta\theta = 0°$. Half-wave cornered array. $(L/r = 5)$.

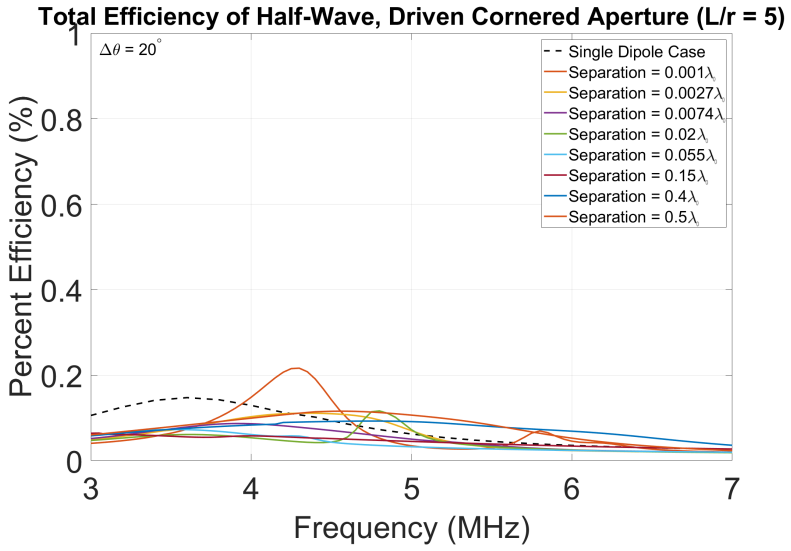

Figure 8.5: All total efficiency curves at $\Delta\theta = 20°$. Half-wave cornered array. $(L/r = 5)$.

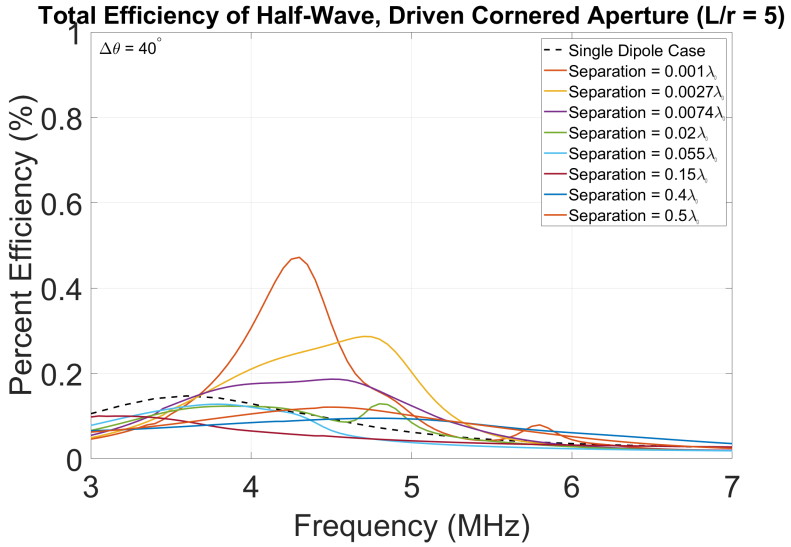

Figure 8.6: All total efficiency curves at $\Delta\theta = 40°$. Half-wave cornered array. $(L/r = 5)$.

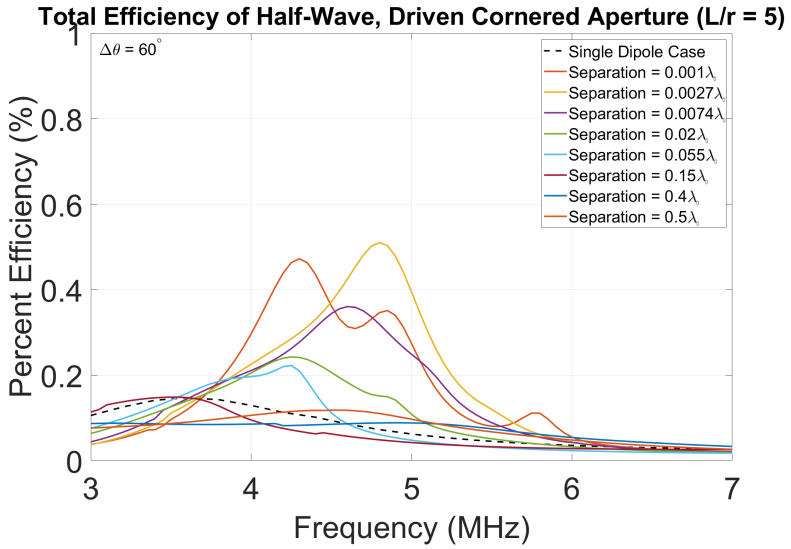

Figure 8.7: All total efficiency curves at $\Delta\theta = 60°$. Half-wave cornered array. $(L/r = 5)$.

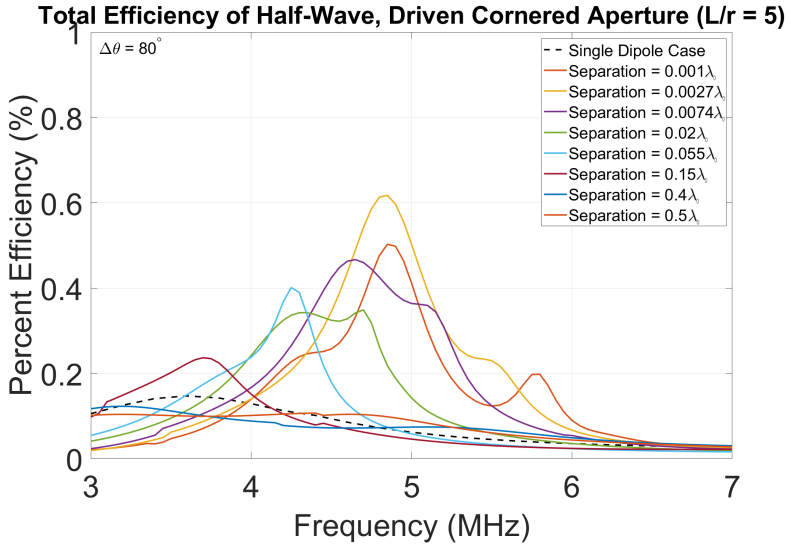

Figure 8.8: All total efficiency curves at $\Delta\theta = 80°$. Half-wave cornered array. $(L/r = 5)$.

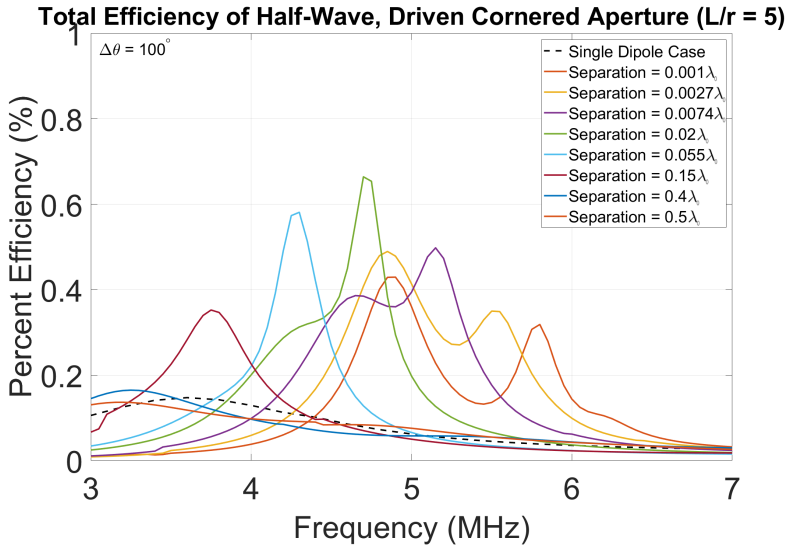

Figure 8.9: All total efficiency curves at $\Delta\theta = 100°$. Half-wave cornered array. $(L/r = 5)$.

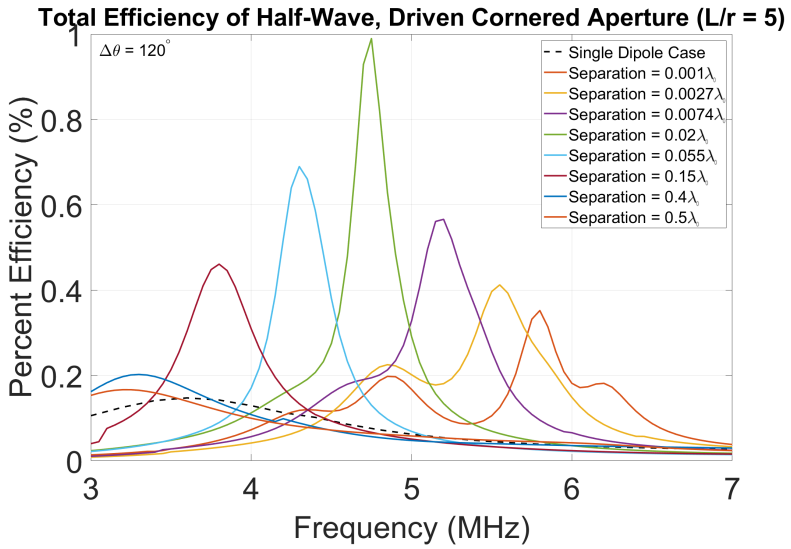

Figure 8.10: All total efficiency curves at $\Delta\theta = 120°$. Half-wave cornered array. $(L/r = 5)$.

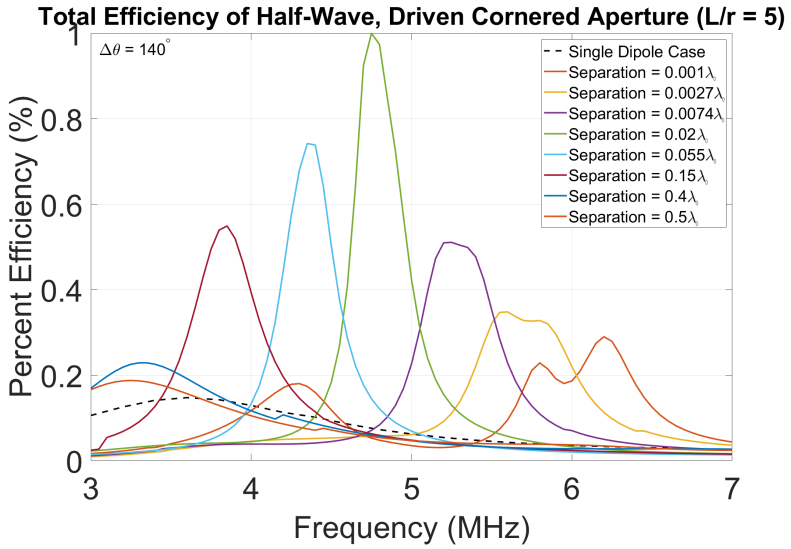

Figure 8.11: All total efficiency curves at $\Delta\theta = 140°$. Half-wave cornered array. $(L/r = 5)$.

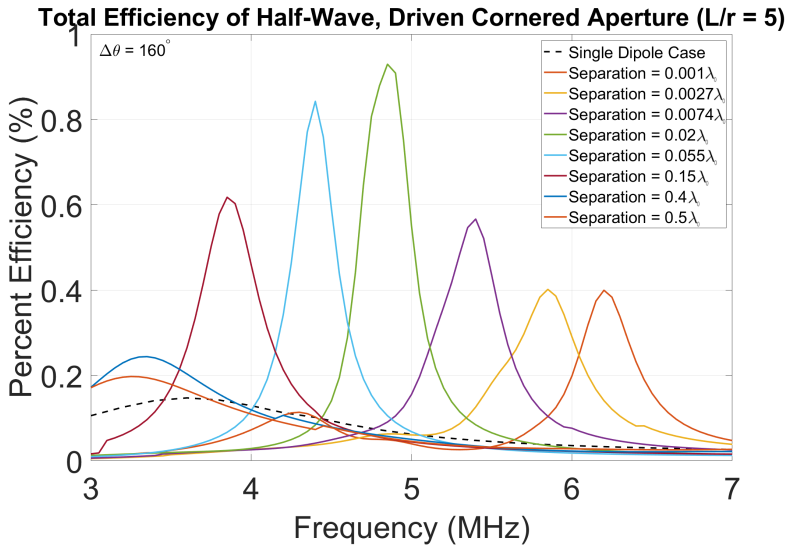

Figure 8.12: All total efficiency curves at $\Delta\theta = 160°$. Half-wave cornered array. $(L/r = 5)$.

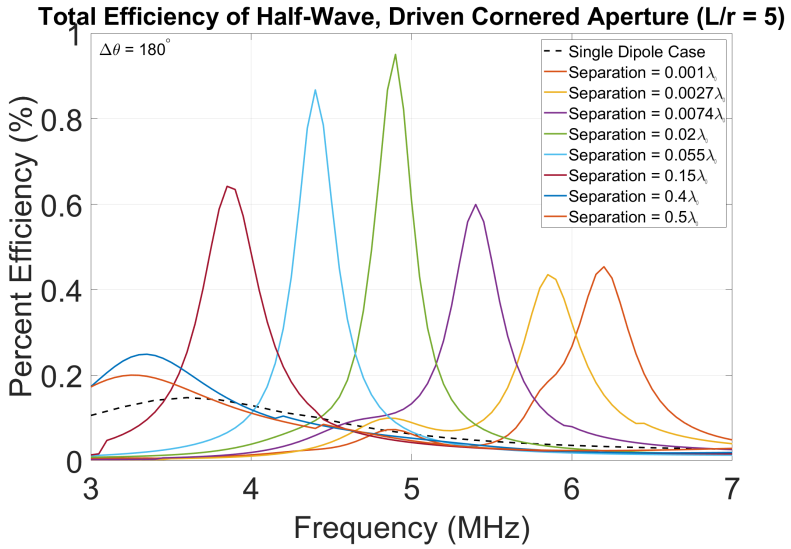

Figure 8.13: All total efficiency curves at $\Delta\theta = 180°$. Half-wave cornered array. $(L/r = 5)$.

Finally, it is worthwhile describing here how the frequency reconfigurability de-

scribed in this section may also prove useful with respect to increasing the positional error tolerance of an SUAS. Specifically, small deviations away from the desired relative element positioning will produce naturally small detriments in the efficiency, and thus maximal gain, of the array. This is of course due to the fact that in moving inadvertently from one spacing scheme to another, the new spacing will not likely host the operational frequency with quite the same efficiency. However, so long as these deviations are detectable, they may likely be corrected by utilizing the proportionality between frequency and phase step described above. In particular, because the phase step has only a rather slow effect on the frequency shifting of efficiency extrema, as seen above, minor deviations may be stably corrected without concern that very precise phase control be needed. In the same way though, this correction technique is likely limited to more minor deviations, those being on the same order of magnitude as the original spacing serving as a rough upper bound. Nonetheless, it is the case that the tightly-coupled arrays described thus far are not especially sensitive to phase errors, as evidenced by the limited changes between $20_\circ$ phase step changes.

8.3 The Smaller Radii Case

In this final section, the last class of analysis, the $(L/r = 15)$ case, will be discussed. To begin, in fig. 8.14-8.18, the total efficiency of both the broadside and the cornered array are visible for a small variety of phase steps. In particular, while a more gradual transitional series, like that of the previous section, may be easily shown, as these five figures demonstrate, the results relative to the single dipole are not nearly as impressive, only in part due to the $(L/r = 15)$ cylinder already being a fairly decent radiator for not too small of a band. What positive results these graphs do demonstrate, however, are best seen in fig. 8.16-8.18, specifically. In these three, considerable frequency shifting

under changes in element spacing is visible, and, depending on the application-specific performance requisites, some of these variations may indeed be useful. The four tallest traces in fig. 8.16 are particularly interesting as they demonstrate frequency shifting similar to that of the previous section, but with both better magnitude of the extrema (only relative to the previous section's traces, not this section's base case), and wider bandwidths. Thus, while not as great an improvement over the base case compared to the previous section, the variations presented for the cornered array here are nonetheless somewhat successful as a proof-of-concept.

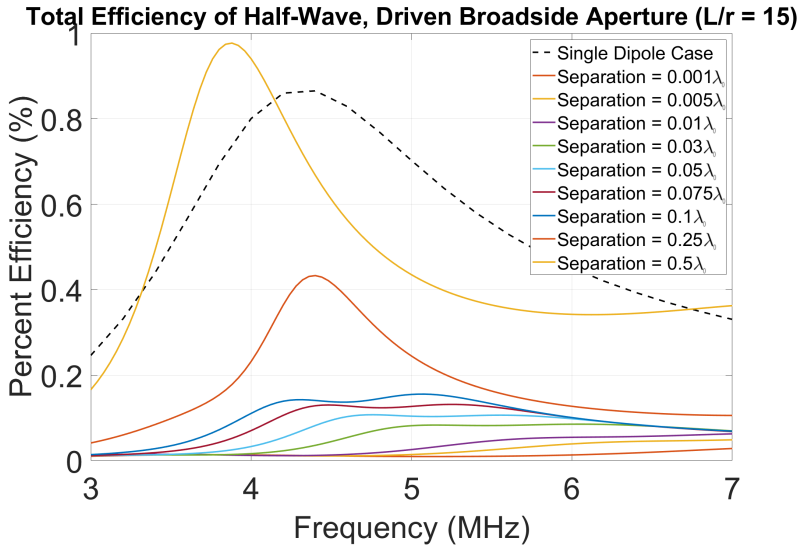

Figure 8.14: All total efficiency curves at $\Delta\theta = 180°$. Half-wave broadside array. $(L/r = 15)$.

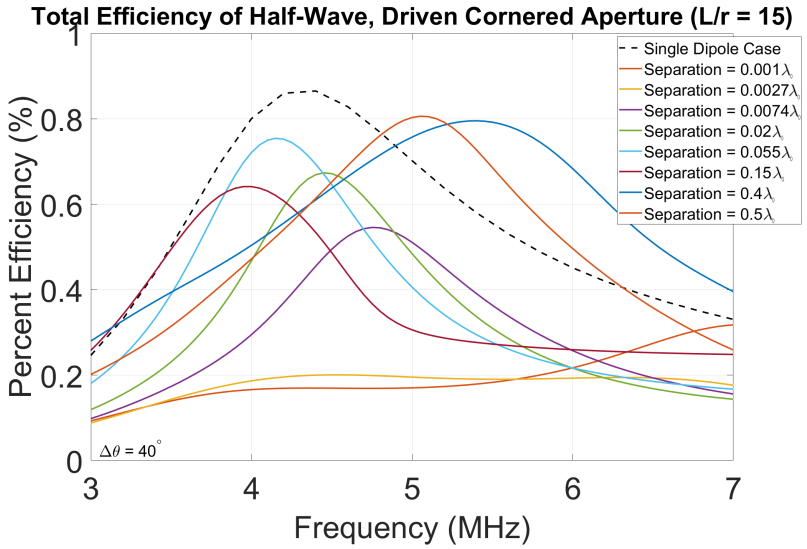

Figure 8.15: All total efficiency curves at $\Delta\theta = 40°$. Half-wave cornered array. $(L/r = 15)$.

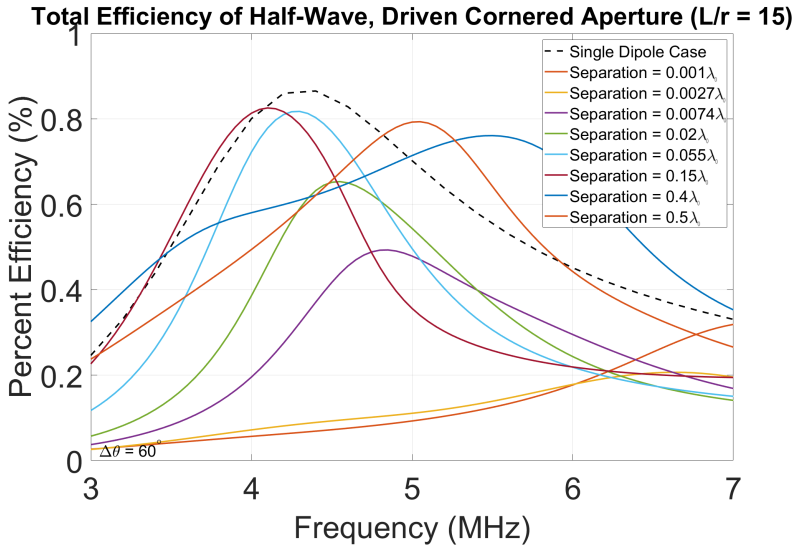

Figure 8.16: All total efficiency curves at $\Delta\theta = 60°$. Half-wave cornered array. $(L/r = 15)$.

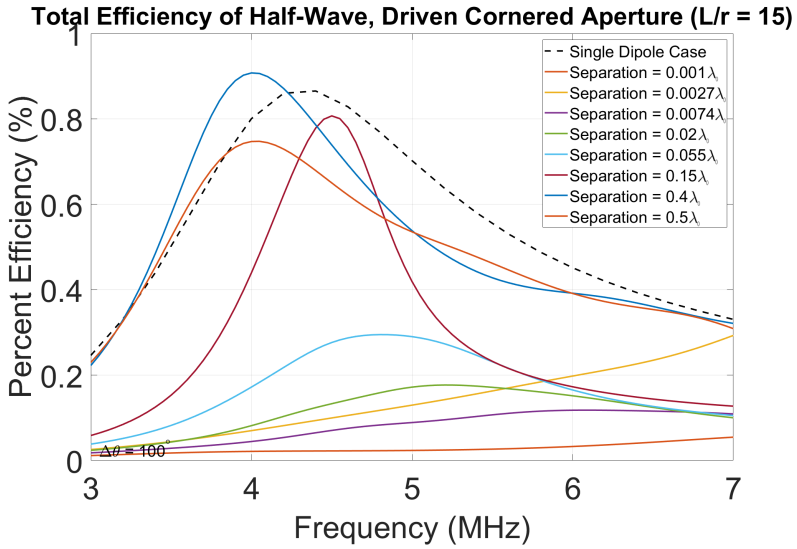

Figure 8.17: All total efficiency curves at $\Delta\theta = 120°$. Half-wave cornered array. $(L/r = 15)$.

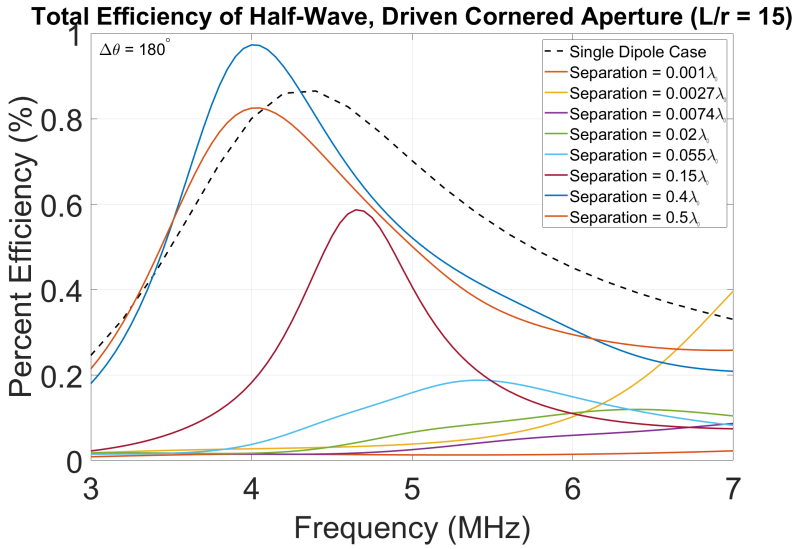

Figure 8.18: All total efficiency curves at $\Delta\theta = 180°$. Half-wave cornered array. $(L/r = 15)$.

Finally, in fig. 8.19-8.24, similar data for the broadside and cornered arrays is pre-

sented, this time showing the variation in maximal total efficiency across phase step size for a small number of inter-element separation distances. With this new data set, the previous discussion of this section is reinforced; specifically, these figures further evince the notion that tightly-coupled arrays may be able to achieve frequency reconfigurability. It is, however, the case that the specific degree of frequency reconfigurability achieved in this section can be interpreted as inferior to that of the previous section as the improvement relative to the base is weaker, implying less effect from any tight-coupling present, although this interpretation is likely application-dependent. At this point, one last interesting question that may be raised is whether any further improvement, and if so, how much, may be achieved through the construction of larger arrays, numbering perhaps ten or twenty elements, instead of the five-elements arrays presented thus far. That answer, however, is not addressed here.

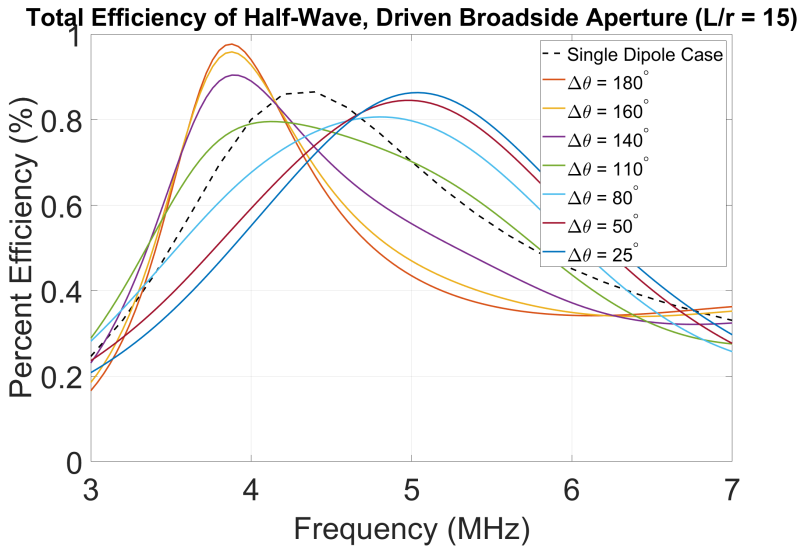

Figure 8.19: All total efficiency curves with separation 0.5λ. Half-wave broadside array. $(L/r = 15)$.

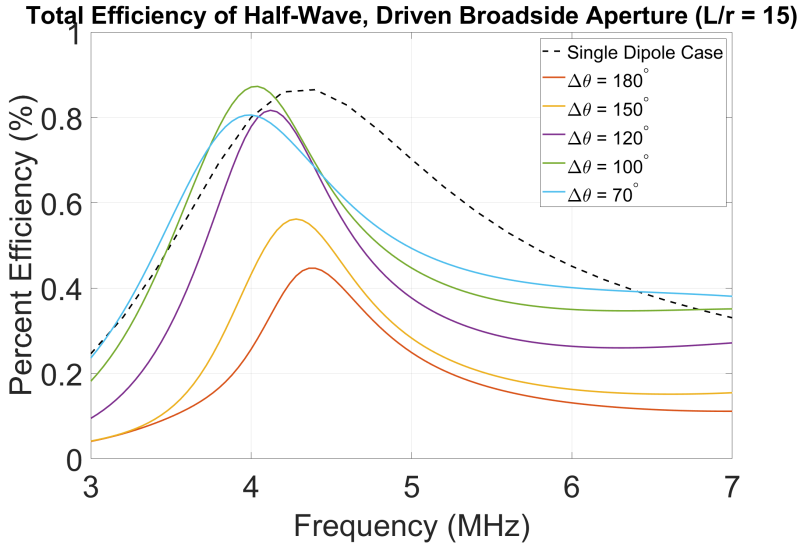

Figure 8.20: All total efficiency curves with separation 0.25λ. Half-wave broadside array. $(L/r = 15)$.

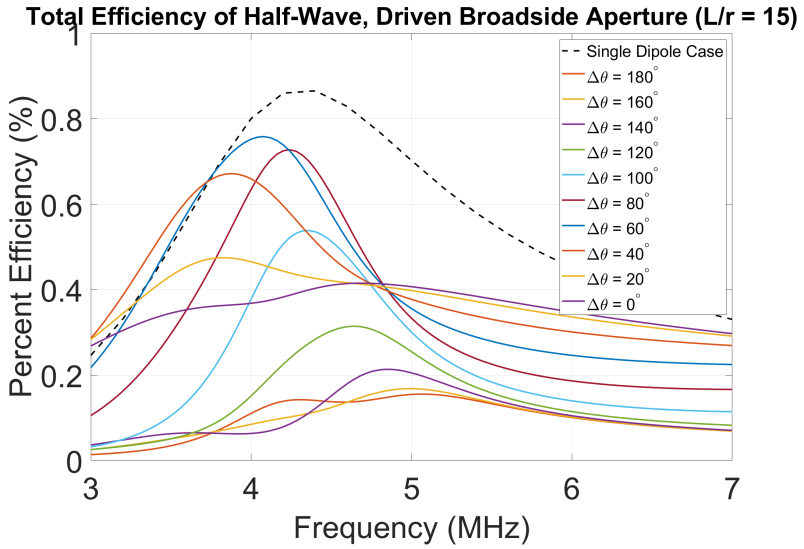

Figure 8.21: All total efficiency curves with separation 0.1λ. Half-wave broadside array. $(L/r = 15)$.

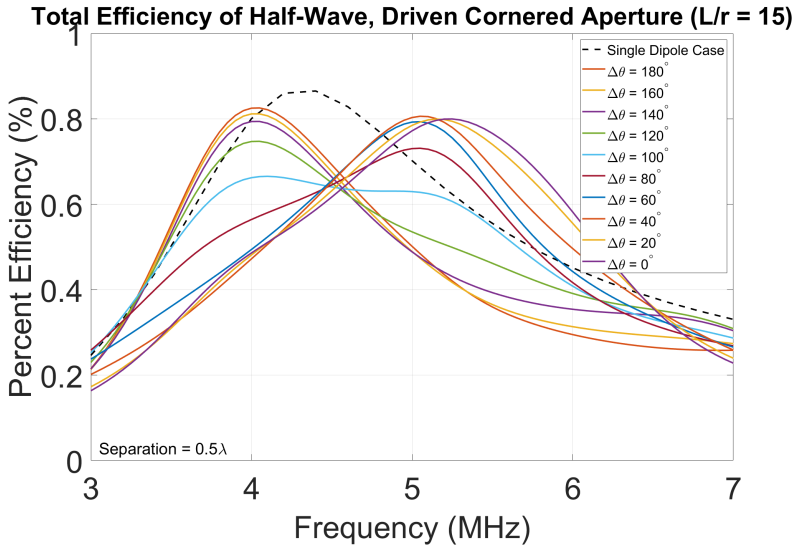

Figure 8.22: All total efficiency curves with separation 0.5λ. Half-wave cornered array. $(L/r = 15)$.

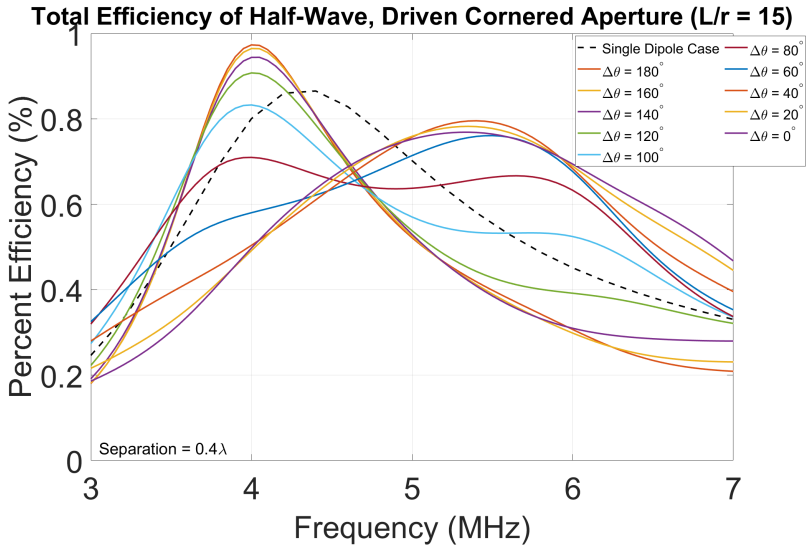

Figure 8.23: All total efficiency curves with separation 0.4λ. Half-wave cornered array. $(L/r = 15)$.

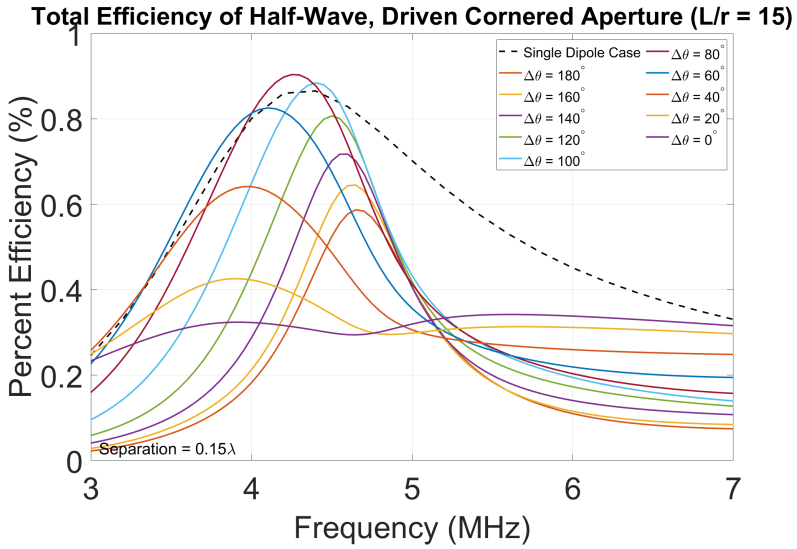

Figure 8.24: All total efficiency curves with separation 0.15λ. Half-wave cornered array. $(L/r = 15)$.

Chapter 9

Conclusions and Future Work

9.1 Conclusions

In summary, this thesis has reached and elucidated a number of meaningful insights and conclusions regarding topics related to the nature and behavior of cylindrical radiators, whether in isolation or in various contexts. Primarily however, this work was an exploration into the feasibility of tightly-coupled SUAS under a number of simplifying constraints, the most significant of these being the reduction of the complex physical shape of a fixed-wing aircraft to a single, considerably thick cylinder, and the limitation of usable inter-element coupling mechanisms to the two mechanisms most feasibly achieved by airborne bodies. Furthermore, when discussing the "feasibility" of tight-coupling in the context of SUAS, this was predominantly defined as the transformation of a single cylinder's aperture into an entirely new, synthetic one constructed by way of array formation, wherein performance could be most easily evaluated with metrics such as total efficiency and realized gain.

To this end, a baseline used to define the realistic and idealized behavior of single cylindrical radiators was created. It was therefore observed that as the length-to-radius ratio and electrical length of a cylindrical dipole decreases, so too does its ability to radiate, possessing neither sufficient radiation resistance to form an appropriate impedance

match with realistic electronic systems, nor to prevent the accumulation of excess waste heat caused by poor radiation efficiency. Subsequently, the coupling strength and applicability of the two inter-element coupling mechanisms were analyzed; it was found that the parallel, longitudinal coupling between the axially-directed currents on the cylinder bodies was superior on both counts, as it allows for greater mutual impedance with which a single cylinder's aperture may be transformed.

In the analysis of arrays, configurations of tightly-coupled but poor radiators were constructed and studied, such that from the mutual interaction of these elements, the synthesis of an entirely new aperture may result, wherein performance factors would be improved, and additional features like frequency reconfigurability could be utilized. In this way, both parasitic arrays with only a single driven element, and fully-driven arrays with five driven elements were found to possess this potential. In particular, arrays with especially radii were found to be especially suitable for tight-coupling techniques, as immense changes relative to the singular, base-case cylinder were found. Moreover, significant insight into the general relationship between an array's physical size, phase length, and ideal operating frequency was developed; in particular, it was found that when one of these aspects is held constant, a specific proportionality exists between the other two. It was also subsequently found that the fully-driven arrays, in having multiple control mechanisms, possessed significant potential to be useful in increasing the positional error tolerance of SUAS.

Additionally, the variation in radiation patterns due to distinct array configurations was studied. Cornered arrays were subsequently found to produce the most focused beams, while crossed arrays, by contrast, were found to often produce very omni-directional patterns. Finally, it was also determined that in the context of tightly-coupled apertures, the shape of an array's radiation pattern shape is largely independent of the elements' physical dimensions and relative spacing, demonstrating how changes

in the array's total efficiency acted only to scale the radiation pattern.

9.2 Scientific Impact

In being an exploratory project, this work has been largely successful simply in investigating the degree to which a tightly-coupled SUAS may be usefully modeled under the aforementioned constraints. In particular, this serves as a contribution to the general understanding of both cylindrical radiators and tightly-coupled arrays. To be even more precise, chapter 5 serves as an extension to general scientific knowledge on the topic of large-radius cylindrical radiators, while chapter 6 does the same for two forms of inter-radiator coupling therein.

Beyond the successful exploration of poorly documented regions in antenna theory, this work also makes considerable strides in the development of knowledge related to airborne-based radiating systems. Specifically, by demonstrating in chapters 7 and 8 how tight-coupling can be positively used to synthesize larger antenna apertures with features such as improved bandwidth, improved total efficiency, and potentially frequency reconfigurability, the scientific understanding of techniques for developing wideband and reconfigurable systems is augmented. This is doubly true in the context of small-bodied SUAS where SWaP constraints are often very restrictive, and thus require new and increased understanding of specialized systems development.

9.3 Future Work

In moving forward with this project, several significant possibilities for the extension and improvement of this work are readily conceived. In particular, it will be of great use, as was previously mentioned, to extend these analyses to arrays with greater numbers of elements, in an attempt to assess the limit behavior of the techniques evaluated

hereto. Furthermore, as one of the principles drawbacks discussed in chapters 7 and 8 is the weakness of the two studied inter-element coupling mechanisms, a step that will necessarily be taken in the future will be in the development of a somewhat more complex model that allows for these mechanisms to function with greater efficacy. Whether this manifests as a model for analyzing the wings of an aircraft, or perhaps modeling its wings and fuselage as a sort of crossed dipole- that much of course has yet to be determined. These possibilities, nonetheless, would be likely to improve the results found hereto. Extending this notion, further work will likely also involve the use of characteristic modes and perturbation analyses, as such allow for vastly more accurate modeling of fixed-wing structures, albeit with an unavoidable increase in computational complexity.

Additional aspects that will most likely be of great importance to this project moving forward include the development and analysis of more realistic UAV-body excitations, the voltage gap model used in this work being largely unsuitable for real-world UAS, for obvious mechanical reasons. Beyond this, more detailed studies on the relevance of positional error tolerance will assuredly be vital, as the control issue surrounding SUAS is still a very considerable hurdle in the development of SUAS. Finally, some minor studies into the effect of very non-ideal conductivity will likely be of use, as it cannot be expected that all UAV bodies, even when metalized, will be of an ideal conductivity, copper and silver being fairly expensive construction materials.

References

[1] M. I. Skolnik, *Radar handbook*. McGraw-Hill Education, 2008.

[2] J. C. Curlander and R. N. McDonough, *Synthetic aperture radar*. Wiley, New York, 1991, vol. 11.

[3] N. Levanon and E. Mozeson, *Radar signals*. John Wiley & Sons, 2004.

[4] M. E. Davis, "Developments in foliage penetration radar," in *2009 International Radar Conference" Surveillance for a Safer World"(RADAR 2009)*, IEEE, 2009, pp. 1–6.

[5] S. J. Munchak, "Remote sensing of precipitation from airborne and spaceborne radar," in *Remote Sensing of Aerosols, Clouds, and Precipitation*, Elsevier, 2018, pp. 267–299.

[6] J. Granger and J. Bolljahn, "Aircraft antennas," *Proceedings of the IRE*, vol. 43, no. 5, pp. 533–550, 1955.

[7] Y. Chen and C.-F. Wang, "Electrically small uav antenna design using characteristic modes," *IEEE Transactions on Antennas and Propagation*, vol. 62, no. 2, pp. 535–545, 2013.

[8] Z.-Q. Liu, Y.-S. Zhang, Z. Qian, Z. P. Han, and W. Ni, "A novel broad beamwidth conformal antenna on unmanned aerial vehicle," *IEEE Antennas and Wireless Propagation Letters*, vol. 11, pp. 196–199, 2012.

[9] K. Obeidat, R. G. Rojas, and B. Raines, "Design of antenna conformal to v-shaped tail of uav based on the method of characteristic modes," in *2009 3rd European Conference on Antennas and Propagation*, IEEE, 2009, pp. 2493–2496.

[10] L. Gupta, R. Jain, and G. Vaszkun, "Survey of important issues in uav communication networks," *IEEE Communications Surveys & Tutorials*, vol. 18, no. 2, pp. 1123–1152, 2015.

[11] E. W. Frew and T. X. Brown, "Airborne communication networks for small unmanned aircraft systems," *Proceedings of the IEEE*, vol. 96, no. 12, 2008.

[12] I. Lachow, "The upside and downside of swarming drones," *Bulletin of the atomic scientists*, vol. 73, no. 2, pp. 96–101, 2017.

[13] *Antenna theory - antenna arrays*. [Online]. Available: https://www.tutorialspoint.com/antenna_theory/antenna_theory_arrays.htm.

[14] F. Namin, J. S. Petko, and D. H. Werner, "Analysis and design optimization of robust aperiodic micro-uav swarm-based antenna arrays," *IEEE Transactions on Antennas and Propagation*, vol. 60, no. 5, pp. 2295–2308, 2012.

[15] M. A. Richards, *Fundamentals of radar signal processing*. McGraw-Hill Education, 2014.

[16] *The impact of frequency in non-contacting ...* 2016. [Online]. Available: https://www.emerson.com/documents/automation/white-paper-impact-of-frequency-in-non-contacting-radar-level-measurement-rosemount-en-us-175148.pdf.

[17] D. M. Pozar, *Microwave engineering*. John wiley & sons, 2011.

[18] J. G. Proakis and M. Salehi, *Digital communications*. McGraw-Hill., 2008.

[19] J. D. Kraus, M. Tiuri, A. V. Räisänen, and T. D. Carr, *Radio astronomy*. Cygnus-Quasar Books Powell, Ohio, 1986, vol. 69.

[20] V. Pierro, V. Galdi, G. Castaldi, I. M. Pinto, and L. B. Felsen, "Radiation properties of planar antenna arrays based on certain categories of aperiodic tilings," *IEEE transactions on antennas and propagation*, vol. 53, no. 2, pp. 635–644, 2005.

[21] A. A. Abouda, H. M. El-Sallabi, and S. Haggman, "Impact of antenna array geometry on mimo channel eigenvalues," in *2005 IEEE 16th International Symposium on Personal, Indoor and Mobile Radio Communications*, 2005.

[22] J. Petko and D. Werner, "Positional tolerance analysis and error correction of micro-uav swarm based antenna arrays," in *2009 IEEE Antennas and Propagation Society International Symposium*, IEEE, 2009, pp. 1–4.

[23] J. Garza, M. A. Panduro, A. Reyna, G. Romero, and C. d. Rio, "Design of uavs-based 3d antenna arrays for a maximum performance in terms of directivity and sll," *International Journal of Antennas and Propagation*, vol. 2016, 2016.

[24] S. Yeh, J.-F. Chamberland, and G. H. Huff, "An investigation of geolocation-aware beamforming algorithms for swarming uavs," in *2017 IEEE International Symposium on Antennas and Propagation & USNC/URSI National Radio Science Meeting*, IEEE, 2017, pp. 641–642.

[25] K. R. Buchanan, "Theory and applications of aperiodic (random) phased arrays," Ph.D. dissertation, 2014.

[26] C. A. Balanis, *Antenna theory: analysis and design*. John wiley & sons, 2015.

[27] C. G. Buxton, "Design of a broadband array using the foursquare radiating element," Ph.D. dissertation, Virginia Tech, 2001.

[28] M. Jones and J. Rawnick, "A new approach to broadband array design using tightly coupled elements," in *MILCOM 2007-IEEE Military Communications Conference*, IEEE, 2007, pp. 1–7.

[29] I. Tzanidis, K. Sertel, and J. L. Volakis, "Characteristic excitation taper for ultra-wideband tightly coupled antenna arrays," *IEEE transactions on antennas and propagation*, vol. 60, no. 4, pp. 1777–1784, 2012.

[30] ——, "Uwb low-profile tightly coupled dipole array with integrated balun and edge terminations," *IEEE Transactions on Antennas and Propagation*, vol. 61, no. 6, pp. 3017–3025, 2013.

[31] H. Huang, K. Xiao, L. Ding, S. Wang, and S. Chai, "Ultrawideband tightly coupled array for multiband communications at sx frequencies," in *2016 IEEE International Workshop on Electromagnetics: Applications and Student Innovation Competition (iWEM)*, IEEE, 2016, pp. 1–3.

[32] M. Huang, K. Zhang, L. Wang, and W. Qiao, "An ultrawideband tightly coupled antipodal vivaldi antenna array for uhf-ku band applications," in *2017 IEEE International Symposium on Antennas and Propagation & USNC/URSI National Radio Science Meeting*, IEEE, 2017, pp. 1323–1324.

[33] J. A. Kasemodel, "Low-profile ferrite loaded uwb tightly coupled dipole array," in *2011 IEEE International Symposium on Antennas and Propagation (APSURSI)*, IEEE, 2011, pp. 1973–1975.

[34] A. K. Awasthi and A. Harish, "Wideband low profile tightly coupled dipole antenna array with an integrated balun," in *2016 International Conference on Emerging Trends in Communication Technologies (ETCT)*, IEEE, 2016, pp. 1–3.

[35] H. Hao and S. Chai, "Ground-enhanced ultrawideband single-polarized tightly coupled dipole array," in *2015 IEEE Advanced Information Technology, Electronic and Automation Control Conference (IAEAC)*, IEEE, 2015, pp. 1034–1037.

[36] I. O. Farhat, K. Z. Adami, Y. Zhang, A. K. Brown, and C. V. Sammut, "Ultra-wideband tightly coupled phased array antenna for low-frequency radio telescope," 2013.

[37] R. N. Pack, A. S. Brannon, and D. S. Filipović, "Tightly coupled array of horizontal dipoles over a ground plane," *IEEE Transactions on Antennas and Propagation*, vol. 68, no. 3, pp. 2097–2107, 2019.

[38] S. Lu, C. Gu, G. Han, Z. Zhou, X. Li, and Z. Li, "A double dipoles per cell structure for solving common-mode resonance in tightly coupled dipole array," in *2016 IEEE International Conference on Microwave and Millimeter Wave Technology (ICMMT)*, IEEE, vol. 2, 2016, pp. 829–831.

[39] L. J. Chu, "Physical limitations of omni-directional antennas," *Journal of applied physics*, vol. 19, no. 12, pp. 1163–1175, 1948.

[40] R. Collin and S. Rothschild, "Evaluation of antenna q," *IEEE Transactions on Antennas and Propagation*, vol. 12, no. 1, pp. 23–27, 1964.

[41] S. R. Best, "A discussion on the quality factor of impedance matched electrically small wire antennas," *IEEE Transactions on Antennas and Propagation*, vol. 53, no. 1, pp. 502–508, 2005.

[42] F. W. Grover, *Inductance calculations: working formulas and tables*. Courier Corporation, 2004.

[43] C. R. Paul, *Analysis of multiconductor transmission lines*. John Wiley & Sons, 2007.

[44] R. Collin, *Dyadic green's functions in electro-magnetic theory: Chen-to tai. 246 pages, diagrams, 6x9 in. scranton, pa., international text book, 1971. price $14.50 (approx.£ 5· 35).* 1973.

[45] T. S. Rappaport *et al.*, *Wireless communications: principles and practice*. prentice hall PTR New Jersey, 1996, vol. 2.

[46] G. Arfken and H. Weber, *Mathematical methods for physicists, fifth-edition*, 2001.

[47] E. W. Weisstein, *Binomial theorem*. [Online]. Available: https://mathworld.wolfram.com/BinomialTheorem.html.

[48] ——, [Online]. Available: https://mathworld.wolfram.com/CylindricalCoordinates.html.

[49] R. W. King, *The theory of linear antennas*. Harvard University Press, 2013.

[50] Y. Haykır and A. Köksal, "A novel singularity-free analysis of coaxial-fed thick monopole antennas," *IEEE Transactions on Antennas and Propagation*, vol. 63, no. 12, pp. 5860–5863, 2015.

[51] J. A. Stratton, *Electromagnetic theory*. John Wiley & Sons, 2007, vol. 33.

[52] R. F. Harrington, *Time-harmonic electromagnetic fields*. McGraw-Hill, 1961.

[53] R. W. P. (W. P. King, *Electromagnetic engineering... by Ronold W. P. King...* eng, 1st ed.., ser. Radio communication series. New York, London: McGraw-Hill book company, inc., 1945.

[54] G. Fikioris and T. T. Wu, "On the application of numerical methods to hallen's equation," *IEEE Transactions on Antennas and Propagation*, vol. 49, no. 3, pp. 383–392, 2001.

[55] W.-X. Wang, "The exact kernel for cylindrical antenna," *IEEE Transactions on Antennas and Propagation*, vol. 39, no. 4, pp. 434–435, 1991.

[56] R. F. Harrington, *Field computation by moment methods*. Wiley-IEEE Press, 1993.

[57] D. Werner, P. Werner, and J. Huffman, "An exact method for integration of the cylindrical wire kernel," in *Proceedings of IEEE Antennas and Propagation Society International Symposium and URSI National Radio Science Meeting*, IEEE, vol. 2, 1994, pp. 1177–1180.

[58] D. H. Werner, "A method of moments approach for the efficient and accurate modeling of moderately thick cylindrical wire antennas," *IEEE Transactions on Antennas and Propagation*, vol. 46, no. 3, pp. 373–382, 1998.

[59] P. Rogers and M. Gunn, "An entire-domain galerkin analysis of the moderately thick dipole," *IEEE Transactions on Antennas and Propagation*, vol. 28, no. 1, pp. 117–121, 1980.

[60] J. A. Huffman, *Numerical modeling of current-carrying wire antennas using exact expressions for the vector potential and electric field integrals*. The Pennsylvania State University, 1995.

[61] J. Huffman and D. Werner, "Modeling of a cylindrical wire antenna with flat end caps using a rigorous moment method technique," *Radio Science*, vol. 36, no. 3, pp. 407–423, 2001.

[62] J. Lifländer and P. F. Oy, "Radiated efficiency: A true measure of antenna performance," *Finland: Pulse Electronics, Corp*, 2010.